

pubs.acs.org/JACS Article

A Candidalysin-Neutralizing Nanomodulator Enhances Colorectal Cancer Immunotherapy by Targeting Fungi-Macrophage Crosstalk

Yu Yan, Kai Zhao, Shan-Shan Pan, Yu-Liang Sun, Zhi-Yong Rao, and Xian-Zheng Zhang*



Cite This: https://doi.org/10.1021/jacs.5c13804



ACCESS

III Metrics & More

Article Recommendations

Supporting Information

ABSTRACT: In colorectal cancer (CRC), the upregulation of Candida albicans (C. albicans) abundance significantly promotes tumor progression and exacerbates immunosuppression. In this study, we demonstrate that candidalysin-induced macrophage pyroptosis contributes to the immunosuppressive tumor microenvironment (TME). Conversely, the neutralizing peptide of candidalysin, isolated via phage display, effectively protects macrophages from pyroptosis. Based on this, we constructed an epigenetic inhibitor-loaded nanomodulator to target the interaction between C. albicans and macrophages. To ensure precise targeting of intraspecific morphological differences, the nanomodulator is covered with the C. albicans pretreated macrophage membranes. The nanomodulator exhibits the ability to protect macrophages



from pyroptosis and reprograms the metabolic and immune response of macrophages, while the epigenetic inhibitor upregulates tumor self-antigen presentation. In vivo, the nanomodulator has been shown to effectively sustain macrophage activation within the TME and promotes a robust IL-17-mediated immune response. Meanwhile, the nanomodulator exhibited excellent immune memory effects and effectively synergized with immune checkpoint blockade therapy in an orthotopic CRC model. This approach of manipulating the *C. albicans*—macrophage crosstalk to augment therapeutic efficacy in CRC offers promising insights for the clinical management of CRC.

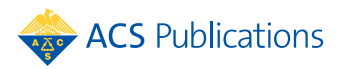
INTRODUCTION

Fungi represent a vital component of the human microbiome and fulfill crucial functions in host immune regulation. In diverse physiological environments, fungi modulate host immunity and invade immunocompromised individuals, including cancer patients.1-4 Increasing evidence suggests that the abundance of fungi is subtly elevated at the tumor sites. For instance, Candida abundance is upregulated in headneck tumors and gastrointestinal tumors, Blastomyces is elevated in lung cancer, Malassezia is enriched in breast cancer, and Lactobacillus is more abundant in head-neck cancer. The expansion of these fungi is frequently associated with increased tumor invasiveness and reduced patient survival, 6,7 indicating that tumor-associated fungi may serve as prognostic markers in a variety of tumors and offer more accurate predictions of immunotherapy efficacy compared to bacterial communities.8 The detailed molecular mechanisms by which fungi affect tumor progression remain poorly understood, and there is a paucity of potential pathways for prevention strategies and diagnosis.

Candida albicans (C. albicans), a native fungus in the human intestine, exists in two distinct forms: yeast and hyphae. The transition from yeast to hyphae, in conjunction with the secretion of candidalysin, is a pivotal characteristic contributing to the pathogenicity of C. albicans. 9-11 The substantial

enrichment of C. albicans in gastrointestinal tumors has been demonstrated to serve as an indicator of poor prognosis, correlating with diminished survival rates and a negative response to immunotherapy.8 Macrophages, the most abundant immune cells within tumors, 12 are important for immune defense against microbial invasion. There is a dynamic interaction between C. albicans and macrophages. 13 Macrophages recognize pathogen-associated molecular patterns (PAMPs) of C. albicans via pattern recognition receptors (PRRs), leading to phagosome formation.¹³ Within the phagosome, C. albicans is degraded through the coordinated action of lysosomal proteases, lipases, glycosidases, and nucleases. The subsequent degradation products have been found to modulate intracellular metabolic pathways and trigger downstream immune activation signals. Furthermore, as central mediators in both innate and adaptive immunity, macrophages activate differentiation of Th1 and Th17 cells,

Received: August 10, 2025 Revised: October 31, 2025 Accepted: October 31, 2025



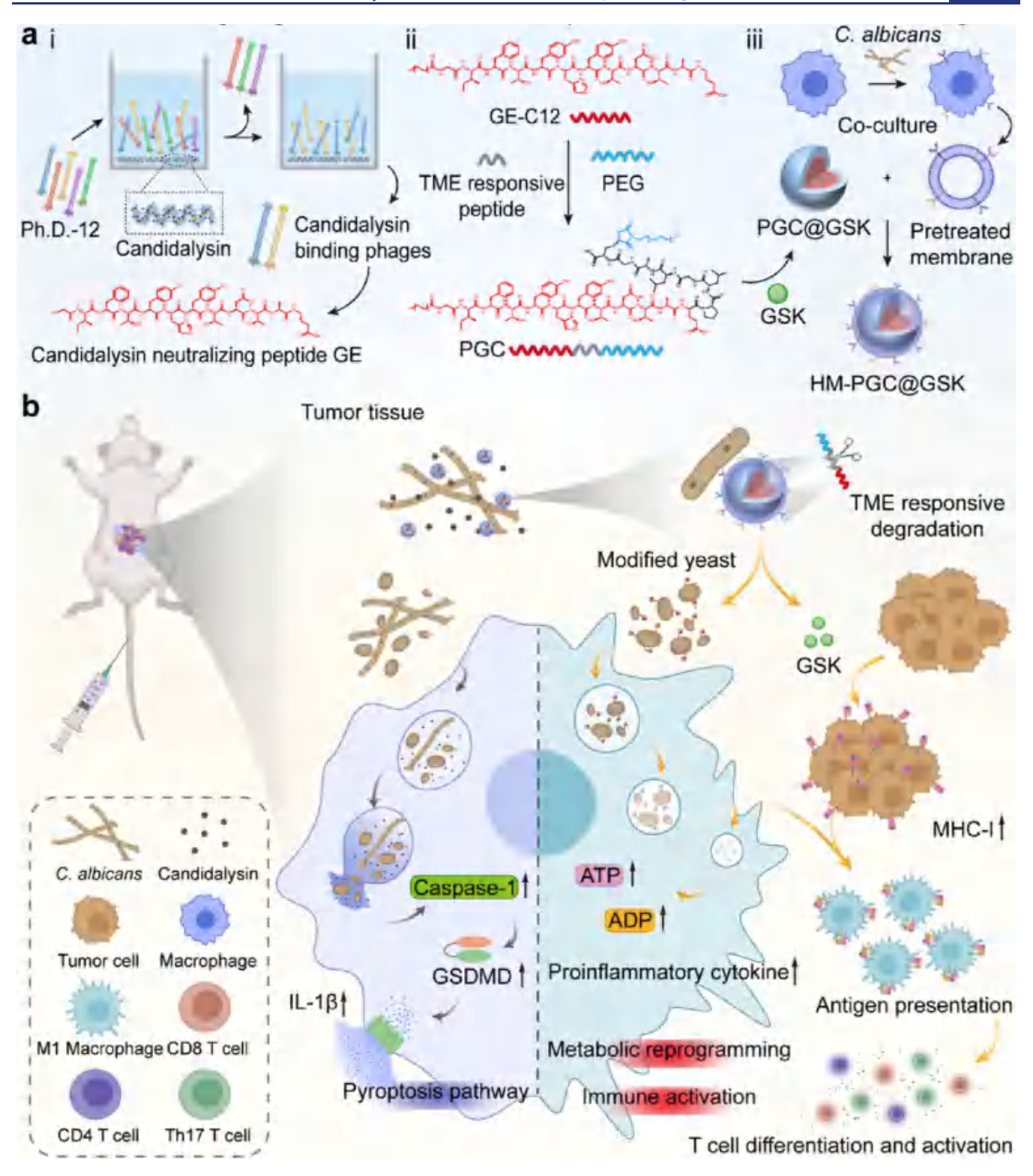


Figure 1. Schematic diagram of HM-PGC@GSK regulating the interplay between intratumoral *C. albicans* and macrophages to enhance colon cancer immunotherapy. (a) Schematic diagram of HM-PGC@GSK synthesis. The schematic was created with Adobe Illustrator and BioRender.com. (b) HM-PGC@GSK selectively targets *C. albicans* via HM surface recognition and responds to tumor-associated MMP-2 for releasing C12-GE and GSK-3484862. C12-GE neutralizes candidalysin and regulates the morphology of *C. albicans*, reprogramming macrophage fate and activating the TME. Concurrently, GSK upregulates the self-antigen presentation of tumor cells and promotes specific adaptive tumor immunity.

thereby limiting further *C. albicans* expansion. ¹⁶ It has been demonstrated that Th1 and Th17 cell-mediated signaling pathways played inhibitory roles in tumor progression. ¹⁷ However, within an immunosuppressive microenvironment,

macrophages are likely to fail to respond to the expansion of *C. albicans*. ^{18,19} *C. albicans* manipulates hyphae and candidalysin to inhibit macrophage activity, thereby blocking Th17 cell differentiation signals, inducing regulatory T cell (Treg)

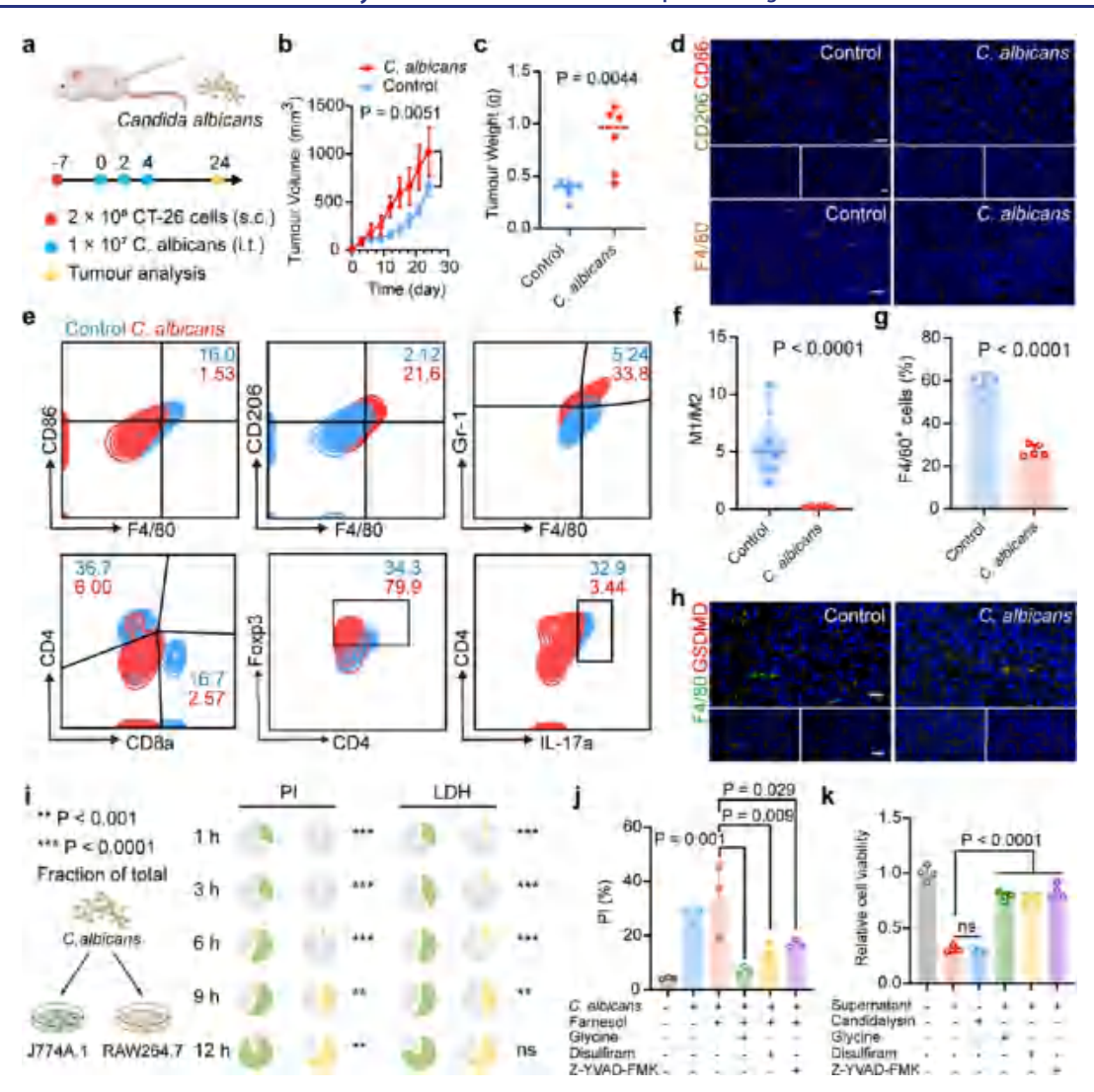


Figure 2. *C. albicans* promoted CRC progression and induced macrophage pyroptosis in the TME. (a) Schematic diagram of the CT26 subcutaneous CRC model with intratumoral *C. albicans* administration. (b) Tumor growth curves over 24 days in CRC mice treated with or without *C. albicans.* n = 6 independent mice. (c) Quantitative analysis of subcutaneous tumor weights of mice across treatment groups on day 24. n = 6 independent mice. (d) Representative immunofluorescence images showing CD86, CD206, and F4/80 expression in CRC tumor tissues under different treatments. Scale bar: 50 μ m. (e) Representative FCM plots of M1 macrophages (CD86+ in CD11b+ F4/80+ cells), M2 macrophages (CD206+ in CD11b+ F4/80+ cells), MDSCs (Gr-1+ F4/80+ in CD11b+ cells), CD8+ cytotoxic T cells (CD8+ in CD3+ cells), Tregs (CD4+ F0xp3+ in CD3+ cells), and Th17 cells (CD4+ IL-17a+ in CD3+ cells) in tumor tissues of CRC mice under different treatments. (f) M1/M2 macrophage ratio in tumor tissues from different CRC treatment groups. n = 5 independent samples. (g) Quantification of total macrophage infiltration (F4/80+ cells) in tumor tissues among treatment groups. n = 5 independent samples. (h) Representative immunofluorescence images showing coexpression of F4/80 and GSDMD in CRC tumor tissues. Scale bar: 50 μ m. (i) Schematic of *C. albicans* coculture with J774A.1 and RAW264.7. Pie charts of PI staining and lactate dehydrogenase (LDH) quantitative analysis at different time points of coculture. The green pie charts represent J774A.1 cells, and the yellow pie charts represent RAW264.7 cells. (j) Quantitative analysis of J774A.1 cell viability following exposure to *C. albicans* conditioned supernatant or candidalysin. n = 4 independent samples. Data are presented as the mean \pm s.d. Statistical significance was determined by unpaired two-tailed Student's t-test (b,t,t,t,t) and one-way ANOVA with Tukey's post hoc correction (j,t).

differentiation, and exacerbating further immunosuppression. Consequently, the outcome of the interaction between *C. albicans* and macrophages after phagocytosis plays a pivotal role in shaping the local and systemic immune environment.

In recent years, nanomedicine has made significant progress in modulating tumor-associated bacterial microbiota. Nevertheless, the fungal management presents a series of challenges due to their complex behavior and significant variability in natural conditions. At present, fungal management still relies on broad-spectrum antifungal agents, such as

polyenes and azoles. However, these agents lack specificity and indiscriminately eradicate diverse fungal populations, thereby disrupting the stability of the human microbiome. Horeover, resistance to broad-spectrum antifungals continues to rise each year. To prevent the emergence of drug resistance, fungal management requires higher spatial and temporal precision. Consequently, the development of a nanomodulator is essential to meeting the stringent demands of effective fungal management.

In this study, the interaction between *C. albicans* and macrophages within the tumor microenvironment (TME) was

investigated as well as the therapeutic potential of nanomedicine-based intervention following this interaction. Our findings demonstrated that a high abundance of C. albicans accelerated the progression of colorectal cancer (CRC) and induced macrophage pyroptosis. Further analysis revealed that this pyroptosis was not contingent on the morphological state of C. albicans but was closely associated with its secreted candidalysin. To address this issue, phage display technology was employed to identify a neutralizing peptide, GE, that specifically bound to candidalysin. The conjugation (C12-GE) of GE with a long carbon chain has been shown to neutralize candidalysin and promote C. albicans yeast morphology, thereby enabling macrophages to evade pyroptosis. Furthermore, C12-GE compromised the viability of C. albicans, facilitating its utilization by macrophages as a metabolic substrate. This process has been shown to reprogram macrophage metabolic pathways and promote their activation. Leveraging the multifunctional capabilities of nanotechnology, we synthesized amphiphilic micelles (PGC) based on C12-GE and encapsulated the DNA methylation inhibitor GSK-3484862 (GSK). This design had been demonstrated to enhance the expression of major histocompatibility complex class I molecules (MHC I) on tumor cells, facilitate antigen presentation, and strengthen adaptive antitumor immunity. This approach, which strengthens antitumor immunity by promoting tumor cell self-antigen presentation, shares similarities with nanoparticle-based strategies that enhance antitumor immunity through the induction of immunogenic cell death (ICD).²⁶

Furthermore, a matrix metalloproteinase-2 (MMP-2) responsive peptide was incorporated with the objective of enabling tumor-specific release of the nanomodulator and preserving intestinal microbial homeostasis. To achieve targeted delivery to C. albicans hyphae, the nanomodulator was coated with hyphae-pretreated macrophage membranes (HM). These membranes exhibited specific PPR profiles that were conducive to hyphal recognition (Figure 1a). Moreover, the macrophage membrane expressed SIRP α naturally, facilitating tumor-directed chemotaxis. In summary, this work developed an epigenetic nanomodulator that precisely edited tumor-associated fungi to modulate macrophage metabolism and immune function, laying the foundation for managing fungal dysbiosis in the TME and enhancing CRC therapy (Figure 1b).

RESULTS AND DISCUSSION

C. albicans Contributes to the Progression of Colorectal Cancer by Inducing Macrophage Pyroptosis within the TME. To investigate the role of C. albicans in CRC progression, a subcutaneous tumor model of CT26 cells in BALB/c mice was established. Mice were administered with C. albicans or saline intratumorally on days 0, 2, and 4 (Figure 2a). The results demonstrated that the tumors in mice treated with C. albicans exhibited accelerated growth, with tumor volume increasing by 54.06% relative to that of the control group. On day 24, the tumor mass in the C. albicans-treated group was 1.3-fold heavier than that in the control group (Figure 2b,c), indicating that C. albicans administration promoted colorectal tumor progression. To further characterize the tumors after administration of C. albicans, pathological analysis was performed on day 24. Hematoxylin and eosin (H&E) staining revealed a heavier tumor burden in the C. albicans-treated group compared to the controls (Figure S1a).

Ki67 and transferase-mediated dUTP-biotin nick end labeling (TUNEL) staining showed an increased cellular proliferation and reduced apoptosis in the C. albicans-treated group. The AIbased quantitative analysis results showed that the TUNEL intensity in the tumors of mice treated with C. albicans was 55.2% lower than that in the control group, while the Ki67 intensity was 1.65-fold higher than that in the control group (Figure S1b,c). Additionally, immunofluorescence analysis revealed a marked reduction in total macrophages (F4/80⁺) within tumors of mice treated with C. albicans, with the majority exhibiting an immunosuppressive phenotype (CD206⁺) (Figures 2d and S2). To further assess the immune cell phenotype within the TME, flow cytometric analysis was conducted. Compared to controls, the tumors of mice treated with C. albicans contained fewer pro-inflammatory M1 macrophages, higher levels of immunosuppressive M2 macrophages and myeloid-derived suppressor cells (MDSCs) (Figures 2e,f and S3a-c), with total macrophage content reduced by 53.39% (Figure 2g). In addition, there was a notable decrease in the infiltration of CD8+ T cells, CD4+ T cells, and Th17 cells (Figures 2e and S3d,e), alongside an increase in Tregs (Figures 2e and S3f). Collectively, these findings indicated that C. albicans contributed to the highly immunosuppressive TME establishment, which might hinder effective tumor therapy. Notably, in tumor tissues of mice treated with C. albicans, macrophage marker F4/80 colocalized more significantly with pyroptosis markers gasdermin D (GSDMD) and GSDMD-N (Figures 2h, S4, and S5). These pieces of evidence suggested that the observed reduction in macrophages following C. albicans treatment was likely driven by pyroptosis.

To further explore the impact of *C. albicans* on macrophages, we employed two widely used murine macrophage cell lines, J774A.1 and RAW264.7.²⁹ These cells were coincubated with C. albicans at a multiplicity of infection (MOI) of 2 for various durations. Cell viability was assessed via Calcein-AM/ propidium iodide (PI) dual staining and was quantified using flow cytometry. Following prolonged coculture (>9 h), both macrophage lines exhibited pronounced cell death (Figure S6a,b), which was also confirmed by the detection of lactate dehydrogenase (LDH) content in the supernatant and the results of cell flow cytometry (Figures 2i and S6c-e). This outcome was consistent with prior observations that hyphal overgrowth by C. albicans could mechanically disrupt macrophage membranes during extended coculture. 18,19 Unexpectedly, J774A.1 cells exhibited significantly greater cell death than RAW264.7 cells during the initial 9 h of exposure, as indicated by higher LDH release in the supernatant and PI positivity (Figures 2i and S6a-e). One key distinction between these cell lines is that RAW264.7 cells lack the apoptosisassociated speck-like protein containing a caspase recruitment domain (ASC) (Figure S7a), which is essential for NLRP3 inflammasome assembly.²⁹ As a result, RAW264.7 cells exhibit an increased resistance to NLRP3-mediated pyroptotic cell death. In the bright field, it was found that J774A.1 coincubated with C. albicans for 1 h showed obvious cell swelling (Figure S7b), which was a typical morphology of cell pyroptosis. Western blot analyses revealed that J774A.1 cells treated with C. albicans exhibited time-dependent increases of caspase-1 and GSDMD-N (Figure S7c), while IL-1 β levels, a downstream indicator of pyroptosis, also progressively increased (Figure S7d). To validate the involvement of the pyroptotic pathway, the caspase-1 inhibitor Z-YVAD-FMK,

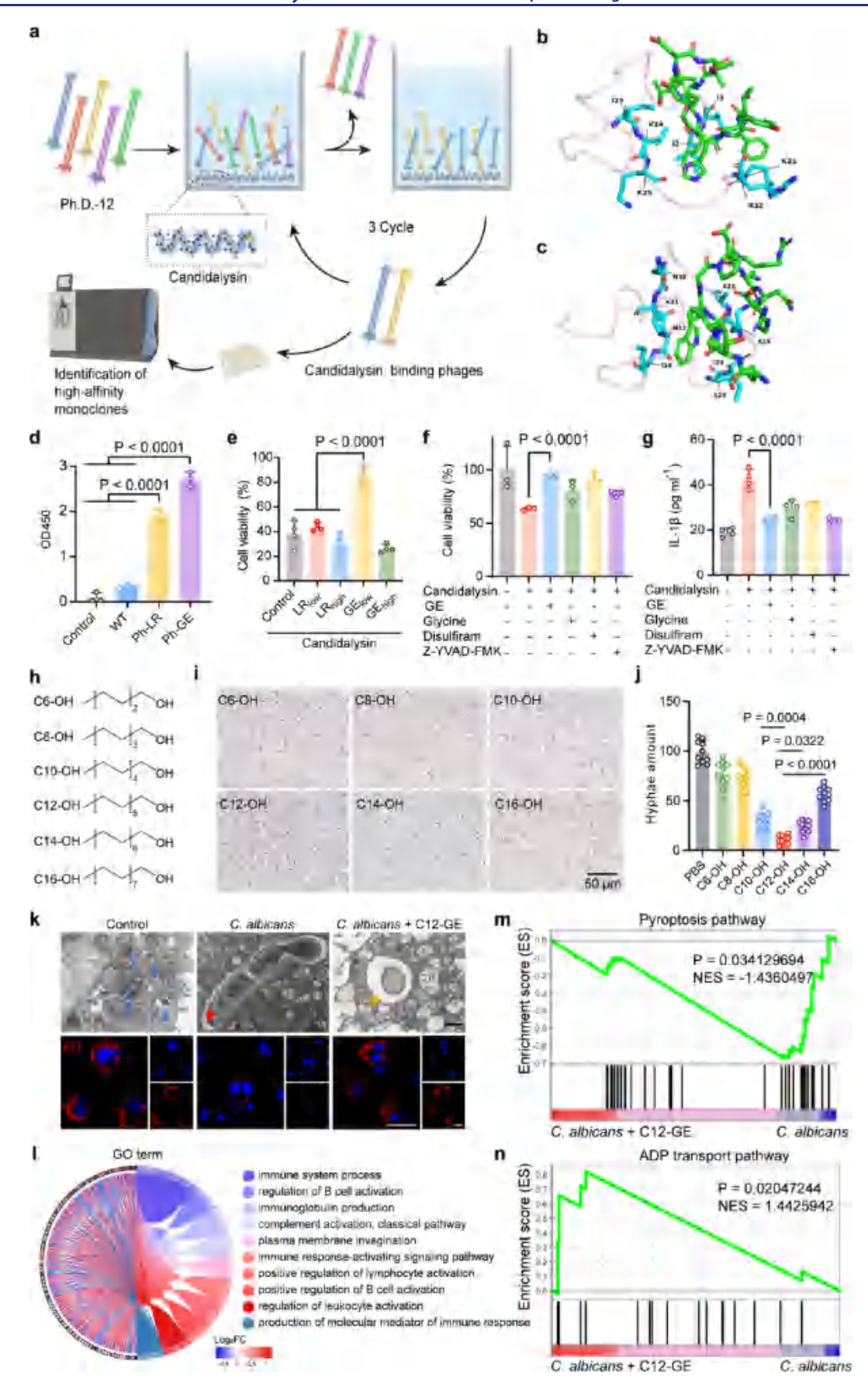


Figure 3. Inhibition of candidalysin effectively inhibited the pyroptosis of macrophages. (a) Schematic diagram of phage displayed screening of candidalysin-binding peptides. The schematic was created with Adobe Illustrator and BioRender.com. (b) The model of peptide GE (blue-green) binding to candidalysin (light purple) protein. (c) The model of peptide LR (blue-green) binding to candidalysin (light purple) protein. (d) ELISA

Figure 3. continued

quantification of the interaction between candidalysin and two high-frequency phage clones (Ph-LR and Ph-GE), a control phage (WT), and a control. n=3 independent samples. (e) Quantitative analysis of peptide LR and peptide GE in eliminating candidalysin toxicity in BMDMs. n=4 independent samples. (f) Quantitative analysis of peptide GE in inhibiting candidalysin-induced BMDM pyroptosis. n=3 independent samples. (g) Quantitative analysis of IL-1 β secretion by BMDMs following GE peptide-mediated inhibition of candidalysin-induced pyroptosis. n=4 independent samples. (h) Chemical structures of fatty alcohols with various carbon chain lengths. (i) Representative bright-field images of *C. albicans* yeast morphology induced by fatty alcohols of differing chain lengths. (j) Quantitative analysis of *C. albicans* yeast morphology induced by fatty alcohols of differing chain lengths. n=10 independent samples. (k) Representative biological scanning electron microscopy images of lysosomes inside BMDMs after different treatments. Scale bar: 50 μ m (inset, 20 μ m). (l) Chord diagrams showing Gene ontology (GO) enrichment analysis of differentially expressed genes in BMDMs treated with *C. albicans* alone versus *C. albicans* + C12 GE. (m) Gene set enrichment analysis (GSEA) comparing pyroptosis pathways among differentially expressed genes post-treatment with *C. albicans* versus *C. albicans* + C12 GE. Data are presented as the mean \pm s.d. Statistical significance was determined by one-way ANOVA with Tukey's post hoc correction (d,e,f,g,j).

glycine inhibiting the membrane aggregation of NINJ1 protein, ³⁰ and the NLRP3 antagonist 1 were incorporated into the coculture system. Each inhibitor significantly reduced the PI-positive cell rate and attenuated macrophage death (Figure S7e). Overall, these results strongly suggested that *C. albicans* induced macrophage death predominantly via activation of the NLRP3-mediated pyroptosis pathway.

To determine whether the ability of C. albicans to induce macrophage pyroptosis is linked to its natural virulence hyphae morphology, we induced its yeast morphology using farnesol.³¹ And we incorporated the commonly used disulfiram, an inhibitor of the pore-forming activity of GSDMD protein by covalently modifying the cysteine residue at position 191, into the experimental system.³² Unexpectedly, even the yeast morphology induced macrophage death to a comparable extent, and all three inhibitors of pyroptosis effectively mitigated this cytotoxicity (Figures 2j and S7f). These results suggested that, in early interactions, the C. albicans morphological state exerted only a minor influence on its pyroptosis-inducing capacity. Given that many microorganisms affect hosts via secreted metabolites, 33,34 we hypothesized that a secretion of C. albicans might mediate the observed pyroptotic response. We focused on candidalysin, a key virulence factor produced by C. albicans, which played a crucial role in the progress of inflammatory bowel disease.¹¹ Both purified candidalysin and C. albicans culture supernatant induced macrophage death, which could be largely abrogated by glycine, disulfiram, and Z-YVAD-FMK (Figure 2k). Comprehensively, these results demonstrated that candidalysin secreted by C. albicans played a key role in the induction of macrophage pyroptosis in early interactions (Figure S8).

Phage-Displayed Candidalysin-Neutralizing Peptide Enhances Macrophages' Resistance to Pyroptosis and Reprograms Their Metabolic Profile, Shifting to an **Antitumor Phenotype.** Currently, there is a lack of available and precise strategies for candidalysin management. To address this, we employed phage display technology to screen peptides that specifically bind to candidalysin in the 12-peptide library (Figure 3a). After three biopanning rounds, two promising peptide sequences were identified: GE (GIFTY-HYTDTAE) and LR (LSVPWGPRDNNR) (Figure S9a,b). Molecular docking simulations conducted with AutoDock Vina revealed that GE formed 8 hydrogen bonds with candidalysin, exhibiting a predicted binding free energy of -1.91 kcal mol (Figure 3b), whereas LR formed nine hydrogen bonds with a predicted binding free energy of -1.43 kcal mol⁻¹ (Figure 3c). The ELISA results demonstrated that Ph-GE exhibited a stronger binding affinity to candidalysin compared with Ph-LR

(Figure 3d). These findings indicated that GE exhibited a higher binding affinity toward candidalysin. MTT assays further demonstrated that GE effectively neutralized the cytotoxicity of candidalysin at a low concentration in bone marrow-derived macrophages (BMDMs), whereas the higher concentrations of cytotoxicity indicated free GE was not suitable for systemic administration (Figure 3e). Additionally, GE significantly inhibited candidalysin-induced macrophage death and IL-1 β secretion to levels comparable to those of the control (Figure 3f,g). These results collectively indicated that GE bound to candidalysin and prevented induction of macrophage pyroptosis. In addition, C. albicans naturally exhibits two forms, hyphae and yeast, which trigger different immune effects.³⁵ The dimorphism of *C. albicans* could be regulated by the long fatty alcohols, which could insert into the phospholipid bilayer of C. albicans, interfering with the normal physiological activities and switching morphology from hyphae to yeast.³¹ However, fatty alcohols with excessively short chain lengths exhibit limited efficacy, whereas those with overly long chains are prone to precipitation due to the increased hydrophobicity. To identify the optimal chain length for inhibiting hyphal formation, we cocultured C. albicans with fatty alcohols of varying chain lengths (C6, C8, C10, C12, C14, and C16) for 12 h (Figure 3h,i). Among these, C12 demonstrated the greatest inhibitory effect, reducing hypha formation by approximately 89.4% (Figure 3j). This suggested that the C12 chain was sufficiently long to insert into C. albicans and effectively inhibited hyphal development while also possessing optimal water solubility to preserve a high free concentration.

We synthesized C12-GE by conjugating the candidalysin-neutralizing peptide GE with a C12 fatty alcohol chain. The molecular docking analysis between C12-GE and candidalysin was performed, demonstrating a binding energy of -1.585 kcal mol⁻¹ (Figure S10a). Furthermore, we further examined the ability of C12-GE to neutralize candidalysin toxicity (Figure S10b) and protect BMDMs from pyroptosis (Figure S10c). These results suggested that the conjugation of C12 to GE did not affect the ability of GE to neutralize candidalysin.

C12-GE continuously induces yeast morphology and neutralizes candidalysin, thereby preventing *C. albicans* from inducing macrophage pyroptosis. Given that microbial viability after endocytosis affects macrophages' nutrient metabolism and downstream signaling pathways, ¹⁴ we evaluated the effect of C12-GE-treated *C. albicans* on the macrophage physiology after endocytosis. First, transmission electron microscopy revealed that the untreated *C. albicans* still retained a filamentous structure after being endocytosed by BMDMs,

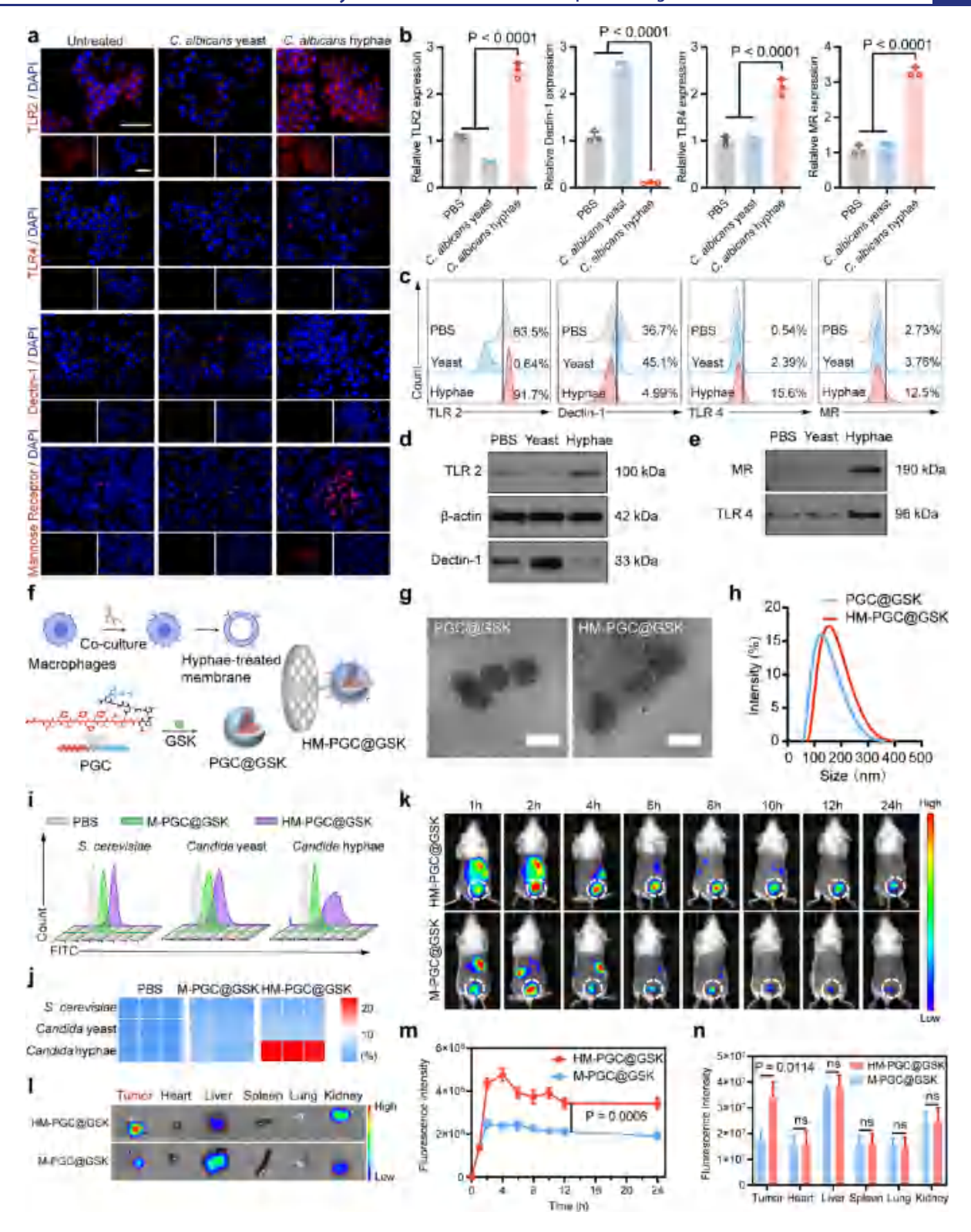


Figure 4. Macrophage membrane prestimulated by *C. albicans* hyphae (HM) assisted the synthesis of HM-PGC@GSK nanomodulators for precise targeting of *C. albicans* both in vitro and in vivo. (a) Representative CLSM images showing differential expression of (TLRs) on the surface of macrophages exposed to *C. albicans* hyphae and yeast form. Scale bar: $50 \mu m$. (b) Relative mRNA expression of TLRs in macrophages exposed to *C. albicans* hyphae and yeast form. n = 3 independent samples. (c) Representative FCM images of the surface expression of different TLRs on the surface of macrophages treated with hyphae and yeast. (d,e) Western blot analyses confirming differential TLR protein expression in macrophages stimulated by hyphae versus yeast forms. (f) Schematic diagram of the synthesis of HM-PGC@GSK. (g) Transmission electron microscopy images and corresponding hydrated particle size distributions of PGC@GSK and HM-PGC@GSK nanoparticles. Scale bar: 100 nm. (h) Hydrated particle size of PGC@GSK and HM-PGC@GSK. (i,j) Flow cytometry evaluation of in vitro targeting efficiency, showing representative histograms (i) and quantitative binding analysis (j) of M-PGC@GSK and HM-PGC@GSK to *C. albicans* hyphae and yeast, n = 3 independent samples. (k) Representative in vivo imaging system (IVIS) images of BALB/c mice bearing subcutaneous CRC tumors injected intratumorally with *C. albicans*

Figure 4. continued

within 24 h after intravenous administration of DIR-labeled M-PGC@GSK or HM-PGC@GSK. (1) Representative IVIS images of tumors and various organs of BALB/c mice bearing subcutaneous CRC tumors injected intratumorally with C. albicans within 24 h after intravenous administration of DIR-labeled M-PGC@GSK or HM-PGC@GSK. (m) Quantification of in situ tumor fluorescence over 24 h after intravenous administration of DIR-labeled M-PGC@GSK or HM-PGC@GSK in BALB/c mice bearing subcutaneous CRC tumors injected intratumorally with C. albicans. n = 3 independent samples. (n) Quantitative analysis of fluorescence intensity of tumors and various organs 24 h after intravenous administration of DIR-labeled M-PGC@GSK or HM-PGC@GSK in subcutaneous CRC BALB/c mice injected intratumorally with C. albicans. n = 3 independent samples. Data are presented as the mean ± s.d. Statistical significance was determined by one-way ANOVA with Tukey's post hoc correction (b) and unpaired two-tailed Student's t-test (m,n).

which disrupted the stability of lysosomes (indicated by red arrows). In contrast, C. albicans treated with C12-GE showed yeast morphology (yellow arrows) inside BMDMs lysosomes, which had clear boundaries and normal morphology like those in the control group (blue arrows) (Figure 3k). Intracellular fungal structures appeared blurred and underwent degradation. At the same time, acridine orange (AO) staining was used to detect the integrity of BMDM lysosomes after different treatments. The results showed that lysosomes in C. albicanstreated BMDMs exhibited diminished red fluorescence, indicating decreased lysosome acidity and compromised integrity. Conversely, lysosomes in the C. albicans treated with the C12-GE group retained strong red fluorescence, proving a preserved acidic environment and structural integrity (Figures 3k and S11a,b). These observations demonstrated that C12-GE could effectively protect macrophage lysosomes from C. albicans-induced damage, providing macrophages with a competitive advantage against C. albicans invasion and enabling normal degradation processes.

In order to explore the effect of C12-GE on the macrophage after regulating C. albicans in more detail, we conducted a comprehensive transcriptional analysis of BMDMs after different treatments. The Venn diagram revealed substantial transcriptomic alterations in both treatment groups (Figure S12a). Compared with the control group, 94 genes were upregulated and 224 genes were downregulated in BMDMs treated with C. albicans (P < 0.05, fold change ≥ 2) (Figure S12b), and 51 genes were upregulated and 14 genes were downregulated in BMDMs treated with C. albicans and C12-GE (P < 0.05, fold change ≥ 2) (Figure S12c). Additionally, relative to the C. albicans-treated group, 300 genes were upregulated and 47 genes were downregulated in BMDMs treated with C. albicans and C12-GE (P < 0.05, fold change \geq 2) (Figure S12d). These results indicated that C12-GE partially restored the gene expression profile of BMDMs altered by C. albicans. Kyoto Encyclopedia of Genes and Genomes (KEGG) enrichment analysis revealed that the differentially expressed genes between the C. albicans + C12-GE treatment group and the C. albicans treatment group were predominantly involved in signal transduction, the immune system, and signaling molecules and interactions (Figure S12e). GO term analysis further identified the enrichment in multiple immune activation pathways and plasma membrane invagination, suggesting that C12-GE might enhance the macrophage phagocytic capacity (Figure 31). Notably, differentially expressed gene clustering analysis demonstrated that additional treatment with C12-GE upregulated genes related to macrophage activation (Tnfsf8, GITRL, Flt3), T cell activation, and Th17 cell differentiation and chemotaxis (Il12, Slamf6, Ccr6). Meanwhile, genes involved in lipid metabolism (Gpr183 and F2r), carbohydrate metabolism (Glcci1), cyclic AMP production (Atp1b1), amino acid

metabolism (Adcy6, Slc43a1), and antioxidant metabolism (Gpx8, Dusp13a) were also significantly upregulated (Figure S13). In addition, gene set enrichment analysis (GSEA) indicated that C12-GE negatively regulated the pyroptosis pathway in BMDMs (Figure 3m) while modulating multiple nutrient metabolism pathways, including gluconeogenesis and ADP transport processes (Figures 3n and S14a-c). These pieces of evidence prove that C12-GE prevented C. albicansinduced pyroptosis, promoted energy metabolism, and activated multiple antitumor immune pathways. Moreover, it was shown that cotreatment with C12-GE and C. albicans effectively enhanced the ability of BMDMs to phagocytose Cy5.5-labeled tumor cells compared with both the *C. albicans*treated and control groups (Figure S15a-c). This finding functionally demonstrated that C12-GE treatment could steer macrophages toward an antitumor phenotype. In summary, C12-GE served as a bridge between pathogenic fungi and immune cells, steering macrophages toward an antitumor phenotype through metabolic and functional reprogramming.

Engineering of HM-PGC@GSK for Targeted Recognition of C. albicans Hyphae via Pretreated Macro**phage Membranes.** To achieve precise regulation of C. albicans in a complex environment, we used the differential expression of macrophage membrane receptors induced by distinct stimuli to achieve specific targeting. Cell membranederived nanoparticles have demonstrated enhanced biological functions in various physiological environments.^{36–39} The expression profiles of Toll-like receptors (TLRs) on macrophages exhibit spatial variation in response to stimulation by different microorganisms.⁴⁰ Specifically, prior research studies have focused on genus-level differences; 40 it remains unclear whether different morphological states of the same microbe elicit distinct receptor expression patterns. Therefore, we compared the expression of Toll-like receptors on macrophages stimulated by C. albicans hyphae and yeast forms, respectively. The immunofluorescence confocal laser scanning microscopy (CLSM) images revealed that stimulation with fungal cells enhanced the fluorescence intensity of TLR2, TLR4, and the mannose receptor (MR), whereas stimulation with yeast cells increased the expression of Dectin-1 (Figure 4a). These findings were corroborated by qPCR; the mRNA levels of TLR2, TLR4, and MR in macrophages were upregulated after hyphae stimulation, while the level of Dectin-1 in macrophages was upregulated after yeast stimulation (Figure 4b). Flow cytometry and Western blot analyses further confirmed that distinct forms of C. albicans elicited different receptor expression profiles in macrophages (Figures 4c-e and S16a-d). The differential expression provides a molecular basis for using stimulated macrophage membranes as a biomimetic delivery platform, enabling targeted recognition of specific fungal states in vivo.

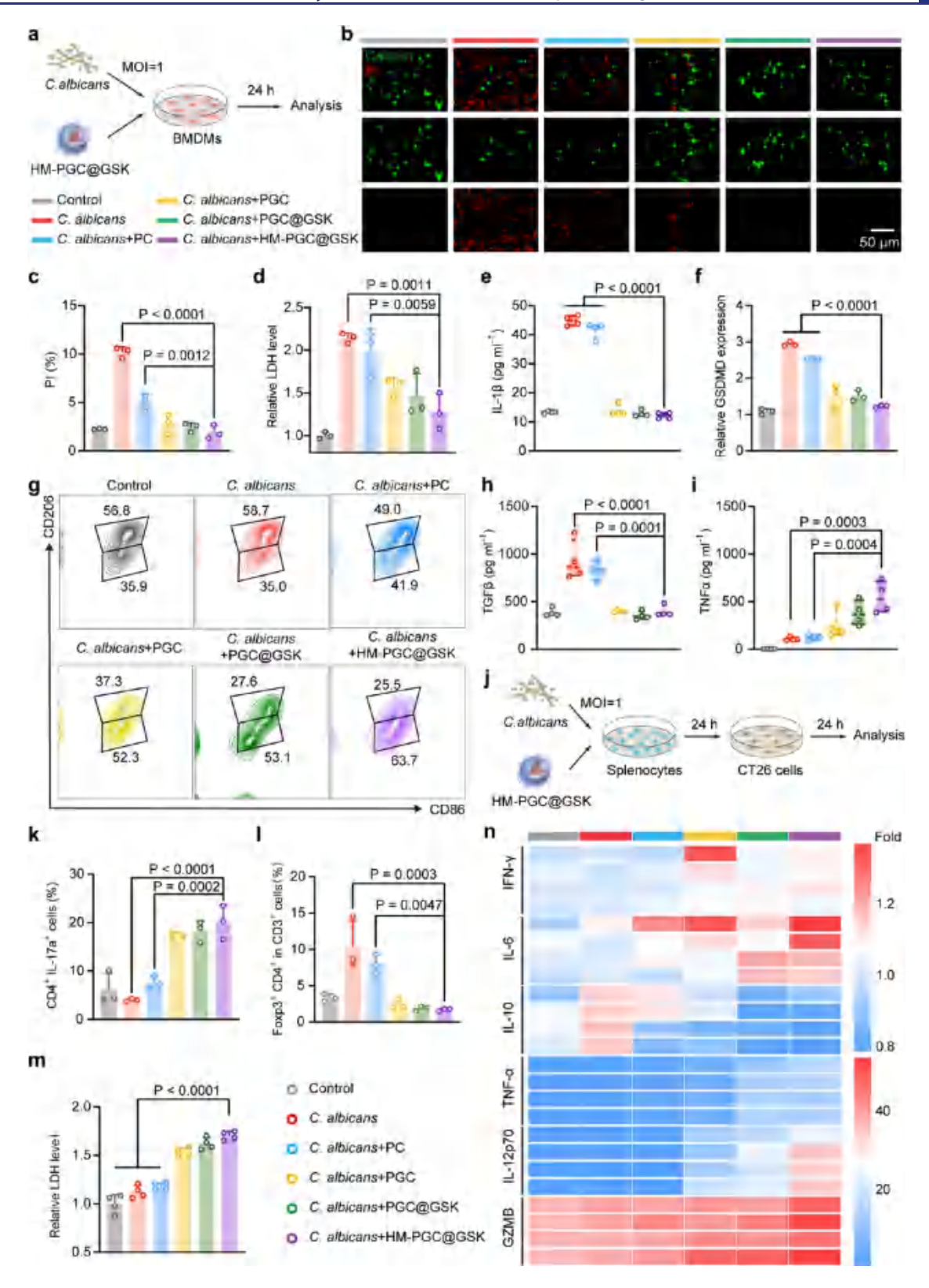


Figure 5. HM-PGC@GSK modulated the *C. albicans*—macrophage axis by inhibiting macrophage pyroptosis and activating both macrophage and Th17-associated immune responses. (a) Schematic diagram of the experiment of HM-PGC@GSK inhibiting *C. albicans*-induced macrophage pyroptosis. (b) Representative CLSM images of Calcein-AM/PI staining of BMDMs following various treatments. (c) Quantitative analysis of PI-positive BMDMs via FCM. n=3 independent samples. (d) Quantitative analysis of LDH release by BMDMs after different treatments. n=3 independent samples. (e) Quantitative analysis of IL-1 β secretion by BMDMs after different treatments by ELISA. n=4 independent samples. (f) qRT-PCR analysis of GSDMD mRNA expression in BMDMs under each treatment condition. n=3 independent samples. (g) Representative FCM plots of M1 and M2 BMDM phenotypes after different treatments. (h,i) Quantitative analysis of TGF β (h) and TNF α (i) secretion by BMDMs after different treatments. n=4 independent samples. (j) Schematic diagram of the experimental workflow for assessing HM-PGC@GSK-mediated activation of splenocytes and CT26 tumor cell lysis. (k,l) FCM analysis of Th17 cells (k) and Tregs (l) differentiation in whole splenocyte

Figure 5. continued

cultures after different treatments. n = 3 independent samples. (m) Cytotoxicity assay quantifying splenocyte-mediated CT26 cell death. n = 4 independent samples. (n) Quantitative analysis of the secretion of IFN- γ , IL-6, IL-10, TNF- α , IL-12p70, and GZMB by splenocytes after different treatments by ELISA. n = 4 independent samples. Data are presented as the mean \pm s.d. Statistical significance was determined by one-way ANOVA with Tukey's post hoc correction (c,d,e,f,h,i,k,l,m).

Next, we prepared C12-GE-based micelles coated with hyphae-stimulated macrophage membranes (HM), forming a nanomodulator HM-PGC@GSK that specifically regulated the tumor microorganism-macrophage axis (Figure 4f). For tumor-specific responsiveness, the amphiphilic polymer PGC incorporated MMP-2 cleavable peptides linking poly(ethylene glycol) (PEG) to C12-GE (Figure S17a-c), self-assembling into stable micelles with a critical micelle concentration of 0.071 g L⁻¹ (Figure S17d). In order to induce specific immunity and achieve long-term immune memory, the epigenetic inhibitor GSK-3484862 was encapsulated inside. GSK-3484862 is a selective noncovalent DNA methyltransferase 1 inhibitor, known to induce significant demethylation with low nonspecific cytotoxicity. 41 We compared several widely used DNA methylation inhibitors with relatively low nonspecific cytotoxicity (RG108, GSK-3484862, and SGI-1027) and evaluated their ability to upregulate MHC class I expression in CT26 tumor cells. The result demonstrated that GSK-3484862 exhibited the strongest MHC class I upregulation (Figure S18). The morphology, stable zeta potential, and hydrated particle size (~200 nm hydrated diameter) of HM-PGC@GSK were confirmed by TEM and Zetasizer (Figures 4g,h and \$19a). The surface zeta potential of PGC and PGC@GSK is mainly attributed to the hydrophilic PEG and GE segments. PEG itself is uncharged and therefore makes a neutral contribution to the zeta potential. In contrast, the GE sequence (GIFTYHYTDTAE) contains two strongly acidic amino acid residues (D and E) and only one basic residue (H), which is only partially protonated under physiological pH (approximately 7.4). As a result, the overall polypeptide segment carries the net negative charge, leading to the negative surface zeta potential observed for both PGC and PGC@GSK. The slight increase in hydrated particle size, accompanied by a decrease in zeta potential, indicated the successful coating of HM over PGC@GSK. High-performance liquid chromatography analysis demonstrated MMP-2 triggered GSK-3484862 release, with a 1.4-fold increase in release rate compared to the untreated nanoparticles (Figure S19b), indicating targeted degradation within the TME and minimal off-target effects. Furthermore, the sizes of HM-PGC@GSK and PGC@GSK in a serum-containing culture medium had negligible changes within 7 days (Figure S20). The results suggested the satisfactory stability of HM-PGC@GSK and PGC@GSK.

To assess the targeting efficacy of HM-PGC@GSK toward *C. albicans* hyphae within complex biological environments, we initially evaluated the targeting ability of the nanomodulators to different fungi in vitro. The nanoparticles M-PGC@GSK synthesized with macrophage membranes without pretreatment were used as a control experimental group. The CLSM images demonstrated that the HM coating facilitated specific binding of HM-PGC@GSK to *C. albicans* hyphae in vitro. Notably, HM-PGC@GSK exhibited minimal nonspecific binding to *Saccharomyces cerevisiae*, which was abundantly present in the intestinal microbiota (Figure S21). Flow cytometry further confirmed the target specificity of HM-

PGC@GSK, showing that hyphae treated with HM-PGC@ GSK exhibited a 5.3-fold increase in green fluorescence intensity compared to those treated with M-PGC@GSK (Figure 4i,j). To examine the target specificity in vivo, HM-PGC@GSK and M-PGC@GSK were intravenously administered to subcutaneous CRC mice, and the distribution of nanoparticles at different time points was monitored by an in vivo imaging system (IVIS). Notably, in mice given intratumoral administration of C. albicans, HM facilitated the rapid accumulation and prolonged retention of nanoparticles at the tumor site (Figure 4k,m). Ex vivo imaging of major organs at 24 h postinjection revealed that HM-PGC@GSK maintained strong fluorescence within the tumor, with the signal intensity being about 1.98 times greater than that of the M-PGC@GSK group (Figures 4l,n and S22). In vivo, fluorescence photons must traverse multiple layers of biological tissue before reaching the detector, resulting in substantial signal attenuation. This attenuation explains why the bioluminescence intensity observed in Figure 4m is lower than that in Figure 4n. Furthermore, histological analysis confirmed the colocalization of HM-PGC@GSK with C. albicans in tumor tissues (Figure S23). However, in mice without *C. albicans* treatment, there was no significant difference in the enrichment of HM-PGC@ GSK and M-PGC@GSK in tumors, whether in vivo or in vitro (Figure S24a-d). These results suggested that intratumoral administration of C. albicans could effectively enhance the targeting and retention of HM-PGC@GSK, further demonstrating the effectiveness of the pretreated membrane.

These above results revealed that HM-PGC@GSK had excellent tumor retention and specific recognition of *C. albicans* hyphae, both in vivo and in vitro, highlighting its potential as a precise therapeutic nanomedicine for modulating the tumor—microbiota—immune axis.

HM-PGC@GSK Modulates the Interaction between *C. albicans* and Macrophages, Enabling Macrophages to Evade Pyroptosis While Sustaining Immune Activation. We first examined the ability of HM-PGC@GSK to induce the morphological transformation of *C. albicans* in the presence or absence of MMP-2. Representative bright field images demonstrated that, in the presence of MMP-2, PGC, PGC@GSK, and HM-PGC@GSK effectively inhibited the formation of hyphae and maintained the yeast morphology. In contrast, the absence of MMP-2 markedly diminished this inhibitory effect (Figure S25a,b). These results indicated that the components of C12-GE facilitated the morphological transition to the yeast form and exhibited a responsiveness to MMP-2.

To further investigate the capacity of HM-PGC@GSK to regulate the interaction between C. albicans and macrophages, we examined the effect of HM-PGC@GSK on the coculture system of C. albicans and BMDMs for 24 h (Figure 5a). Calcein/PI double staining representative CLSM images after coculture revealed a significant reduction in PI-positive cells in the PGC, PGC@GSK, and HM-PGC@GSK groups, compared with the PC group (Figure 5b,c). Additionally, the release of LDH and IL-1 β in the HM-PGC@GSK groups was

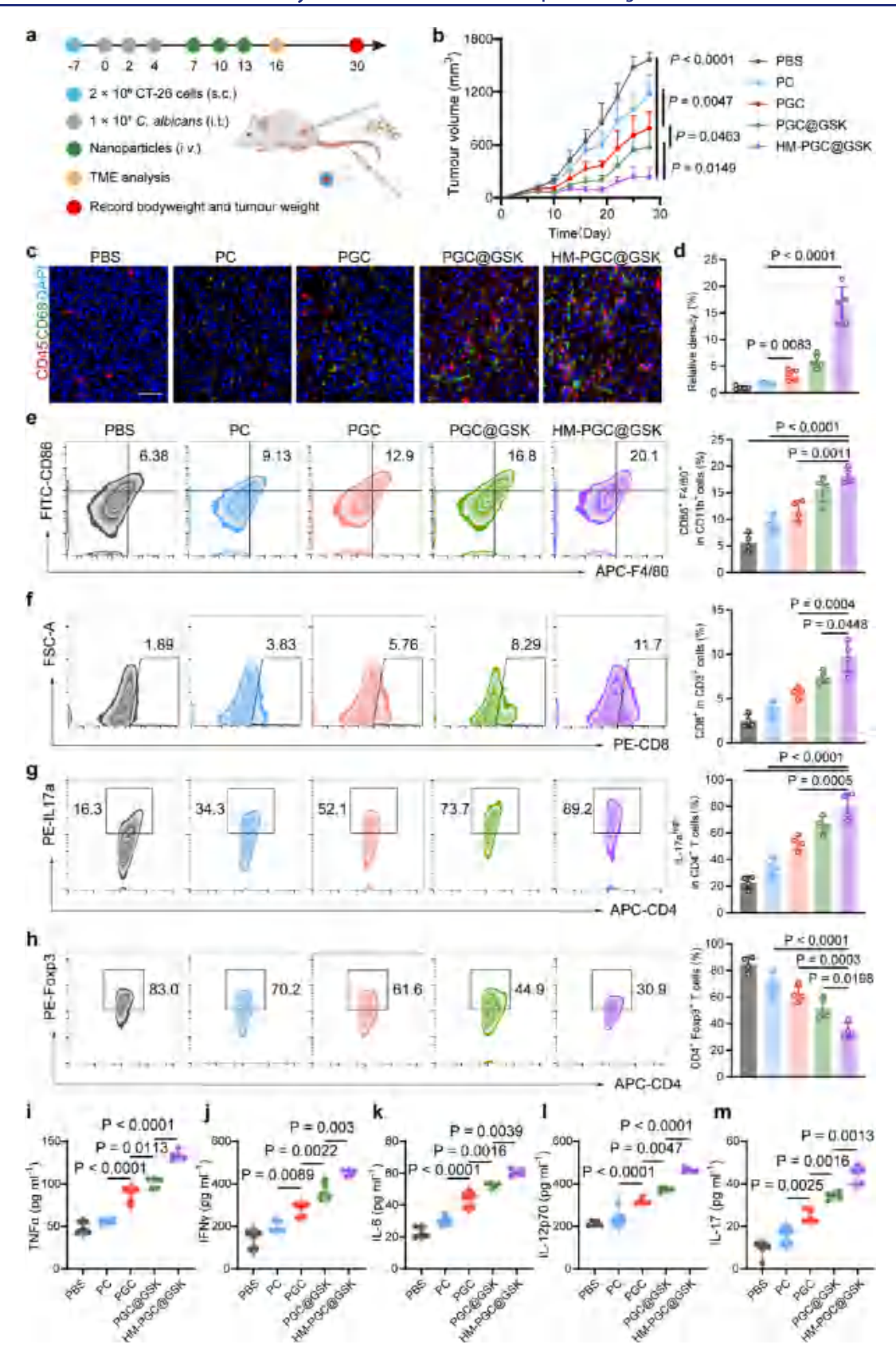


Figure 6. HM-PGC@GSK showed excellent antitumor efficacy and promoted the immune microenvironment activation in the CT26 subcutaneous tumor model. (a) Schematic diagram of the CT26 subcutaneous tumor model construction and the HM-PGC@GSK treatment scheme. (b) Tumor volume curves within 28 days in mice treated with PBS, PC, PGC, PGC@GSK, and HM-PGC@GSK. n = 6 independent mice. (c,d) Representative immunofluorescence staining CLSM images of CD68 and CD45 expression in tumor tissues from different treatment groups (c) and quantitative fluorescence intensity analysis of CD68 (d). Scale bar: $50 \ \mu m$. n = 5 independent samples. (e,h) Representative FCM images and quantitative statistical analysis of M1 macrophages (CD86⁺ F4/80⁺ in CD11b⁺ cells) (e), CD8⁺ cytotoxic T cells (CD8⁺ in CD3⁺) (f), Th17 cells

Figure 6. continued

(IL-17a⁺ CD4⁺ in CD3⁺) (g), and Tregs (Foxp3⁺ CD4⁺ in CD3⁺) (h) in different treatment groups. n = 4 independent samples. (i-m) Quantitative statistical analysis of TNF- α (i), IFN- γ (j), IL-6 (k), IL-12p70 (l), and IL-17 (m) in tumor tissues of CT26 cell subcutaneous tumor mice in different treatment groups. n = 5 independent samples. Data are presented as the mean \pm s.d. Statistical significance was determined by one-way ANOVA with Tukey's post hoc correction.

significantly reduced (Figure 5d,e). Consistent with these results, qPCR analysis showed a marked downregulation of GSDMD expression in the HM-PGC@GSK group, approaching expression levels observed in the untreated group (Figure 5f). Similar phenomena were observed in parallel experiments conducted using J774A.1 macrophage cells (Figure S26a-d). The above evidence collectively proved that HM-PGC@GSK significantly and sustainably reverses the pyroptosis of macrophages caused by *C. albicans*.

Subsequently, we explored the immune status of macrophages that had evaded pyroptosis with the help of HM-PGC@GSK. BMDMs were cocultured with C. albicans and various nanoparticles, followed by assessment of macrophage immune phenotypes. Flow cytometry revealed that exposure to C. albicans increased CD206 expression while concurrently reducing CD86 expression on BMDMs, indicating a phenotypic shift toward an immunosuppressive M2-like state. Notably, HM-PGC@GSK effectively reversed these changes, resulting in decreased CD206 expression and elevated CD86 expression (Figure S27a,b). The M1/M2 ratio was significantly elevated, showing a 3.6-fold increase compared with the group treated with C. albicans alone (Figures 5g and S27c). Further cytokine analysis demonstrated that C. albicans exposure enhanced TGF- β secretion while reducing TNF- α production by BMDMs. In contrast, treatment with HM-PGC@GSK significantly suppressed TGF- β secretion and promoted TNF- α expression (Figure 5h,i). These results showed that HM-PGC@GSK reversed the immunosuppression caused by C. albicans and promoted macrophage polarization toward a proinflammatory M1-like phenotype. To assess the downstream effects of HM-PGC@GSK on other immune cells, splenocytes were pretreated with C. albicans and the various nanoparticles for 12 h and then cocultured with CT26 tumor cells (Figure 5j). Flow cytometric analysis revealed that HM-PGC@GSK significantly modulated the T cell subsets. Specifically, the proportion of Th17 cells was markedly increased after HM-PGC@GSK treatment, exhibiting a 4.99fold increase compared to treatment with C. albicans alone (Figure 5k), while the proportion of Tregs was significantly reduced to 0.16-fold that of the C. albicans-treated group (Figure 51). Analysis of CT26 tumor cells post coculture demonstrated a substantial increase in MHC class I molecule expression in the HM-PGC@GSK group (Figure S27d), suggesting enhanced antigen exposure. LDH release assays further indicated that HM-PGC@GSK treatment enhanced Tcell-mediated cytotoxicity against CT26 cells, representing a 57.83% improvement compared to the C. albicans-treated group (Figure 5m). It was shown that PGC@GSK and HM-PGC@GSK could significantly enhance the specificity of whole spleen cells in killing tumor cells (Figure S28a,b). This was theoretically because GSK-3484862 could effectively reduce the methylation level of tumor cell DNA, thereby contributing to the development of immune memory.

Moreover, ELISA analysis of coculture supernatants demonstrated elevated levels of various pro-inflammatory and immune-stimulatory cytokines in the HM-PGC@GSK group,

while the level of the immunosuppressive cytokine IL-10 was significantly reduced (Figure 5n). These findings demonstrated that HM-PGC@GSK effectively drove the differentiation of Th17 cells, enhanced the killing ability of T cells against tumor cells, and robustly modulated an immunostimulatory environment.

HM-PGC@GSK Exhibited Excellent Antitumor Efficacy and Robust Activation of the Immune Microenvironment in Subcutaneous Tumor Models. Encouraged by the activation of splenic immune cells and enhanced T cell cytotoxicity induced by HM-PGC@GSK in vitro, we next evaluated its therapeutic efficacy in vivo. A subcutaneous CRC mouse model was established, followed by the administration of various treatment regimens (Figure 6a). On day 28, the results showed that the tumor inhibition rate of the PGC@ GSK treatment group reached 63.37%, significantly higher than that of the PGC group (49.69%) and the PC group (25.00%). Notably, the HM-PGC@GSK group exhibited the highest inhibition rate, 85.04%, demonstrating a robust capacity to suppress subcutaneous tumor growth (Figures 6b and S29a). Histological examination and TUNEL staining further confirmed that HM-PGC@GSK treatment effectively inhibited tumor cell proliferation and significantly promoted apoptosis (Figure S29b).

To explore whether HM-PGC@GSK has exerted immunomodulatory effects within the TME in vivo, we performed immunofluorescence staining and flow cytometry analyses on CRC tumor tissues after virous treatment. Immunofluorescence results showed that HM-PGC@GSK enhanced macrophage accumulation to 16.28-fold higher than that observed in the control group (Figure 6c,d), proving that HM-PGC@GSK effectively maintains macrophage presence within tumors in vivo. Moreover, we examined the differentiation of intratumoral T cells in each group in the CT26 subcutaneous tumor model by immunofluorescence experiments (Figures S30 and S31). The results showed that the CD8⁺ T cells, CD4⁺ T cells, and Th17 cells in the HM-PGC@ GSK group were significantly increased compared with the control group, except for Tregs, proving that HM-PGC@GSK could promote the increase of cytotoxic T cells and helper T cells in the tumor and weaken the immunosuppression of TME. FCM results demonstrated a 2.22-fold increase in M1like macrophage populations after HM-PGC@GSK treatment (Figure 6e), accompanied by significant reductions in M2 macrophages and myeloid-derived suppressor cells (MDSCs) (Figure S32a,b). Additionally, HM-PGC@GSK significantly elevated CD8⁺ T cell infiltration in tumor tissues to 3.93 times that of the control group (Figure 6f). Among CD4⁺ T helper cells, Th17 cell levels increased 3.51 times more than those in the control, while Treg proportions decreased to 41.39% of the control group (Figure 6g,h). Furthermore, the proportion of mature dendritic cells in the inguinal lymph nodes reached 20% in the HM-PGC@GSK-treated group (Figure S32c), reflecting enhanced activation of adaptive antitumor immunity. Concurrently, levels of pro-inflammatory cytokines (TNF- α , IFN-γ, IL-6, IL-12p70, and IL-17) within tumor tissues were

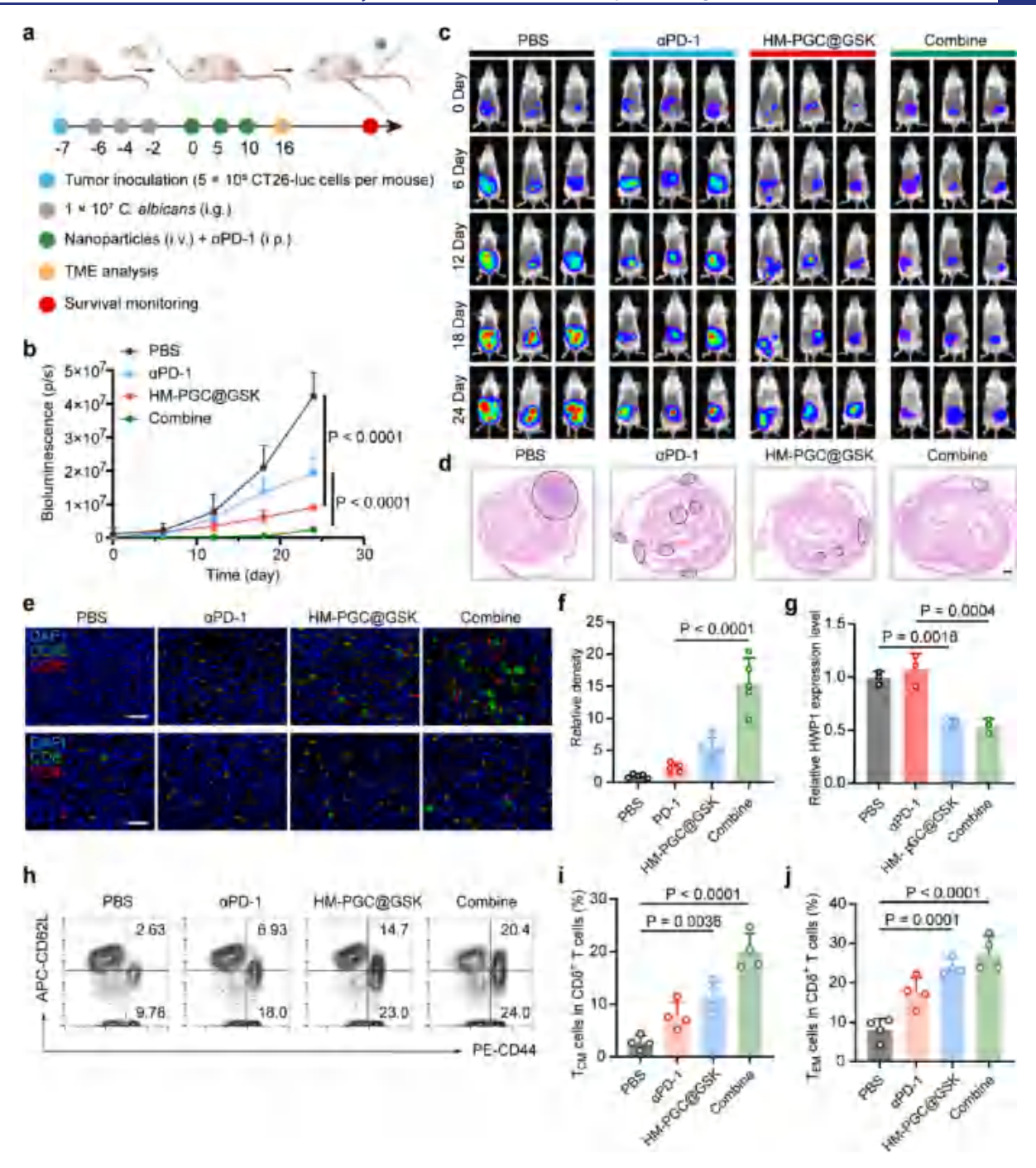


Figure 7. Antitumor efficacy of HM-PGC@GSK in combination with ICB therapy in an orthotopic *C. albicans*-burdened CRC model. (a) Schematic diagram of the construction of the orthotopic *C. albicans*-burdened colorectal cancer and the HM-PGC@GSK combined with the ICB treatment scheme. "i.g." refers to oral gavage. "i.v." refers to intravenous injections. "i.p." refers to intraperitoneal injections. (b,c) In vivo bioluminescence imaging of orthotopic CRC mice after receiving PBS, α PD-1, HM-PGC@GSK, and combined treatment. (d) Representative images of H&E staining of tumor-bearing intestinal segments of orthotopic CRC mice after different treatments. Scale bar: 0.5 mm. (e,f) Representative immunofluorescence staining CLSM images of CD68, CD45, CD4, and CD8 in tumor tissues of orthotopic CRC mice in different treatment groups (e) and quantitative analysis of relative fluorescence intensity of CD68 (f). Scale bar: 50 μ m. n = 5 independent samples. (g) qRT-PCR quantitative analysis of HWP1 mRNA levels in fecal flora of orthotopic CRC mice in different treatment groups. n = 3 independent samples. (h) Representative FCM images (h) and quantitative statistical analysis (i,j) of T_{CM} (CD44⁺ CD62L⁺ in CD8⁺) and T_{EM} (CD44⁺ CD62L⁻ in CD8⁺) in the spleen of mice with orthotopic colon cancer after different treatments. n = 4 independent samples. Data are presented as the mean \pm s.d. Statistical significance was determined by one-way ANOVA with Tukey's post hoc correction (b,f,g,i,j).

upregulated to varying extents following HM-PGC@GSK treatment (Figure 6i-m). Collectively, these results indicated that HM-PGC@GSK effectively alleviated *C. albicans*-induced immunosuppression within the TME, promoted the accumulation of pro-inflammatory macrophages, and amplified

downstream T cell responses, ultimately supporting more robust and durable antitumor immunity.

Moreover, we examined the expression of MHC I in CT26 subcutaneous tumors of mice after receiving different treatment regimens (Figure S33). The results showed that HM-

PGC@GSK and PGC@GSK had a significant upregulation of MHC I compared to the control group, upregulating 9.36-fold and 5.13-fold, respectively. Furthermore, we performed a subcutaneous tumor experiment, including several additional control groups. The results demonstrated that HM-PGC@ GSK achieved significantly greater antitumor efficacy compared with free GSK-3484862, HM-PGC, M-PGC@GSK, and Liposome@DOX (Figure S34a,b). Specifically, the tumor inhibition rates were approximately 42.9% in the free GSK-3484862 group, 58.7% in the HM-PGC group, and 86.2% in the HM-PGC@GSK group, which notably exceeded the expected effect under the additivity model of 76.4% for GSK and HM-PGC treatment. These findings indicated that GSK and HM-PGC acted synergistically rather than merely contributing additive therapeutic effects, thereby further supporting the rationale for the design of HM-PGC@GSK. Otherwise, the results showed that mice treated with HM alone did not exhibit superior therapeutic efficacy compared with the control group. And the immunofluorescence staining images showed that the TME in mice treated with the HM coating exhibited no significant recruitment or differentiation of T cells and macrophages (Figure S35). These results cleared the primary role of the HM coating being the precise targeting of intratumoral fungi.

Next, we assessed the hemolytic test of HM-PGC@GSK. The results showed that neither nanoparticle exhibited strong direct cytotoxicity, indicating that its therapeutic efficacy is not primarily mediated by direct tumor cell killing. The hemolytic rates stay below 5% after being cocultured with HM-PGC@ GSK under various concentrations, suggesting that HM-PGC@GSK has negligible effects on blood cells and possesses satisfactory blood compatibility (Figure S36). And we assessed the cytotoxicity of HM-PGC@GSK and PGC@GSK in both tumor and normal cells (Figure S37a,b). The results showed that neither nanoparticle exhibited strong direct cytotoxicity, indicating that their therapeutic efficacy is not primarily mediated by direct tumor cell killing. While HM-PGC@GSK showed excellent antitumor effects, it did not induce a significant decrease in the weight of tumor-bearing mice (Figure S38a), suggesting minimal systemic toxicity. Hematological and biochemical analyses revealed no notable abnormalities across treatment groups (Figure S38b-f), and histopathological examination of major organs via H&E staining showed no evident tissue damage or pathological alterations (Figure S39). These findings prove that HM-PGC@GSK possessed favorable biocompatibility and safety profiles, underscoring its potential for clinical translation.

HM-PGC@GSK Combined with Immune Checkpoint Blockade for the Treatment of Orthotopic Colorectal Cancer. In the subcutaneous tumor model, HM-PGC@GSK effectively reshaped the TME. To further assess its potential to enhance immune checkpoint blockade (ICB) therapy in CRC, we established an orthotopic CRC mouse model and administered various treatment regimens (Figure 7a). The results indicated that HM-PGC@GSK effectively sensitized α PD-1 therapy. Specifically, the tumor inhibition rate of the combined treatment group reached 94.35%, markedly higher than 54.28% of the α PD-1 group and 78.67% of the HM-PGC@GSK group (Figures 7b,c and S40). Survival analysis showed that the combined therapy prolonged the median survival of mice from 28 to 49 days, representing a 75% improvement (Figure S41a). H&E staining of the intestinal tissues confirmed a substantial reduction in tumor burden

following the combination therapy (Figure 7d). Furthermore, TUNEL staining and Ki67 immunofluorescence showed that the combined therapy promoted tumor cell apoptosis and suppressed cellular proliferation more effectively than either monotherapy (Figure S41b).

Immunofluorescence analysis revealed that the combinatorial treatment group exhibited a more significant enrichment of CD8+ T cells and macrophages within the TME compared to the monotherapy group. Notably, the macrophage intensity was upregulated by 15.43-fold, proving the ability of HM PGC@GSK to preserve macrophage activity in situ (Figure 7e,f). Moreover, HM-PGC@GSK significantly reduced the mRNA expression of the C. albicans hypha-associated gene HWP1 in mouse fecal samples (Figure 7g). These pieces of evidence proved that HM-PGC@GSK modulated C. albicans dimorphism in a complex environment and regulated interactions between C. albicans and macrophages. Furthermore, the immune memory response triggered by HM-PGC@ GSK was examined on day 16 after virous treatment. The combined treatment of HM-PGC@GSK and αPD-1 significantly increased the central memory T cells (T_{CM}) and effector memory T cells (T_{EM}) in the spleen of the orthotopic CRC mice, which increased by 6.46-fold and 2.37-fold, respectively, compared with the control group (Figure 7h-j). Immunofluorescence analysis revealed that the combined treatment group exhibited a 1.62-fold increase in the number of Th17 cells compared with the α PD-1 group, accompanied by a 2.68fold reduction in Tregs (Figure S42). These findings highlighted the capacity of HM-PGC@GSK to augment the efficacy of ICB therapy and strengthen immunological memory in colorectal cancer.

To further clarify the mechanism of HM-PGC@GSK, we examined the impact of *C. albicans* infection on the therapeutic efficacy of HM-PGC@GSK by establishing an orthotopic colon cancer model without C. albicans infection (Figure S43). The results showed that in the absence of *C. albicans*, the α PD-1 group achieved a tumor inhibition rate of 67.6%, whereas the HM-PGC@GSK group exhibited only a 30.1% inhibition rate. This outcome contrasted with the findings in the orthotopic colon cancer model with the oral administration of C. albicans, where HM-PGC@GSK demonstrated superior antitumor efficacy (Figure 7b,c). These results indicated that HM-PGC@GSK exerted its therapeutic benefits primarily in the context of C. albicans overgrowth, further supporting the conclusion that its efficacy was mediated through the modulation of *C. albicans* within the tumor microenvironment.

CONCLUSIONS

Our study demonstrated that a high abundance of C. albicans promoted the progression of CRC, with macrophage pyroptosis induced by candidalysin likely serving as a critical contributing factor in this process. Based on this finding, we integrated the candidalysin-neutralizing peptide with an epigenetic regulator and developed the nanomodulator HM-PGC@GSK.

It is noteworthy that HM-PGC@GSK enabled highly specific intraspecific morphological targeting and precise modulation of the physiological activity of intratumoral C. albicans hyphae. It had been demonstrated that HM-PGC@ GSK protected macrophages from pyroptosis and reprogrammed macrophages' energy metabolism and immune state in multiple models. Furthermore, HM-PGC@GSK markedly

improved the response to ICD and strengthened long-term memory immunity in an orthotopic CRC model.

In addition, it is important to note that distinct macrophage subtypes may exhibit differential sensitivities to candidalysin, attributable to variations in their metabolic programs and the basal activation state of inflammasomes. This warrants further investigation in future studies.

Collectively, this study elucidated a previously underexplored mechanism by which tumor-associated fungi might contribute to tumor progression and introduced a multifunctional nanotherapeutic strategy for targeted fungal intervention. The nanomedicine-mediated regulation of fungi-macrophage interactions introduced effective therapeutic avenues for the clinical management of tumor-associated fungal dysbiosis and its integration into cancer immunotherapy.

ASSOCIATED CONTENT

Data Availability Statement

The data that support the findings of this study are available from the corresponding author upon reasonable request.

Supporting Information

The Supporting Information is available free of charge at https://pubs.acs.org/doi/10.1021/jacs.5c13804.

Materials and methods; experimental details, including preparation and characterization of HM-PGC@GSK, BMDM pyroptosis assay and activation assay in vitro, splenocyte activation and killing assay, phage display assay, biological transmission electron microscopy assay, antitumor therapeutic efficacy investigation in the CT26 subcutaneous tumor model, therapeutic efficacy and long-term antineoplastic immune memory investigation in the orthotopic CT26-luc CRC model, and immune profiling; histological analysis; quantitative analysis; quantitative statistical analysis; distribution of red and green fluorescence intensities; immunofluorescence images and quantitative colocalization analysis; CLSM and FCM images, flow cytometry analysis, and quantitative analysis; details of pyroptosis induced by C. albicans in macrophages; schematic diagram of the distinct pathways of macrophage cell death; quantitative analysis and bright-field images of phage outputs; details of neutralization of candidalysin by C12-GE preventing macrophage pyroptosis; AO staining in BMDMs after different treatments; Venn diagram, volcano plots, and KEGG pathway annotation analysis; heat map for identification of differentially expressed genes; GSEA enrichment analysis; BMDM phagocytosis of tumor cells after different treatments; synthesis and characterization of PGC; FCM quantitative analysis; synthesis and characterization of HM-PGC@GSK; stability plot; CLSM images; fluorescence images; targeting capacity of HM-PGC@GSK and M-PGC@GSK; morphological transformation of C. albicans induced by HM-PGC@ GSK; schematic diagram of splenocyte killing specificity detection and cell viability details; average growth curves of CRC tumors and H&E staining, TUNEL staining, and Ki67 staining images; tumor volume curves and H&E staining images of tumor tissues; hemolysis rates of mouse blood; cell viability and live/dead staining images; average body weight of mice with subcutaneous CRC tumors, heat map of the complete blood cell count analysis, and analysis of complete blood biochemical

indices; H&E staining images of major organs; bright-field images of the intestinal sections; survival curves and Ki67 and TUNEL staining images of tumor sites; schematic diagram of the orthotopic CRC model and in vivo bioluminescence imaging and quantitative analysis; gating strategies used for flow cytometry analysis; probe sequences for FISH experiments; and primer sequences for qRT-PCR analysis (PDF)

AUTHOR INFORMATION

Corresponding Author

Xian-Zheng Zhang — Key Laboratory of Biomedical Polymers of Ministry of Education & Department of Chemistry, Wuhan University, Wuhan 430072, P. R. China; orcid.org/0000-0001-6242-6005; Email: xz-zhang@whu.edu.cn

Authors

Yu Yan — Key Laboratory of Biomedical Polymers of Ministry of Education & Department of Chemistry, Wuhan University, Wuhan 430072, P. R. China; orcid.org/0009-0007-0057-9904

Kai Zhao – Key Laboratory of Biomedical Polymers of Ministry of Education & Department of Chemistry, Wuhan University, Wuhan 430072, P. R. China; orcid.org/0000-0003-1176-1537

Shan-Shan Pan – Key Laboratory of Biomedical Polymers of Ministry of Education & Department of Chemistry, Wuhan University, Wuhan 430072, P. R. China

Yu-Liang Sun – Key Laboratory of Biomedical Polymers of Ministry of Education & Department of Chemistry, Wuhan University, Wuhan 430072, P. R. China

Zhi-Yong Rao – Key Laboratory of Biomedical Polymers of Ministry of Education & Department of Chemistry, Wuhan University, Wuhan 430072, P. R. China

Complete contact information is available at: https://pubs.acs.org/10.1021/jacs.5c13804

Author Contributions

[†]Y.Y. and K.Z. contributed equally.

Notes

The authors declare no competing financial interest.

ACKNOWLEDGMENTS

This work was supported by the National Natural Science Foundation of China (22135005, 52588201, and 52333004). The animal experiments were approved by the Institutional Animal Care and Use Committee of the Animal Experiment Center/A3 Laboratory of Wuhan University, and all animal experiments were conducted in accordance with the Guidelines for Animal Experimentation of the Animal Experiment Center/A3 Laboratory of Wuhan University.

REFERENCES

(1) Ost, K. S.; O'Meara, T. R.; Stephens, W. Z.; Chiaro, T.; Zhou, H.; Penman, J.; Bell, R.; Catanzaro, J. R.; Song, D.; Singh, S.; Call, D. H.; Hwang-Wong, E.; Hanson, K. E.; Valentine, J. F.; Christensen, K. A.; O'Connell, R. M.; Cormack, B.; Ibrahim, A. S.; Palm, N. W.; Noble, S. M.; Round, J. L. Adaptive Immunity Induces Mutualism Between Commensal Eukaryotes. *Nature* **2021**, *596*, 114–118.

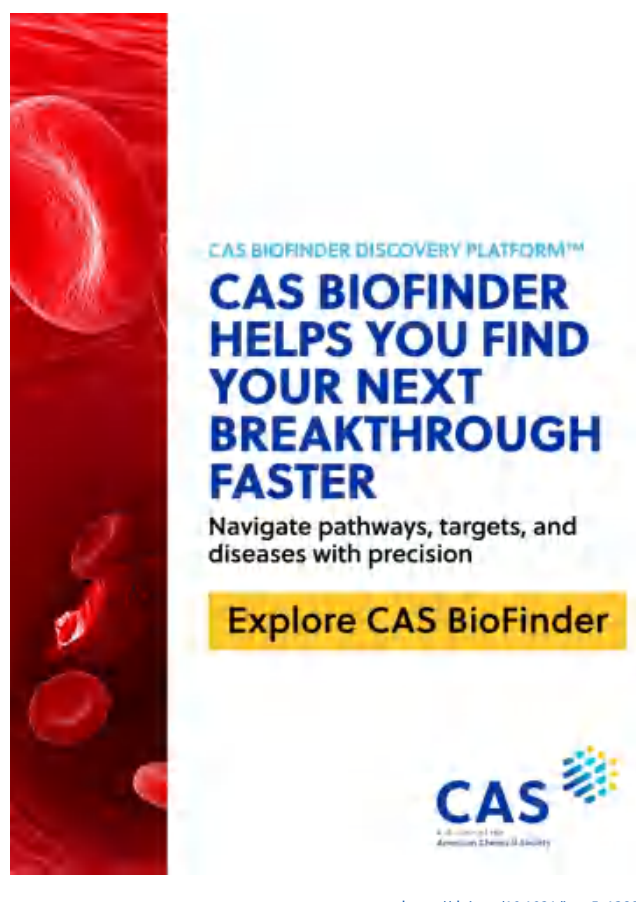
(2) Iliev, I. D.; Brown, G. D.; Bacher, P.; Gaffen, S. L.; Heitman, J.; Klein, B. S.; Lionakis, M. S. Focus on Fungi. *Cell* **2024**, *187*, 5121–5127.

- (3) Ost, K. S.; Round, J. L. Commensal Fungi in Intestinal Health and Disease. *Nat. Rev. Gastroenterol. Hepatol.* **2023**, 20, 723-734.
- (4) Guglietta, S.; Li, X.; Saxena, D. Role of Fungi in Tumorigenesis: Promises and Challenges. *Annu. Rev. Pathol.: Mech. Dis.* **2025**, 20, 459–482.
- (5) Dohlman, A. B.; Klug, J.; Mesko, M.; Gao, I. H.; Lipkin, S. M.; Shen, X.; Iliev, I. D. A Pan-cancer Mycobiome Analysis Reveals Fungal Involvement in Gastrointestinal and Lung Tumors. *Cell* **2022**, *185*, 3807–3822.
- (6) Riquelme, E.; McAllister, F. Bacteria and fungi: The counteracting modulators of immune responses to radiation therapy in cancer. *Cancer Cell* **2021**, *39*, 1173–1175.
- (7) Saftien, A.; Puschhof, J.; Elinav, E. Fungi and Cancer. Gut 2023, 72. 1410.
- (8) Narunsky-Haziza, L.; Sepich-Poore, G. D.; Livyatan, I.; Asraf, O.; Martino, C.; Nejman, D.; Gavert, N.; Stajich, J. E.; Amit, G.; González, A.; Wandro, S.; Perry, G.; Ariel, R.; Meltser, A.; Shaffer, J. P.; Zhu, Q.; Balint-Lahat, N.; Barshack, I.; Dadiani, M.; Gal-Yam, E. N.; Patel, S. P.; Bashan, A.; Swafford, A. D.; Pilpel, Y.; Knight, R.; Straussman, R. Pan-cancer Analyses Reveal Cancer-type-specific Fungal Ecologies and Bacteriome Interactions. *Cell* **2022**, *185*, 3789—3806.
- (9) Liang, S.-H.; Sircaik, S.; Dainis, J.; Kakade, P.; Penumutchu, S.; McDonough, L. D.; Chen, Y.-H.; Frazer, C.; Schille, T. B.; Allert, S.; Elshafee, O.; Hänel, M.; Mogavero, S.; Vaishnava, S.; Cadwell, K.; Belenky, P.; Perez, J. C.; Hube, B.; Ene, I. V.; Bennett, R. J. The Hyphal-specific Toxin Candidalysin Promotes Fungal Gut Commensalism. *Nature* **2024**, *627*, *620*–*627*.
- (10) Romo, J. A.; Lopez-Ribot, J. L. Candidalysin: An Unlikely Aide for Fungal Gut Commensalism. *Cell Host Microbe* **2024**, 32, 625–626.
- (11) Müller, R.; König, A.; Groth, S.; Zarnowski, R.; Visser, C.; Handrianz, T.; Maufrais, C.; Krüger, T.; Himmel, M.; Lee, S.; Priest, E. L.; Yildirim, D.; Richardson, J. P.; Blango, M. G.; Bougnoux, M.-E.; Kniemeyer, O.; d'Enfert, C.; Brakhage, A. A.; Andes, D. R.; Trümper, V.; Nehls, C.; Kasper, L.; Mogavero, S.; Gutsmann, T.; Naglik, J. R.; Allert, S.; Hube, B. Secretion of the Fungal Toxin Candidalysin is Dependent on Conserved Precursor Peptide Sequences. *Nat. Microbiol.* **2024**, *9*, 669–683.
- (12) Jin, R.; Neufeld, L.; McGaha, T. L. Linking macrophage metabolism to function in the tumor microenvironment. *Nat. Cancer* **2025**, *6*, 239–252.
- (13) Lorenz, M. C.; Fink, G. R. The glyoxylate cycle is required for fungal virulence. *Nature* **2001**, *412*, 83–86.
- (14) Lesbats, J.; Brillac, A.; Reisz, J. A.; Mukherjee, P.; Lhuissier, C.; Fernández-Monreal, M.; Dupuy, J.-W.; Sequeira, A.; Tioli, G.; De La Calle Arregui, C.; Pinson, B.; Wendisch, D.; Rousseau, B.; Efeyan, A.; Sander, L. E.; D'Alessandro, A.; Garaude, J. Macrophages recycle phagocytosed bacteria to fuel immunometabolic responses. *Nature* 2025, 640, 524–533.
- (15) Riviello, A.; Brenner, D. Bacteria-derived nutrient recycling: How phagocytosed bacteria regulate macrophage metabolism. *Cell Metab.* **2025**, *37*, 1046–1048.
- (16) Leonardi, I.; Gao, I. H.; Lin, W.-Y.; Allen, M.; Li, X. V.; Fiers, W. D.; De Celie, M. B.; Putzel, G. G.; Yantiss, R. K.; Johncilla, M.; Colak, D.; Iliev, I. D. Mucosal fungi promote gut barrier function and social behavior via Type 17 immunity. *Cell* **2022**, *185*, 831–846.
- (17) Denk, D.; Ramakrishnan, M.; Conche, C.; Pallangyo, C.; Pesic, M.; Ceteci, F.; Kennel, K. B.; Kirisözü, A. C.; Engel, E.; Mohs, K.; Ritter, B.; Pardo, A. M.; Özkurt, E.; Hildebrand, F.; Waisman, A.; Arkan, M. C.; Greten, F. R. IL-17RA signaling provides dual tumor-suppressor function during late-stage colorectal carcinogenesis. *Immunity* **2025**, 58, 701–715.
- (18) Netea, M. G.; Joosten, L. A. B.; van der Meer, J. W. M.; Kullberg, B.-J.; van de Veerdonk, F. L. Immune defence against Candida fungal infections. *Nat. Rev. Immunol.* **2015**, *15*, 630–642.
- (19) Erwig, L. P.; Gow, N. A. R. Interactions of fungal pathogens with phagocytes. *Nat. Rev. Microbiol.* **2016**, *14*, 163–176.
- (20) Dong, X.; Pan, P.; Zheng, D.-W.; Bao, P.; Zeng, X.; Zhang, X.-Z. Bioinorganic hybrid bacteriophage for modulation of intestinal

- microbiota to remodel tumor-immune microenvironment against colorectal cancer. Sci. Adv. 2020, 6, No. eaba1590.
- (21) Chen, L.; Shen, J.; Kang, Z.; Zhang, Z.; Zheng, Z.; Zhang, L.; Xiao, Z.; Zhang, Q.; Fang, H.; Zhou, J.; Wang, Y.; Yang, Y.; Liu, Z.; Chen, Q. Fusobacterium nucleatum-mimicking nanovehicles to overcome chemoresistance for breast cancer treatment by eliminating tumor-colonizing bacteria. *Chem* **2024**, *10*, 1783–1803.
- (22) Chen, L.; Zhao, R.; Shen, J.; Liu, N.; Zheng, Z.; Miao, Y.; Zhu, J.; Zhang, L.; Wang, Y.; Fang, H.; Zhou, J.; Li, M.; Yang, Y.; Liu, Z.; Chen, Q. Antibacterial Fusobacterium nucleatum-Mimicking Nanomedicine to Selectively Eliminate Tumor-Colonized Bacteria and Enhance Immunotherapy Against Colorectal Cancer. *Adv. Mater.* 2023, 35, 2306281.
- (23) Tso, G. H. W.; Reales-Calderon, J. A.; Tan, A. S. M.; Sem, X.; Le, G. T. T.; Tan, T. G.; Lai, G. C.; Srinivasan, K. G.; Yurieva, M.; Liao, W.; Poidinger, M.; Zolezzi, F.; Rancati, G.; Pavelka, N. Experimental evolution of a fungal pathogen into a gut symbiont. *Science* 2018, 362, 589–595.
- (24) Schikora-Tamarit, M. A.».; Gabaldón, T. Recent gene selection and drug resistance underscore clinical adaptation across Candida species. *Nat. Microbiol.* **2024**, *9*, 284–307.
- (25) Lee, Y.; Puumala, E.; Robbins, N.; Cowen, L. E. Antifungal Drug Resistance: Molecular Mechanisms in Candida albicans and Beyond. *Chem. Rev.* **2021**, *121*, 3390–3411.
- (26) Li, F.; Zhang, X.-Q.; Ho, W.; Tang, M.; Li, Z.; Bu, L.; Xu, X. mRNA lipid nanoparticle-mediated pyroptosis sensitizes immunologically cold tumors to checkpoint immunotherapy. *Nat. Commun.* **2023**, *14*, 4223.
- (27) Zhang, Z.; Pan, Z.; Li, Q.; Huang, Q.; Shi, L.; Liu, Y. Rational design of ICD-inducing nanoparticles for cancer immunotherapy. *Sci. Adv.* **2024**, *10*, No. eadk0716.
- (28) Lee, J.; Choi, S. W.; Park, M.; Um, W.; Kwon, S.; Kim, C. H.; Joo, H.; You, D. G.; Lee, J. A.; Shin, S.; Kang, H.; Ghahari, F.; Kim, J.; Park, J. H. Hematite-embedded mesoporous nanoparticles for ferroptosis-inducing cancer sonoimmunotherapy. *J. Controlled Release* **2025**, 385, 113990.
- (29) Bryan, N. B.; Dorfleutner, A.; Kramer, S. J.; Yun, C.; Rojanasakul, Y.; Stehlik, C. Differential Splicing of the Apoptosis-associated Speck Like Protein Containing a Caspase Recruitment Domain (ASC) Regulates Inflammasomes. *J. Inflammation* **2010**, *7*, 23.
- (30) Borges, J. P.; Sætra, R. S.; Volchuk, A.; Bugge, M.; Devant, P. A.-O.; Sporsheim, B.; Kilburn, B. R.; Evavold, C. L.; Kagan, J. C.; Goldenberg, N. M.; Flo, T. H.; Steinberg, B. E. Glycine inhibits NINJ1 membrane clustering to suppress plasma membrane rupture in cell death. *eLife* **2022**, *11*, No. e78609.
- (31) Lindsay, A. K.; Deveau, A.; Piispanen, A. E.; Hogan, D. A. Farnesol and Cyclic AMP Signaling Effects on the Hypha-to-Yeast Transition in Candida albicans. *Eukaryotic Cell* **2012**, *11*, 1219–1225.
- (32) Hu, J. J.; Liu, X.; Xia, S.; Zhang, Z.; Zhang, Y.; Zhao, J.; Ruan, J.; Luo, X.; Lou, X.; Bai, Y.; Wang, J.; Hollingsworth, L. R.; Magupalli, V. G.; Zhao, L.; Luo, H. R.; Kim, J.; Lieberman, J.; Wu, H. FDA-approved disulfiram inhibits pyroptosis by blocking gasdermin D pore formation. *Nat. Immunol.* **2020**, *21*, 736–745.
- (33) O'Keefe, S. J. D. Diet, Microorganisms and Their Metabolites, and Colon Cancer. *Nat. Rev. Gastroenterol. Hepatol.* **2016**, *13*, 691–706.
- (34) Hsu, C. L.; Schnabl, B. The Gut-Liver Axis and Gut Microbiota in Health and Liver Disease. *Nat. Rev. Microbiol.* **2023**, *21*, 719–733.
- (35) Hernández-Santos, N.; Gaffen, S. L. Th17 Cells in Immunity to Candida albicans. *Cell Host Microbe* **2012**, *11*, 425–435.
- (36) Krishnan, N.; Jiang, Y.; Zhou, J.; Mohapatra, A.; Peng, F.-X.; Duan, Y.; Holay, M.; Chekuri, S.; Guo, Z.; Gao, W.; Fang, R. H.; Zhang, L. A Modular Approach to Enhancing Cell Membrane-coated Nanoparticle Functionality Using Genetic Engineering. *Nat. Nanotechnol.* **2024**, *19*, 345–353.
- (37) Zhu, J.; Xie, R.; Gao, R.; Zhao, Y.; Yodsanit, N.; Zhu, M.; Burger, J. C.; Ye, M.; Tong, Y.; Gong, S. Multimodal Nano-

immunotherapy Engages Neutrophils to Eliminate Staphylococcus aureus Infections. *Nat. Nanotechnol.* **2024**, *19*, 1032–1043.

- (38) Deng, R.; Zhao, R.; Zhang, Z.; Chen, Y.; Yang, M.; Lin, Y.; Ye, J.; Li, N.; Qin, H.; Yan, X.; Shi, J.; Yuan, F.; Song, S.; Xu, Z.; Song, Y.; Fu, J.; Xu, B.; Nie, G.; Yu, J.-K. Chondrocyte Membrane—coated Nanoparticles Promote Drug Retention and Halt Cartilage Damage in Rat and Canine Osteoarthritis. Sci. Transl. Med. 2024, 16, No. eadh9751.
- (39) Zhao, Y.; Li, Q.; Niu, J.; Guo, E.; Zhao, C.; Zhang, J.; Liu, X.; Wang, L.; Rao, L.; Chen, X.; Yang, K. Neutrophil Membrane-Camouflaged Polyprodrug Nanomedicine for Inflammation Suppression in Ischemic Stroke Therapy. *Adv. Mater.* **2024**, *36*, 2311803.
- (40) Li, B.; Wang, W.; Zhao, L.; Wu, Y.; Li, X.; Yan, D.; Gao, Q.; Yan, Y.; Zhang, J.; Feng, Y.; Zheng, J.; Shu, B.; Wang, J.; Wang, H.; He, L.; Zhang, Y.; Pan, M.; Wang, D.; Tang, B. Z.; Liao, Y. Photothermal Therapy of Tuberculosis Using Targeting Pre-activated Macrophage Membrane-coated Nanoparticles. *Nat. Nanotechnol.* **2024**, *19*, 834–845.
- (41) Azevedo Portilho, N.; Saini, D.; Hossain, I.; Sirois, J.; Moraes, C.; Pastor, W. A. The DNMT1 Inhibitor GSK-3484862 Mediates Global demethylation in Murine Embryonic Stem Cells. *Epigenet. Chromatin* **2021**, *14*, 56.



A Candidalysin-Neutralizing Nanomodulator Enhances Colorectal Cancer Immunotherapy by Targeting Fungi-Macrophage Crosstalk

Yu Yan, ¹⁺ Kai Zhao, ¹⁺ Shan-Shan Pan, ¹ Yu-Liang Sun, ¹ Zhi-Yong Rao, ¹ Xian-Zheng Zhang ^{1*}

¹ Key Laboratory of Biomedical Polymers of Ministry of Education & Department of Chemistry, Wuhan University, Wuhan 430072, P. R. China

This file includes:

- > Experimental materials and methods
- Figure S1-S43
- > Table S1, S2

^{*} Corresponding author. E-mail address: xz-zhang@whu.edu.cn (X. Z. Zhang)

⁺ These authors contributed equally.

Experimental materials and methods

Materials. Triethylamine, 1-Hexanol, 1-Octanol, 1-Decanol, 1-Dodecanol, 1-Tetradecanol, 1-Hexadecanol, Osmium (VIII) oxide were purchased from Aladdin Biochemical Technology. GSK-3484862, X-GAL (BCIG), (Isopropyl β-D-thiogalactoside) IPTG were purchased from MedChemExpress. Enzyme-linked immunosorbent assay (ELISA) kits for IL-1β (CME0015-096), TGFβ (CME0020-096), TNFα (CME0004-096), IFN-γ (CME0003-096), IL-6 (CME0006-096) were purchased from 4A Biotech. Enzyme-linked immunosorbent assay (ELISA) kits for IL-10 (ELK1143), IL-12p70 (ELK9395), GZMB (ELK1660), IL-17 (ELK1147) were purchased from ELK Biotechnology. Cell Membrane Protein Extraction Kit (EX1500) and Lacate dehydrogenase (LDH) Activity Assay Kit (BC0680) were purchased from Solarbio life science. Cell Counting Kit-8 (CCK-8) (KTA1020) was purchased from Abbkine, Wuhan, China. Recombinant mouse GM-CSF was obtained from Chamot Biotechnology Co., Ltd. Recombinant mouse M-CSF was obtained from Peprotech. GSDMD N-Terminal antibody (DF13758) was purchased from Affinity biosciences. Jiangsu. Caspase-1 antibody (Cat #89332) was purchased from Cell Signaling Technology. TLR2 (A19125) was purchased from ABclonal. TLR4 (30400-1-AP) was purchased from Proteintech. Dectin-1 (PA5-97284) was purchased from Thermo Fisher. Mannose receptor antibody (Cat #24595) was purchased from Cell Signaling Technology. In vivo MAb anti-mouse PD-1 (Cat# BE0146, Clone# RMP1-14) was purchased from BioXCell.

Cell lines and bacteria strains. CT26 cells, J774A.1 cells, and RAW264.7 cells were provided by China Center for Type Culture Collection. CT26 cells were cultured in RPM1 1640 medium supplemented with 10% FBS and 100 U ml⁻¹ penicillin-streptomycin, 5% CO₂ 95% air, and 37 degrees Celsius. J774A.1 cells and RAW264.7 cells were cultured in RPM1 DMEM medium supplemented with 10% inactivated FBS and 100 U ml⁻¹ penicillin-streptomycin, 5% CO₂ 95% air, and 37 degrees Celsius. *Candida albicans* ATCC 10231 was purchased from Guangdong Provincial Center for Microbiological Culture Collection and cultured in PDB medium at 30°C with shaking.

Mycelium of *C. albicans* was obtained by induction with 10% FBS for 12 h, and yeast morphology was obtained by induction with farnesol for 12 h.

Synthesis of C12-GE. The peptide C12-GE was synthesized using standard Fmoc-based solid-phase peptide synthesis (SPPS) on Wang resin. Wang resin (1 g, 0.5 mmol g⁻¹ loading) was pre-swollen and functionalized with Fmoc-Cys(Trt)-OH (1 g) in the presence of HOBt (1 g), DMAP (0.2 g), and DIC (1 ml, Cat#1040091, Leyan, Shanghai, China) under nitrogen for ≥6 h. Completion was confirmed by a negative ninhydrin test. The Fmoc protective group was removed with 20% piperidine in DMF (2 × 15 min), as indicated by a positive ninhydrin assay. Each amino acid was coupled sequentially using activated Fmoc-protected residues and standard DIC/HOBt chemistry until the full peptide sequence was assembled. Dodecanoic acid (1 g) was coupled to the N-terminus using DIC and HOBt (0.5 ml, 0.5 g) for 2 h. A colorless ninhydrin result confirmed completion of C12 attachment. The peptide was cleaved from the resin using TFA, precipitated in ice-cold diethyl ether, and collected by centrifugation. The crude product was purified by preparative LC-MS and lyophilized to yield C12-GE.

Synthesis of PGC. 100 mg of Mal-PEG_{2K}-OH was dissolved in 3 ml DMF, followed by addition of 1.1 equivalents of C12-GE and 3 equivalents of triethylamine. The reaction proceeded at room temperature for 12 hours. The reaction mixture was then transferred to a 1000 Da dialysis membrane and dialyzed against ultrapure water for 24 hours. The dialysate was collected and lyophilized to yield the PEG-C12-GE conjugate (PGC). Successful synthesis was confirmed by ¹H NMR spectroscopy analysis, which verified characteristic proton peaks corresponding to both PEG and the C12-GE moiety.

Preparation and characterization of HM-PGC@GSK. 10 mg PGC and 1mg GSK were codissolved in DMSO and slowly added to phosphate-buffered saline (PBS) under ultrasonic conditions to form PGC@GSK nanoparticles. For macrophage membrane (HM) preparation, RAW 264.7 cells were co-cultured with *C. albicans* hyphae at an MOI of 1 for 12 hours. Cells were then collected, and

pretreatment macrophage membranes were isolated using a commercial cell membrane protein extraction kit (Solarbio) and subsequently lyophilized. The PGC@GSK nanoparticles and HM were mixed in a 1:1 mass ratio and subjected to successive extrusion through 800 nm, 400 nm, and 200 nm polycarbonate membranes (20–30 passes) using an Avanti liposome extruder, yielding the HM-PGC@GSK formulation. Particle size distribution and zeta potential were characterized using a Zetasizer (Nano ZS, Malvern Instruments), and nanoparticle morphology was visualized via transmission electron microscopy (JEOL JEM-2100 at 200 kV).

Different length fatty alcohol chains induce morphological changes in *C. albicans*. *C. albicans* was activated overnight at 37 °C in potato dextrose broth (PDB), then diluted the following day in fresh medium to an OD₆₀₀ of 0.6. DMSO solutions of C6OH, C8OH, C10OH, C12OH, C14OH, and C16OH were each added to a final concentration of 50 μM. After 12 hours of incubation, morphological changes in *C. albicans* were assessed via light microscopy.

Preparation of Bone marrow–derived macrophages (BMDMs). C57BL/6 mice were euthanized by cervical dislocation, surface-sterilized with 70% ethanol, and carefully dissected to expose the hind limbs. The femurs and tibias were isolated by excising proximal and distal ends near the hip and knee joints. Marrow was flushed from each bone using 2–3 ml PBS per bone, and the resulting cell suspension was collected by centrifugation. Red blood cells were lysed using an RBC lysis buffer, followed by PBS washes and pellet recovery. Cells were then cultured in DMEM supplemented with 10% FBS and 50 ng ml⁻¹ M-CSF for 7 days to generate BMDMs. Differentiation was confirmed by flow cytometry. Mature BMDMs were cryopreserved in Kryogene cell therapeutic cryopreservation solution (Milecell Biological Science & Technology Co., Ltd.) and stored in liquid nitrogen for future experiments

BMDMs pyroptosis assay and activation assay in vitro. BMDMs and *C. albicans* were co-cultured at a multiplicity of infection (MOI) of 1. Experimental treatments included PC, PGC, PGC@GSK, and HM-PGC@GSK, each at a polymer concentration of 50 µg ml⁻¹. After 24 hours of incubation,

we evaluated macrophage cytotoxicity through LDH release and IL-1β secretion assays, and assessed cell viability using Calcein-AM/PI staining. Additionally, flow cytometry was performed to quantify the polarization ratio of M1 to M2 macrophage subpopulations.

Splenocyte activation and killing assay. Mouse spleen cells were isolated from BALB/c mice as follows: following cervical dislocation, spleens were harvested and mechanically dissociated through a 70 μm cell strainer using the plunger of a syringe. The strainer was rinsed with PBS containing 2% FBS to collect a single-cell suspension, which was then centrifuged at 300 g for 5 minutes. Red blood cells were lysed using an erythrocyte lysis buffer, and the remaining splenocytes were collected. CT26 tumor cells were seeded and infected with *Candida albicans* at an MOI of 0.1. Treatment groups included PC, PGC, PGC@GSK, and HM-PGC@GSK, each at a polymer concentration of 50 μg ml⁻¹, and incubated for 2 hours. Subsequently, freshly isolated splenocytes were added at an effector-to-target (E:T) ratio of 1:1. After 24 hours of co-culture, splenocyte immunophenotyping was performed via flow cytometry, and CT26 tumor cell viability at the bottom of the well was assessed using a CCK-8 assay to evaluate T cell-mediated cytotoxicity.

Phage display assay. Coat an ELISA plate with *Candidalysin* at 50 μg ml⁻¹ and incubate at 4°C overnight. Discard the coating solution and block with 5% skim milk powder at 37°C for 1 hour. After blocking, add 50 μl of 5% skim milk powder and 50 μl of phage supernatant, and incubate at 37°C for 2 hours. Elute the mixture with 100 μl of 0.2M Gly-HCl (pH 2.2) for 8 minutes, then neutralize with 15 μl of 1M Tris-HCl (pH 9.1). Dilute 10 μl of the neutralization solution 1000, 10000, and 100000 times, then infect 1 ml of ER2738 (OD600 = 0.6) at 37°C for 5 minutes. After infection, add to 3 ml of 50°C top culture medium, mix, and pour onto 2YT/IPTG/Xgal plates for overnight incubation at 37°C. The following day, count the blue spots on the plate and calculate the number of recovered phages. Elute phages were then infected into 40 ml of ER2738 (1:100 inoculation after overnight shaking), incubated at 37°C for 5 hours, and centrifuged at 12,000 g for 10 minutes to remove precipitates. The supernatant was mixed with 1/6 volume of 20% PEG/2.5M NaCl and

allowed to stand at 4°C for 2 hours. After centrifugation at 12,000 g for 15 minutes at 4°C, discard the supernatant, resuspend the precipitate in 1 ml of culture medium, and repeat the process twice to complete three rounds of screening.

After the third round of screening, the eluted phages were used to infect *Escherichia coli*, followed by the addition of 3 mL of 50°C top culture medium. The mixture was then plated onto 2YT/IPTG/Xgal medium and incubated at 37°C overnight. Blue spot monoclones were picked with a pipette tip, inoculated into a 96-well plate, and cultured at 37°C for 5 hours. Phages were subsequently harvested by centrifugation. *Candidalysin* was coated onto the ELISA plate at 500 ng well⁻¹, and blocked with 5% PBSM at 37°C for 1 hour. Then, 50 μl of 5% PBSM and 50 μl of the phage supernatant obtained in step 3 were added to each well and incubated at 37°C for 1 hour. After washing, anti-P8/HRP phage secondary antibody was added and incubated at 37°C for 40 minutes. Following another wash, 100 μl of TMB substrate was added, and the reaction was terminated after 15 minutes in the dark. The positive sequences were identified based on the microplate reader readings.

Biological transmission electron microscopy assay. After induced mature BMDMs were cocultured with PBS, *Candida albicans*, and *Candida albicans* + C12-GE (10 μg ml⁻¹) for 12 hours, the
cells from each treatment group were collected into 1.5 mL EP tubes and centrifuged at 300 g for 10
minutes. The supernatant was carefully discarded, and 1 ml of 2.5% glutaraldehyde fixative (at room
temperature) was added slowly. The cells were fixed in the dark at room temperature for 15 minutes.
After fixation, the cells were centrifuged again, embedded in 1% agarose solution, and further fixed
with 1% osmium tetroxide in 0.1 M phosphate buffer (pH 7.4) for 2 hours at room temperature.
Following fixation, the cells underwent dehydration through an alcohol and acetone gradient,
infiltrated and embedded, and polymerized into resin blocks for sectioning. The prepared sections
were subsequently imaged using a transmission electron microscope (HITACHI, HT7700, 120 kV)
to examine the lysosomal morphology in detail.

FISH staining assay. For cell samples, cells on the slide (SAINING Biotechnology) were fixed with in situ hybridization fixative for 20 minutes, rinsed with PBS three times, and incubated with prehybridization solution at 37°C for 1 hour. Subsequently, the cells were hybridized overnight with a hybridization solution containing the probe in an incubator. After washing with SSC buffer, normal rabbit serum was added and incubated at room temperature for 30 minutes to block nonspecific binding. Following the addition of Du.al 1249, the cells were incubated at 37°C for 50 minutes, rinsed three times with PBS, and the corresponding tyramide signal amplification (TSA) reagent was applied. After incubation in the dark at room temperature for 10 minutes, the cells were washed with TBST, and imaging was performed using confocal laser scanning microscopy (CLSM).

For tissue samples, specific tissues were fixed with in situ hybridization fixative for 12 hours, dehydrated through an ethanol gradient, and embedded in immersion wax. After dewaxing tissue sections by graded water immersion, antigen retrieval was performed by autoclaving with EDTA (pH 9.0). The sections were then incubated with 3% methanol-H₂O₂ solution at room temperature in the dark for 15 minutes to block endogenous peroxidase activity. FISH staining was then conducted following the same procedure as for the cell samples, and the sections were observed and photographed using CLSM. The FISH probe sequences targeting *C. albicans* used in this article are shown in Table S2.

Transcriptomic analysis. After induced mature BMDMs were co-cultured with PBS, *C. albicans*, and *C. albicans*+C12-GE (10 μg ml⁻¹) for 12h, the supernatant was removed and washed three times with PBS. After trypsin digestion, the cells at the bottom of the plate were collected, the supernatant was removed by centrifugation, and the cells were washed three times with PBS. The cell pellets were collected by centrifugation. The cell pellets were homogenized by pipetting at a ratio of 1 ml TRIzol per 5×10⁶ cells, and 1 ml per tube was dispensed into pre-cooled RNase-free cryotubes, frozen in liquid nitrogen for 0.5 h, and then transferred to -80°C for storage. High-throughput sequencing was completed by Majorbio BioTech Co., Ltd., and transcriptome data were analyzed online using the

ISanger cloud platform (https://cloud.majorbio.com).

Animal experiments. The animal experiments were approved by the Institutional Animal Care and Use Committee of the Animal Experiment Center/A3 Laboratory of Wuhan University, and all animal experiments were conducted in accordance with the Guidelines for Animal Experimentation of the Animal Experiment Center/A3 Laboratory of Wuhan University.

For the *Candida albicans*-induced subcutaneous colorectal cancer (CRC) progression model, BALB/c mice were subcutaneously inoculated with 2×10⁶ CT26 cells on the right flank. When the tumor volume reached approximately 100 mm³ on day 0, the tumor-bearing mice were randomly assigned to six groups, with six mice per group. Normal saline or *C. albicans* (1×10⁷ cells per mouse) was administered intratumorally. The treatment cycle was every 2 days, with a total of three administrations. Tumor volume changes were monitored during the course of the experiment, and tumor tissues and major organs were harvested on day 24 for histological analysis.

For the subcutaneous CRC mouse model, BALB/c mice were subcutaneously inoculated with 2×10⁶ CT26 cells on day 0. When the tumor volume reached approximately 100 mm³ on day 7, the tumor-bearing mice were randomly divided into six groups, with six mice in each group. A 100 µl injection of PBS, PC, PGC, PGC@GSK, or HM-PGC@GSK (polymer concentration of 500 µg ml¹) was administered via tail vein injection every 3 days, for a total of three doses. Tumor volume changes were monitored throughout the study, and tumor tissues and major organs were collected on day 28 for histological analysis.

For the orthotopic CRC mouse model, BALB/c mice were inoculated with 5×10⁶ CT26-luc cells on the cecal wall, 7 days prior to treatment. Tumor growth was monitored using an IVIS system (Perkin Elmer) following intraperitoneal injection of d-luciferin. On day 0, mice with orthotopic colorectal cancer were randomly assigned to six groups, with six mice per group. A 100 μl injection of PBS, PC, PGC, PGC@GSK, or HM-PGC@GSK (polymer concentration of 500 μg ml⁻¹) was administered via tail vein, and αPD-1 antibody (50 μg per mouse) was given intraperitoneally, with a

dosing cycle every 3 days for a total of three doses. Tumor volume was continuously monitored throughout the study.

This study adhered to the maximum tumor burden limits set by the ethics committee. Mice exhibiting a significant weight loss (≥ 15% of their baseline weight) or displaying clinical signs of distress, such as abdominal distention, severe lethargy, or respiratory distress, were considered to be in a moribund state and were immediately euthanized according to humane endpoint guidelines.

Tumor tissue flow cytometry assay. In the subcutaneous CRC mouse model, tumor tissues, spleens, and inguinal lymph nodes were collected on day 28 after treatment. In the orthotopic CRC model, spleens were harvested from mice on day 16. Tumor tissues were enzymatically digested with type IV collagenase (1 mg ml⁻¹), hvaluronidase (1 mg ml⁻¹), and DNase I (10 ug ml⁻¹), and inguinal lymph nodes and spleens were mechanically disrupted with PBS containing 2% FBS to prepare single-cell suspensions. The collected cells were then stained with specific fluorescent-labeled antibodies, including: dendritic cells (fluorescein isothiocyanate (FITC) anti-mouse CD11c antibody, phycoerythrin (PE) anti-mouse CD80 antibody, allophycocyanin (APC) anti-mouse CD86 antibody), T cells (FITC anti-mouse CD3 antibody, APC anti-mouse CD4 antibody, PE anti-mouse CD8a antibody), Th17 T cells (FITC anti-mouse CD3 antibody, APC anti-mouse IL-17αantibody, PE antimouse CD8a antibody), exhausted T cells (FITC anti-mouse CD8 antibody, APC anti-mouse PD-1 antibody, PE anti-mouse TIM-3 antibody), M1 macrophages (PE anti-mouse CD11b antibody, APC anti-mouse F4/80 antibody, FITC anti-mouse CD86 antibody), MDSCs (APC anti-mouse CD11b antibody, PE anti-mouse CD45 antibody, FITC anti-mouse Gr-1 antibody), Treg cells (FITC antimouse CD3 antibody, APC anti-mouse CD4 antibody, PE anti-mouse Foxp3 antibody) and memory T cells (FITC anti-mouse CD8a antibody, APC anti-mouse CD62L antibody, PE anti-mouse CD44 antibody). The above fluorescent antibodies were purchased from Biolegend. Flow cytometry FCM was performed by BD Accuri C6, and FlowJo software was used for data processing and analysis.

otherwise specified. Data analysis was conducted using GraphPad Prism 9.0 software. Statistical significance was evaluated using unpaired two-tailed Student's t-test, one-way ANOVA, or two-way ANOVA with Tukey's post hoc corrections, with a p-value of < 0.05 considered statistically significant. All experiments, including immunohistochemistry, immunofluorescence, H&E staining, western blotting, transmission electron microscopy (TEM), gel electrophoresis, and FISH staining, were independently performed at least three times, yielding consistent results.

Schematics. Schematics were created with Adobe Illustrator and Biorender.com.

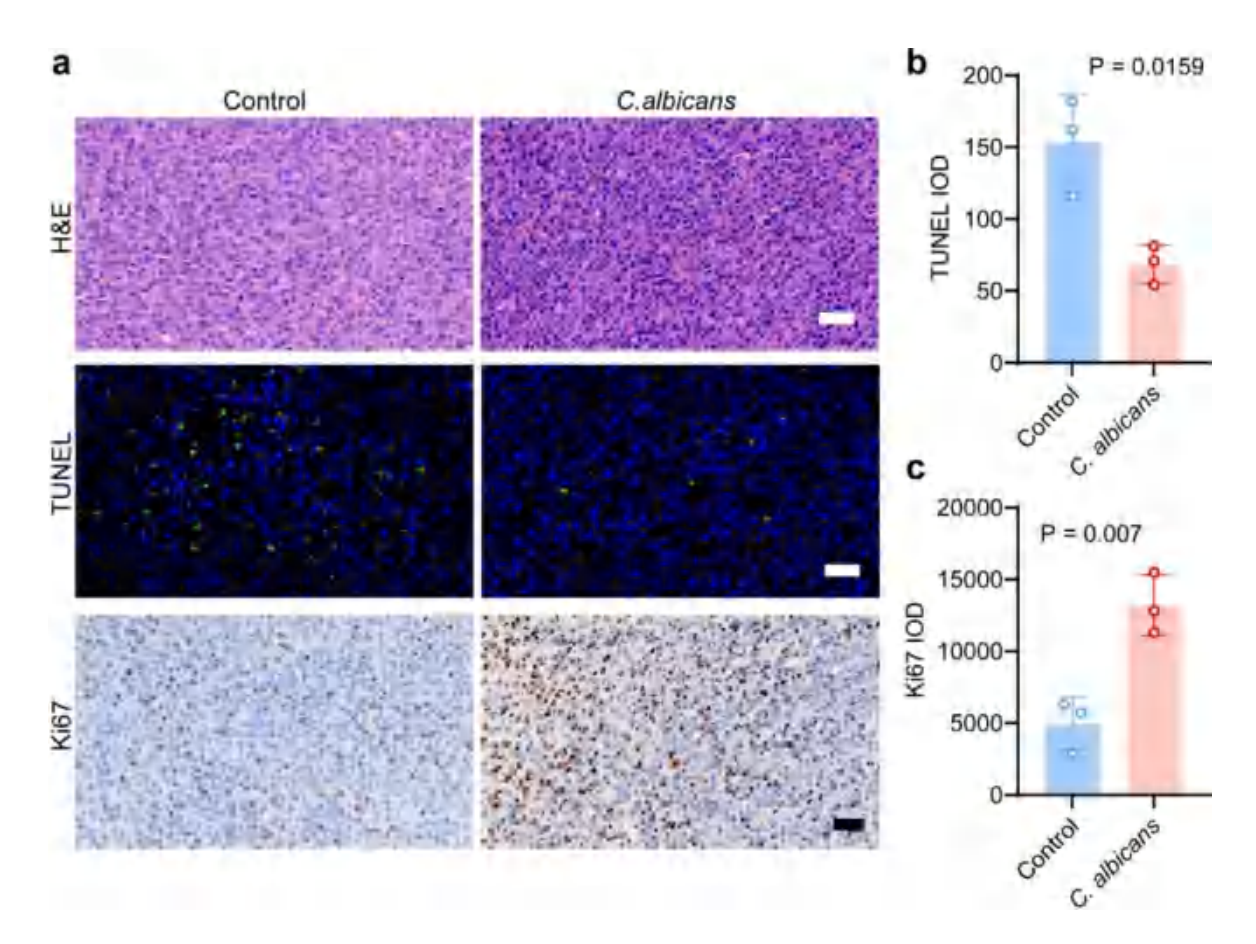


Figure S1. Histological analysis of subcutaneous tumors in mice following *C. albicans* administration. a, Representative images of H&E staining, TUNEL, and Ki67 staining of tumor tissues from mice treated with and without *C. albicans*. Scale bar, 50 μ m. b-c, Quantitative analysis of Figure S1a by Aipathwell. n = 3 independent samples. Data are presented as mean \pm s.d. Statistical significance was determined by unpaired two-tailed Student's t-test (b, c).

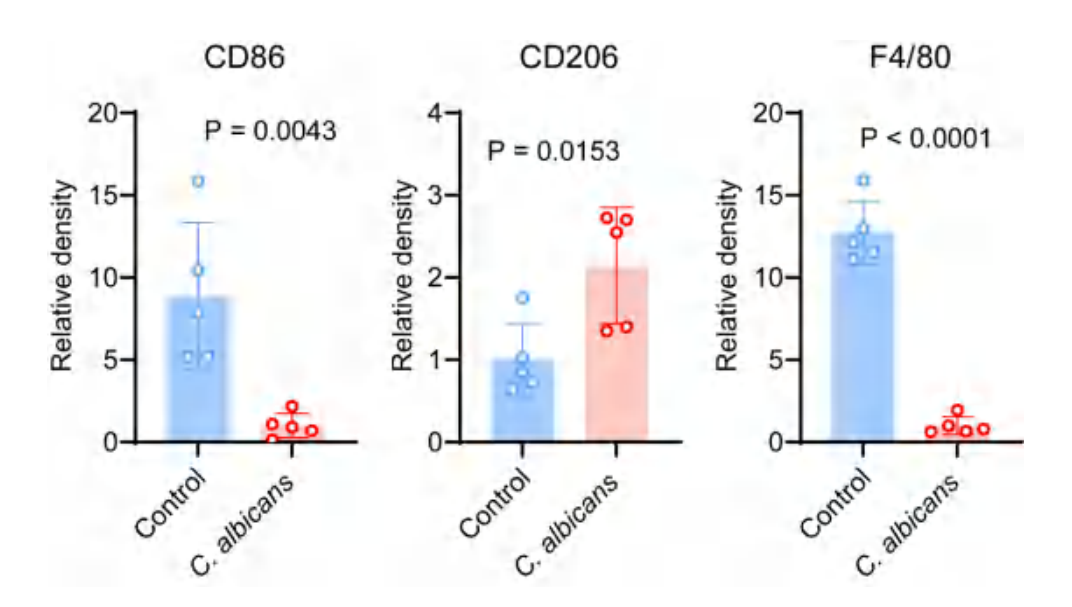


Figure S2. The quantitative analysis of Figure 2d. n = 5 independent samples. Data are presented as mean \pm s.d. Statistical significance was determined by unpaired two-tailed Student's t-test.

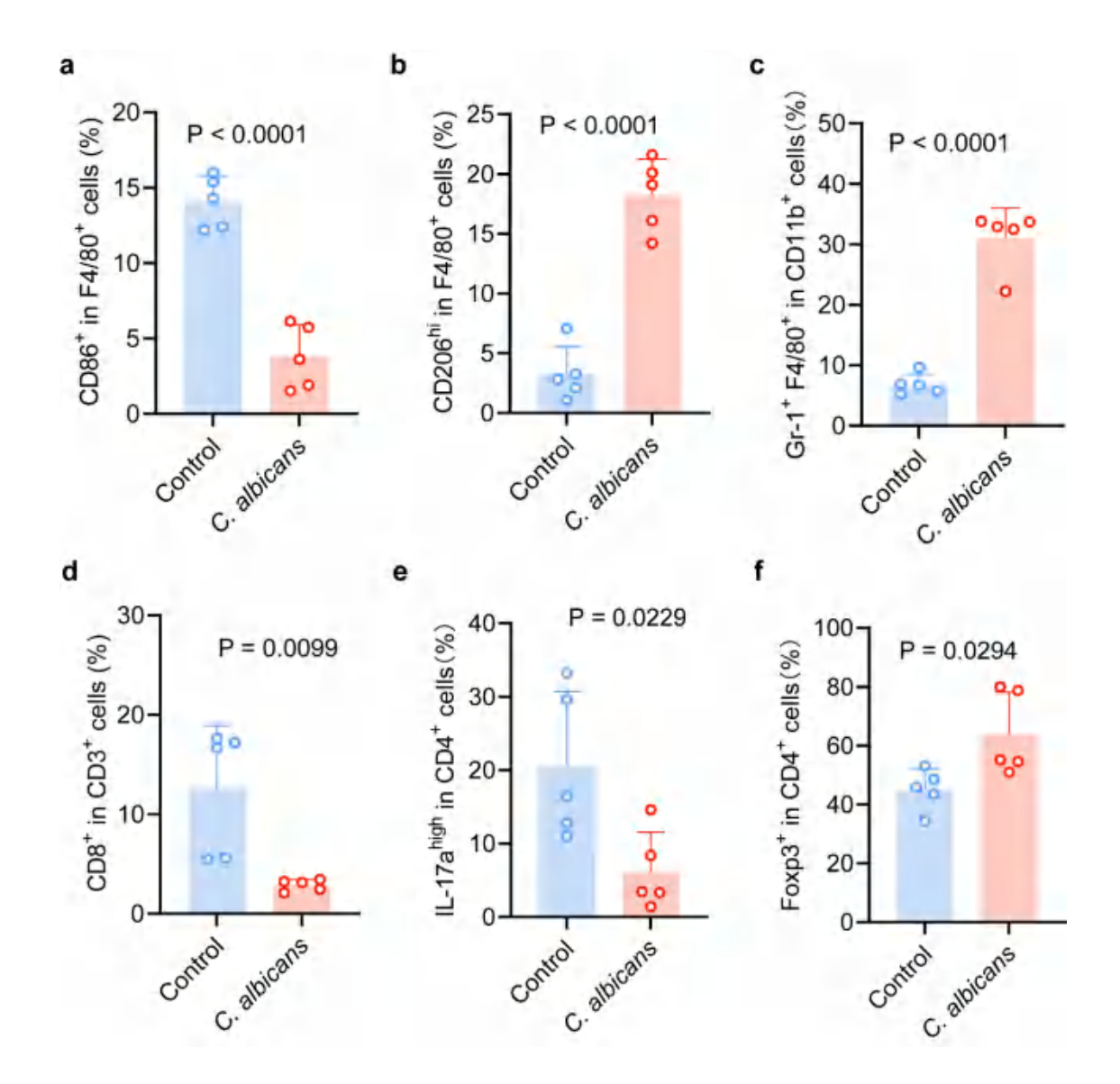


Figure S3. Quantitative statistical analysis of M1 macrophages (CD86⁺ in CD11b⁺ F4/80⁺ cells) (a), M2 macrophages (CD206⁺ in CD11b⁺ F4/80⁺ cells) (b), MDSCs (Gr-1⁺ F4/80⁺ in CD11b⁺ cells) (c), CD8⁺ cytotoxic T cells (CD8⁺ in CD3⁺ cells) (d), Th17 (CD4⁺ IL-17a⁺ in CD3⁺ cells) (e) and Treg (CD4⁺ Foxp3⁺ in CD3⁺ cells) (f) in tumor tissues of mice treated with or without *C. albicans*. n = 5 independent samples. Data are presented as mean \pm s.d. Statistical significance was determined by unpaired two-tailed Student's t-test.

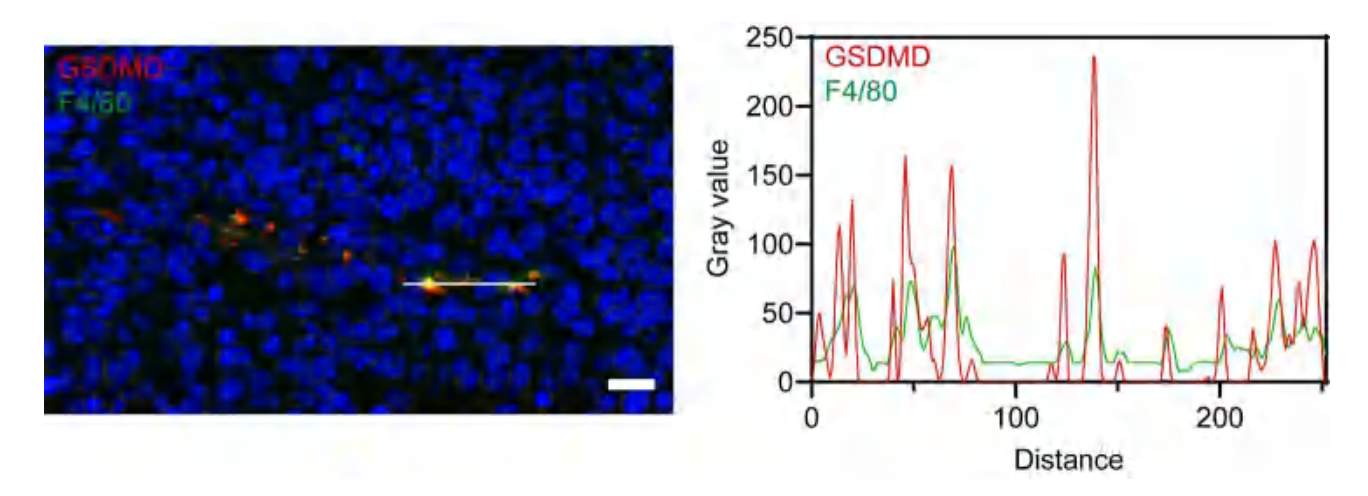


Figure S4. The graph showing the distribution of red and green fluorescence intensities along the line in Figure 2h. The Pearson's R value of red and green fluorescence calculated using ImageJ Coloc 2 was 0.71.

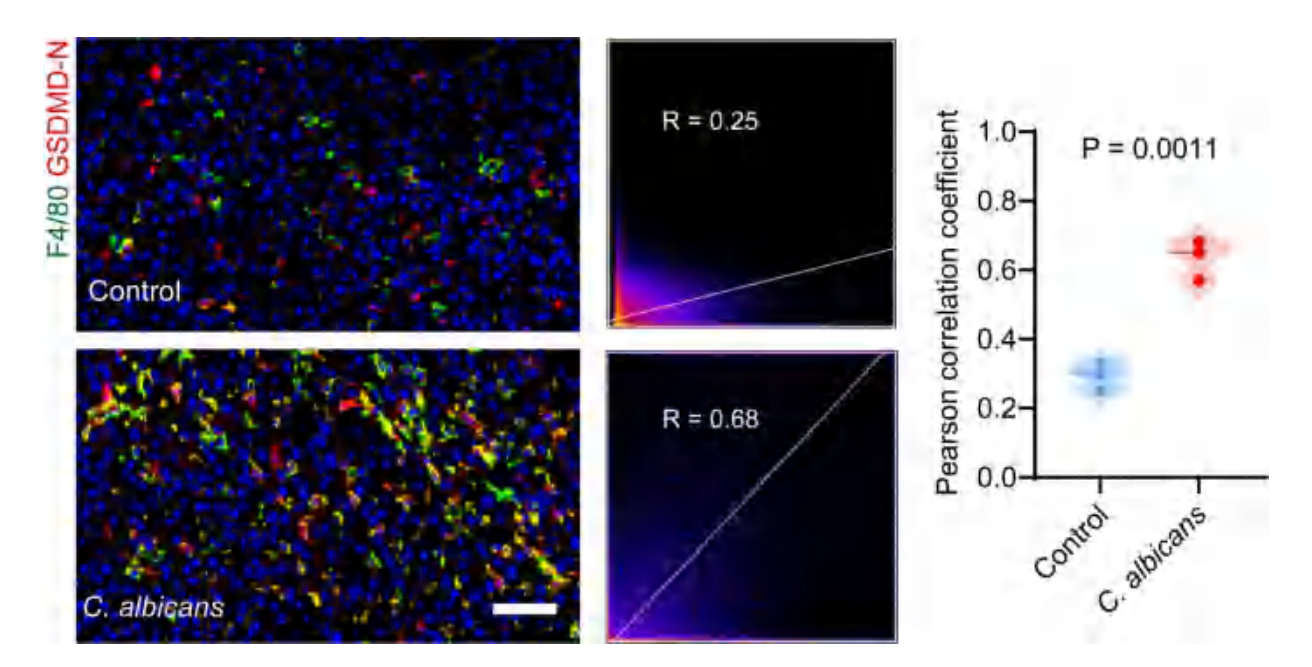


Figure S5. Representative immunofluorescence images showing co-expression of F4/80 and GSDMD-N in CRC tumor tissues after different treatments and the quantitative colocalization analysis by ImageJ Coloc 2. Scale bar, $50 \mu m$. n = 3 independent samples. Data are presented as mean \pm s.d. Statistical significance was determined by unpaired two-tailed Student's t-test.

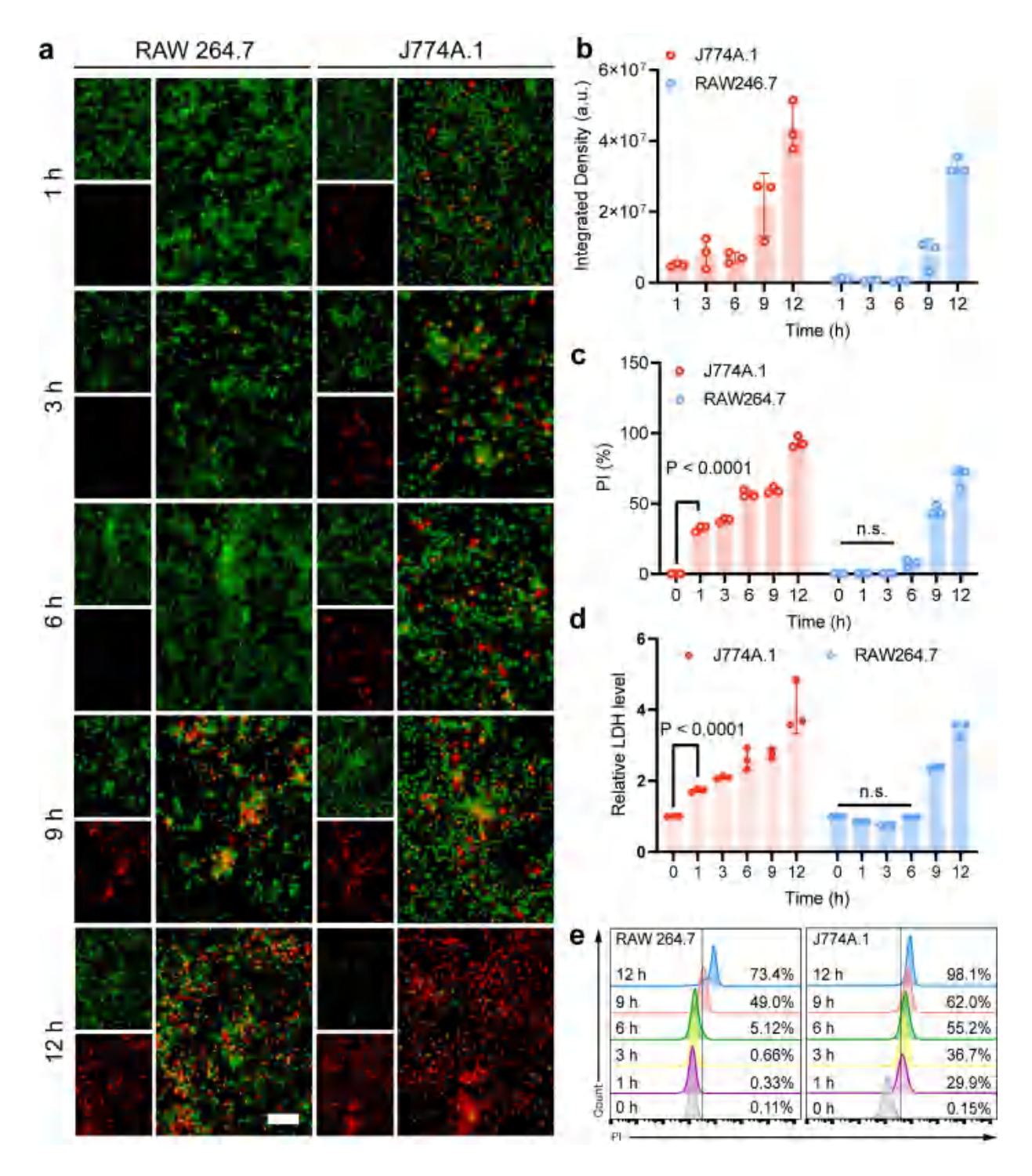


Figure S6. a, Representative CLSM images of Calcein/PI staining of in macrophages co-incubated with *C. albicans* for varying time intervals. b-c, Flow cytometry analysis of PI staining intensity (b) and positive rate (c) of two macrophages co-incubated with *C. albicans* for different time periods. n = 3 independent samples. d, Quantitative analysis of LDH released by two macrophages co-incubated with *C. albicans* for different time periods. n = 3 independent samples. e, Representative FCM images

of PI staining. Data are presented as mean \pm s.d. Statistical significance was determined by two-way ANOVA with Tukey's post hoc corrections (b, c, d).

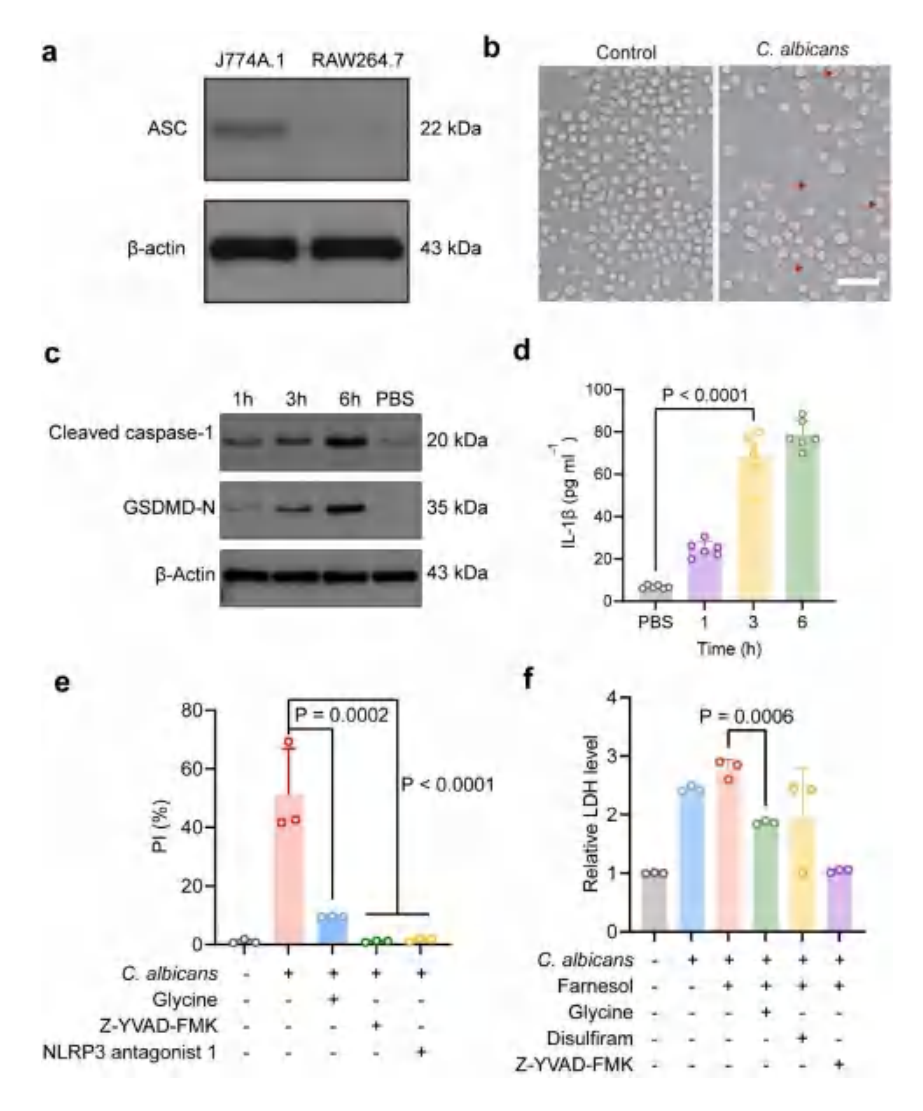


Figure S7. *C. albicans* induces pyroptosis in macrophages. a, Expression of endogenous ASC in J774A.1 and RAW264.7 macrophages. b, Representative bright field images following co-culture of J774A.1 macrophages with *C. albicans*. c, Expression of cleaved caspase-1 and GSDMD-N in J774A.1 after co-culture with *C. albicans* at different time points. d, Quantitative analysis of IL-1β secretion from J774A.1 following co-culture with *C. albicans* during different time. n = 5 independent samples. e, Quantitative analysis of PI positivity in macrophages while co-culturing with *C. albicans* in the presence of different inhibitors. n = 3 independent samples. f, Quantitative analysis of LDH release from macrophages co-cultured with *C. albicans* in various states, in the presence of different inhibitors n = 3 independent samples. Data are presented as mean \pm s.d. Statistical significance was determined by one-way ANOVA with Tukey's post hoc correction (d, e, f).

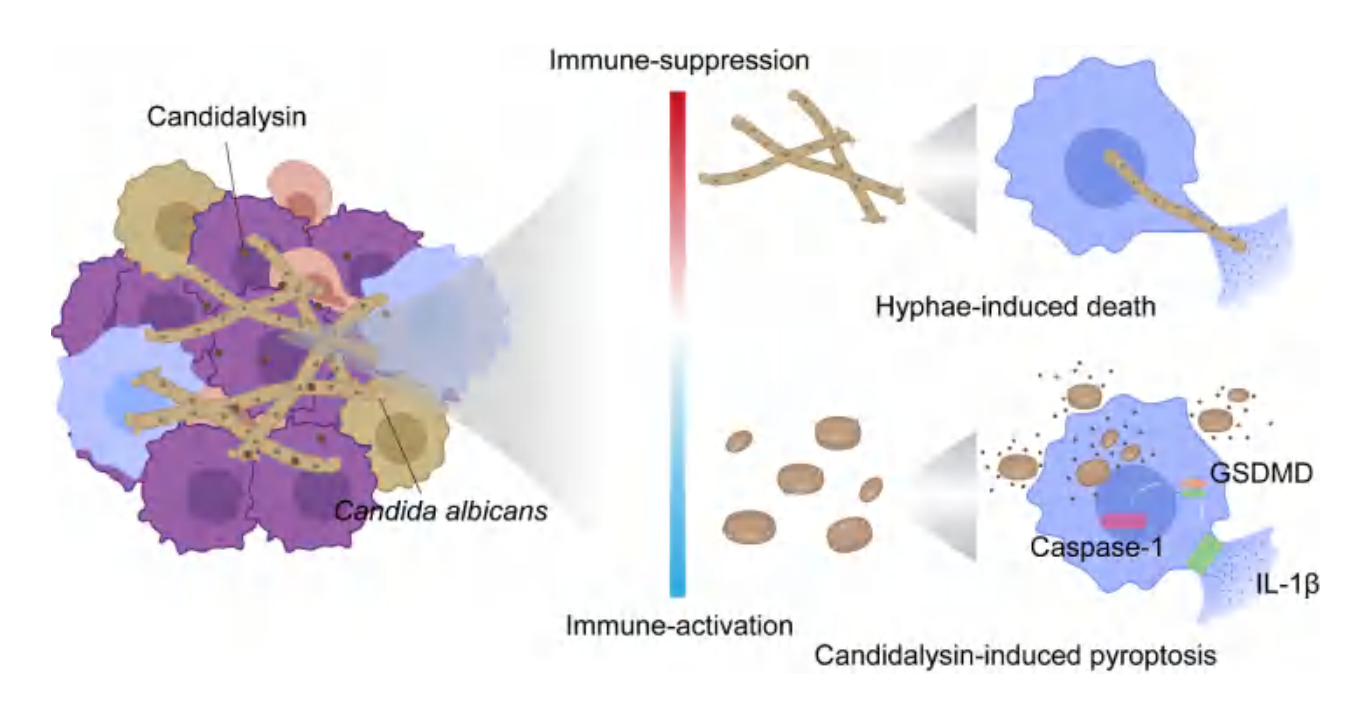


Figure S8. Schematic diagram of the distinct pathways of macrophage cell death induced by different morphological states of *C. albicans*.



Figure S9. a-b, The phage outputs from the three rounds of biopanning. Quantitative analysis (a) and bright field images (b) of phage outputs from each round of biopanning.

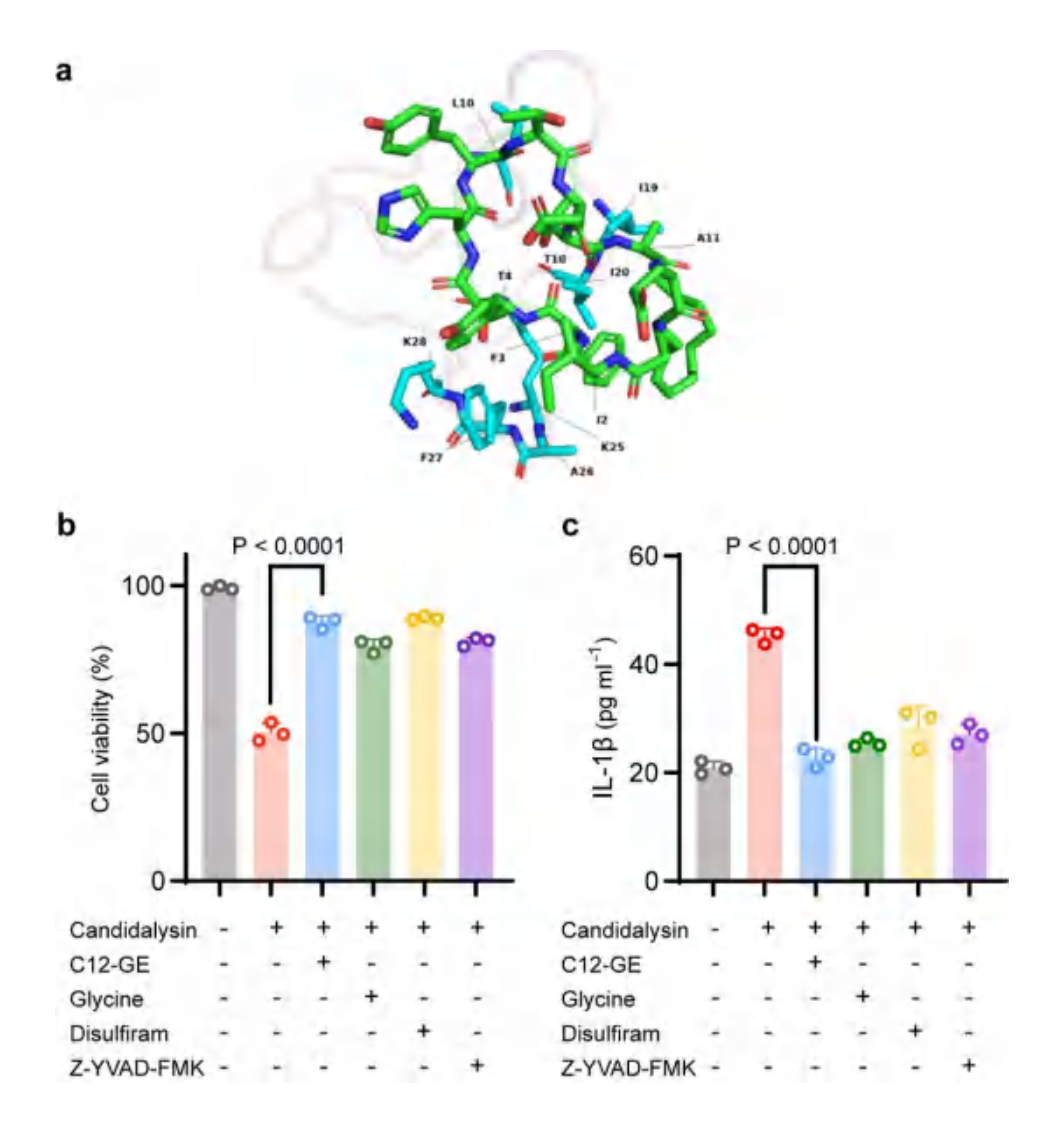


Figure S10. Neutralization of candidalysin by C12-GE prevents macrophage pyroptosis. a, The model of C12-GE (blue-green) binding to candidalysin (light purple) protein. b, Quantitative analysis of C12-GE in inhibiting candidalysin-induced BMDM pyroptosis. n=3 independent samples. c, Quantitative analysis of IL-1 β secretion by BMDMs following C12-GE peptide-mediated inhibition of candidalysin-induced pyroptosis. n=3 independent samples.

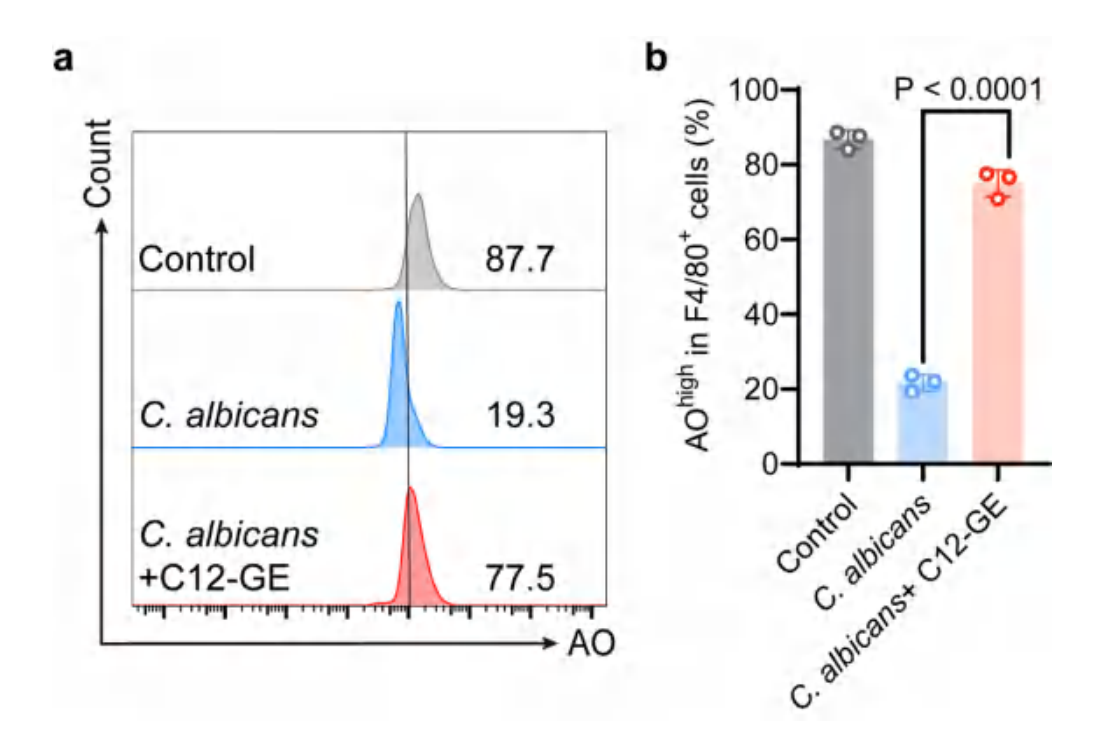


Figure S11. AO staining in BMDMs after different treatment. a-b, Representative FCM images of AO intensity inside BMDMs after different treatments (a) and quantitative statistical analysis (b). n = 3 independent samples. Data are presented as mean \pm s.d. Statistical significance was determined by one-way ANOVA with Tukey's post hoc correction (b).

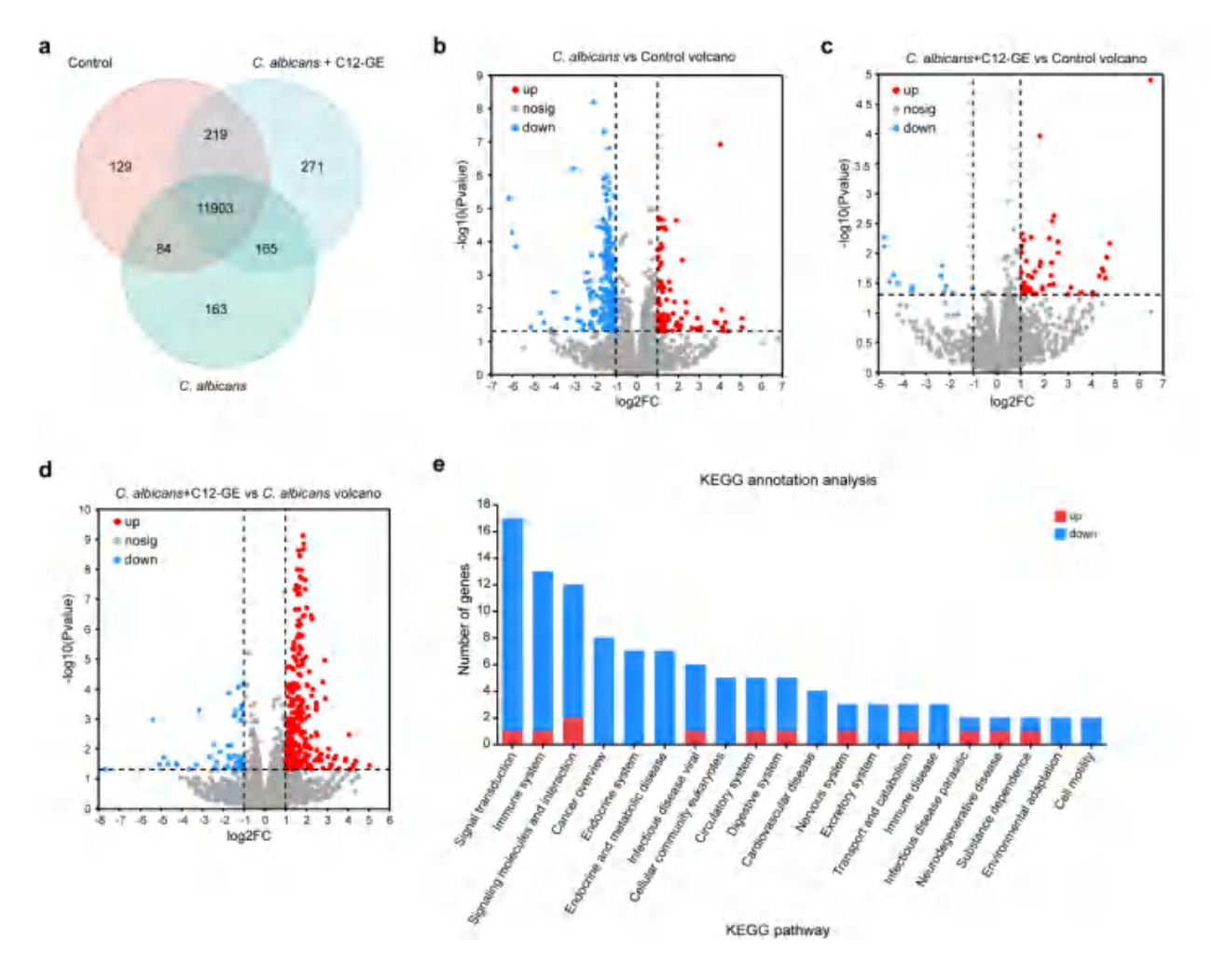


Figure S12. a, Venn diagram of BMDM cell transcription after different treatments. b, Volcano plot of differentially expressed genes between the *C. albicans* treatment group and the control group (p value < 0.05 and fold change \geq 2). c, Volcano plot of differentially expressed genes between the *C. albicans* + C12-GE treatment group and the control group (p value < 0.05 and fold change \geq 2). d, Volcano plot of differentially expressed genes between the *C. albicans* + C12-GE treatment group and the *C. albicans* treatment group (p value < 0.05 and fold change \geq 2). e, KEGG pathway annotation analysis of differentially expressed genes between the *C. albicans* + C12-GE treatment group and the *C. albicans* treatment group.

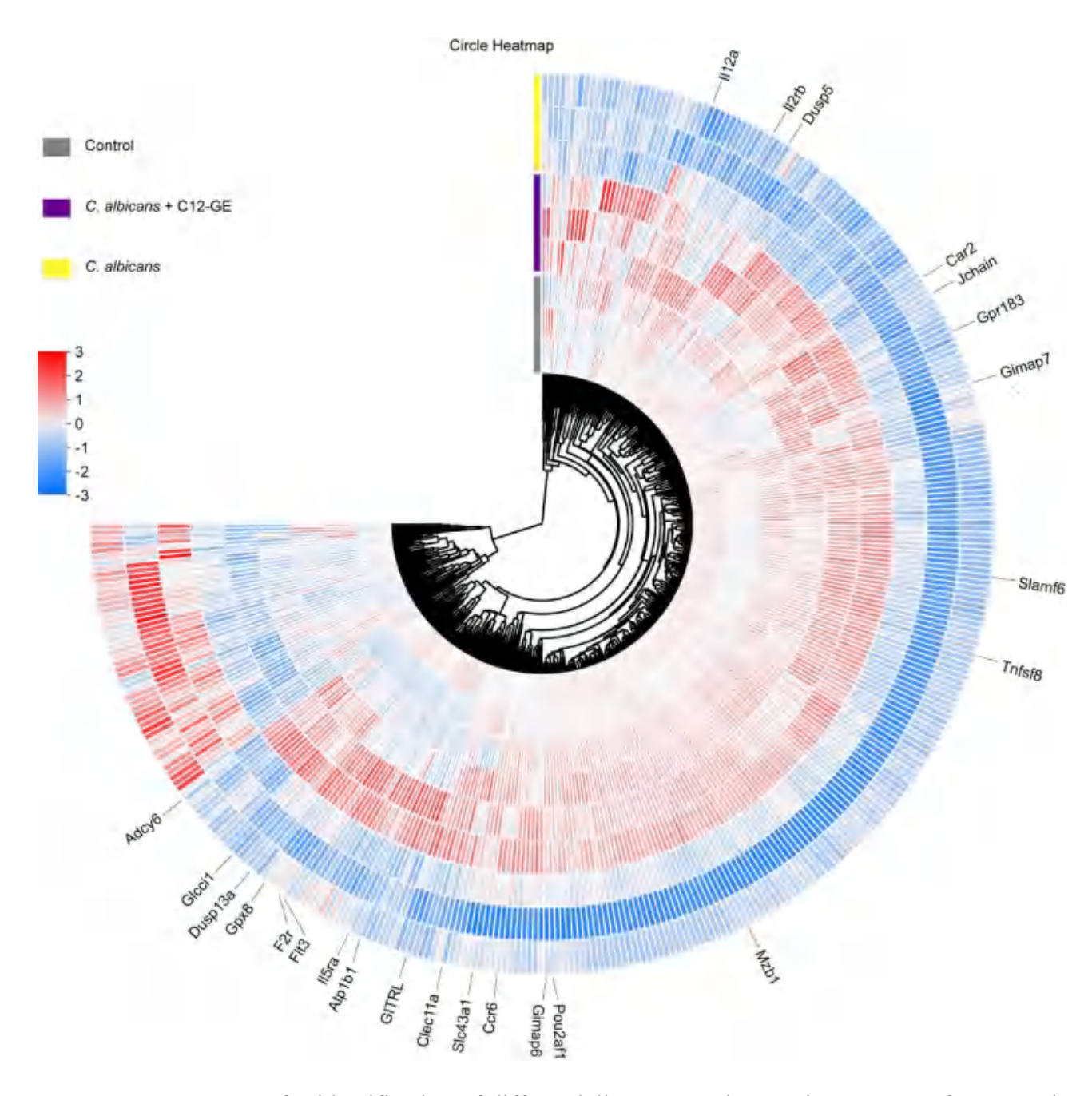


Figure S13. Heat map for identification of differentially expressed genes in BMDMs after control, *C. albicans* and *C. albicans*+C12-GE treatment. Three biological replicates are shown for each group.

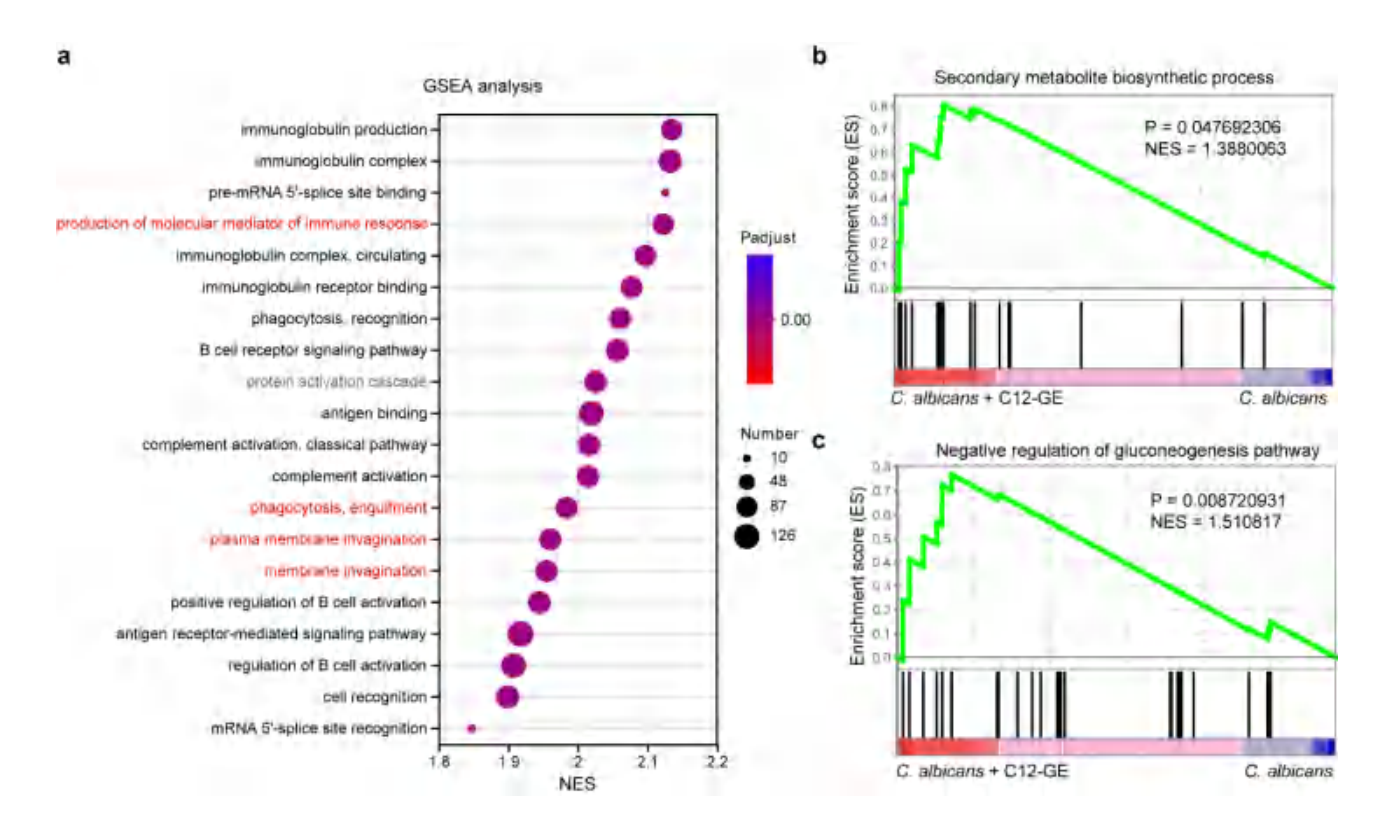


Figure S14. a, GSEA enrichment analysis comparing the pathways associated with differentially expressed genes between the *C. albicans* + C12-GE treatment group and the *C. albicans* treatment group. b, GSEA enrichment analysis comparing the secondary metabolite biosynthetic process of differentially expressed genes in BMDMs after *C. albicans* treatment and *C. albicans* + C12-GE treatment. c, GSEA enrichment analysis comparing the negative regulation of the gluconeogenesis pathway of differentially expressed genes in BMDMs after *C. albicans* treatment and *C. albicans* + C12-GE treatment.

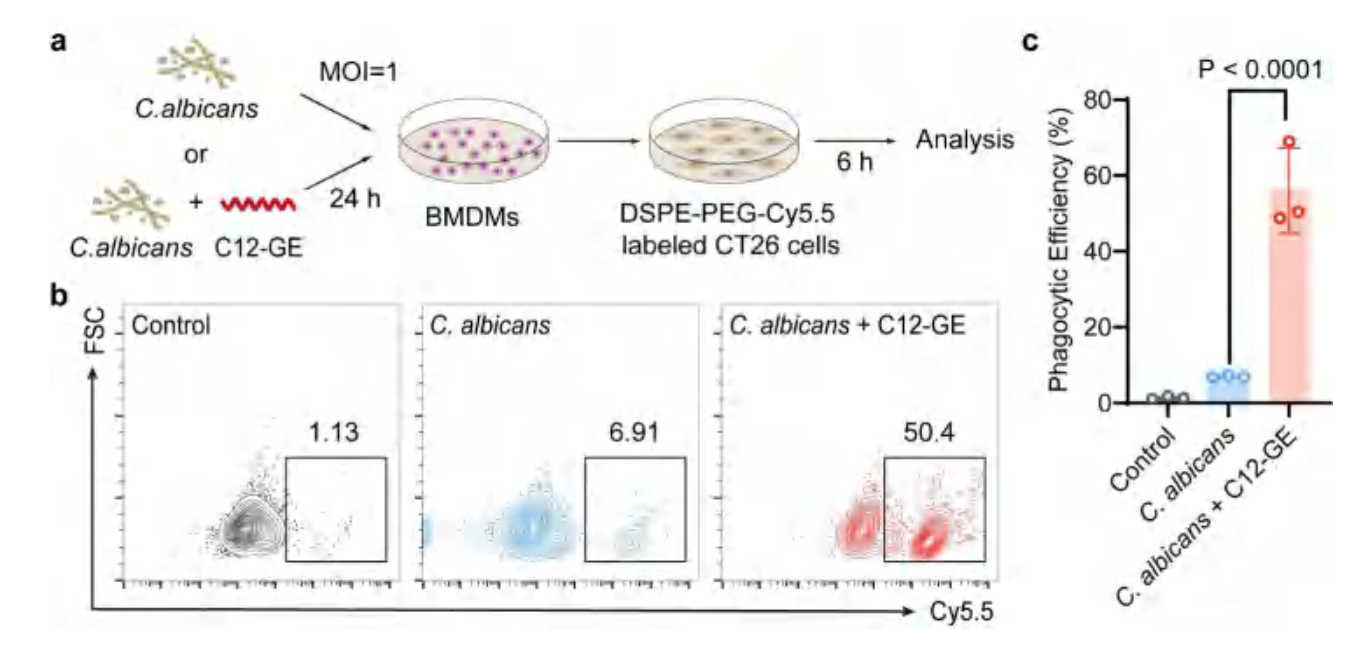


Figure S15. BMDM phagocytosis of tumor cells after different treatment. a, Schematic diagram of the phagocytosis assays with tumor target cells. b-c, Representative FCM images of phagocytic efficiency of BMDMs after different treatments (b) and quantitative statistical analysis (c). n = 3 independent samples. Data are presented as mean \pm s.d. Statistical significance was determined by one-way ANOVA with Tukey's post hoc correction (c).

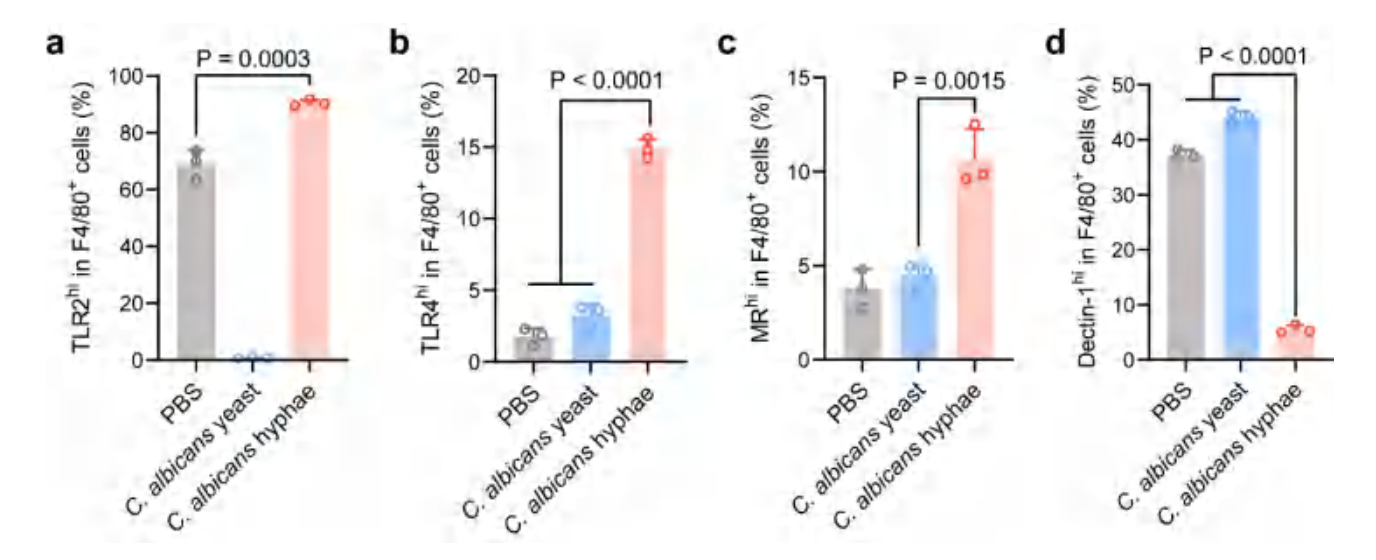


Figure S16. Quantitative analysis of the expression levels of TLR2 (a), TLR4 (b), Mannose receptor (c), and Dectin-1 (d) on the surface of macrophages treated with *C. albicans* hyphae and yeast forms respectively. n = 3 independent samples. Data are presented as mean \pm s.d. Statistical significance was determined by one-way ANOVA with Tukey's post hoc correction.

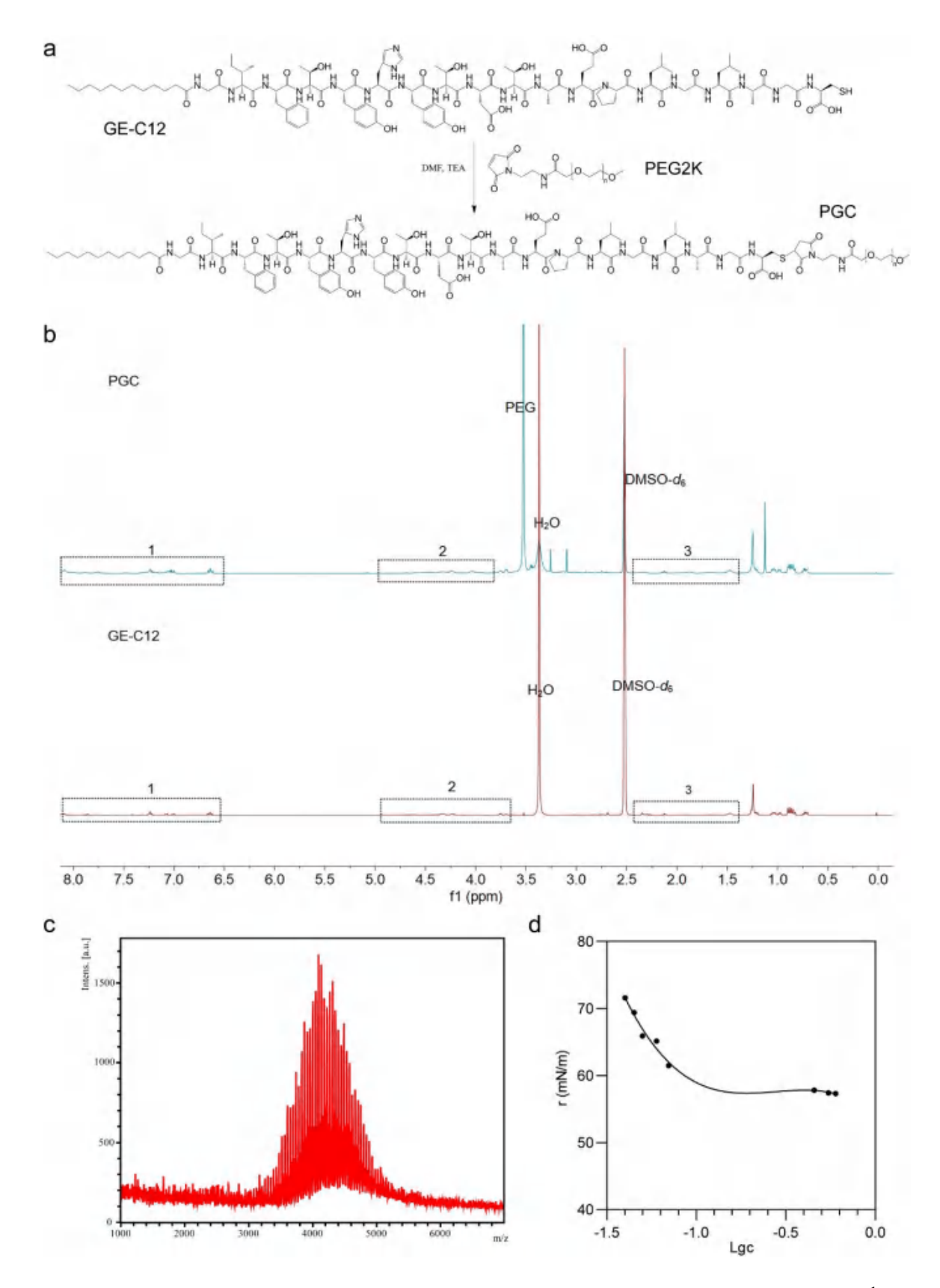


Figure S17. Synthesis and characterization of PGC. a, Synthesis of PGC polymers. b, ¹H-NMR spectrum of PGC (DMSO-d6). c, MALDI mass spectrum of PGC. d, Detection of CMC of PGC by surface tension method.

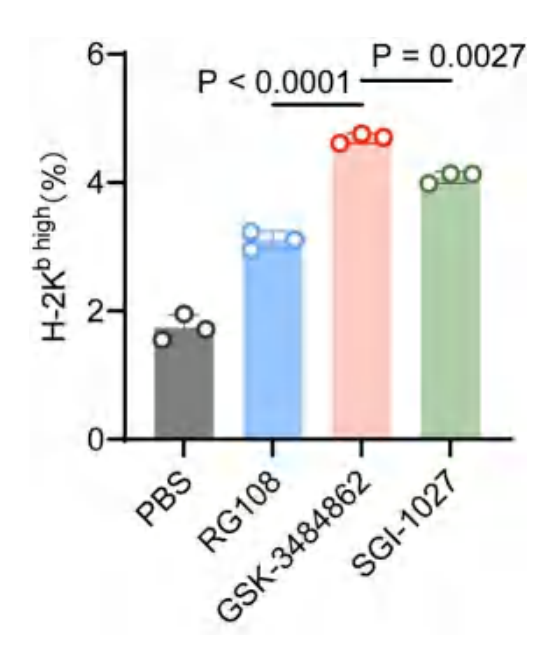


Figure S18. FCM quantitative analysis of H-2K^b expression on CT26 cells after different treatments. n = 3 independent samples. Data are presented as mean \pm s.d. Statistical significance was determined by one-way ANOVA with Tukey's post hoc correction.

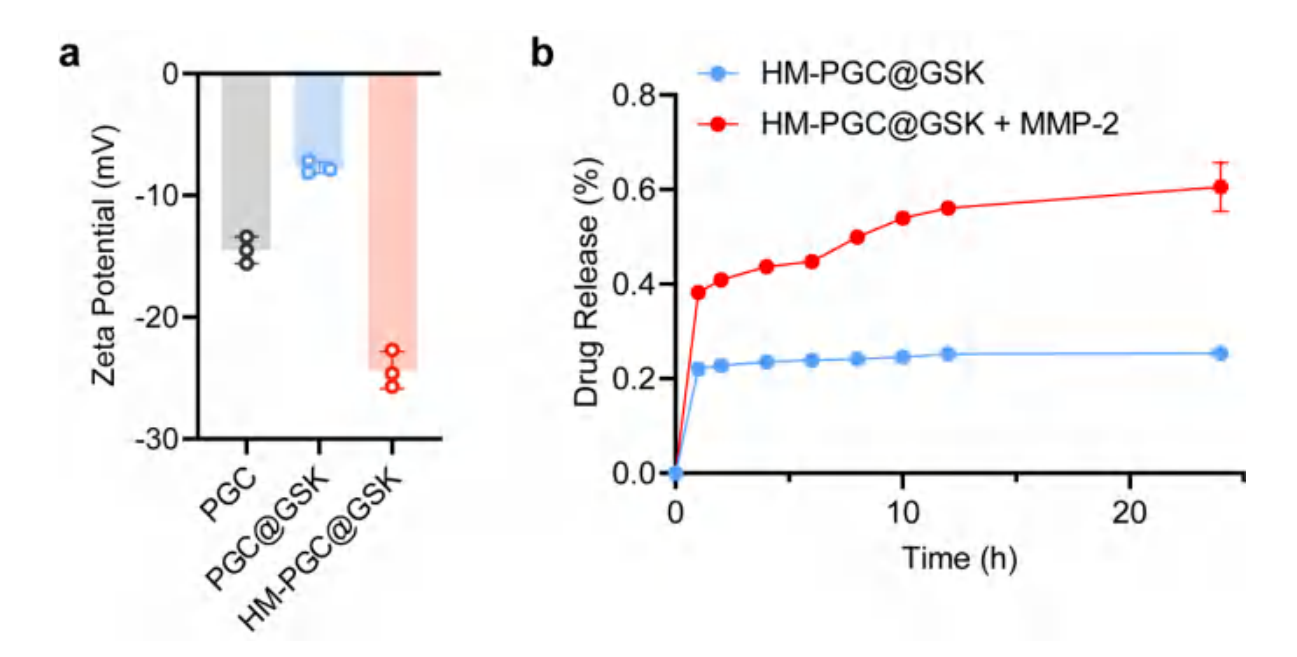


Figure S19. Synthesis and characterization of HM-PGC@GSK. a, Zeta potential of PGC, PGC@GSK, and HM-PGC@GSK. n = 3 independent samples. b, Drug release curves of HM-PGC@GSK in the presence or absence of MMP-2. n = 3 independent samples. Data are presented as mean \pm s.d. Statistical significance was determined by one-way ANOVA with Tukey's post hoc correction (a) and unpaired two-tailed Student's t-test (b).

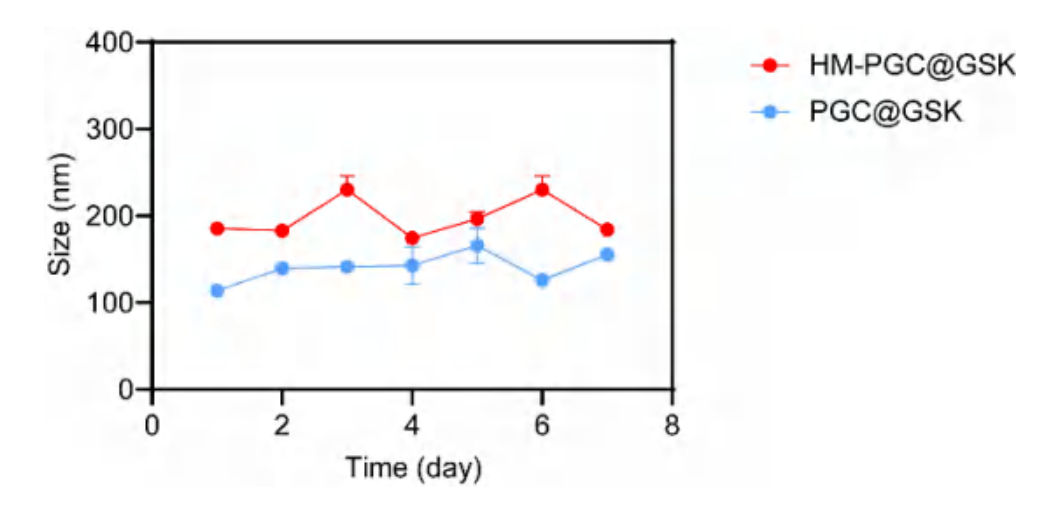


Figure S20. The stability of HM-PGC@GSK and PGC@GSK in serum-containing culture medium.

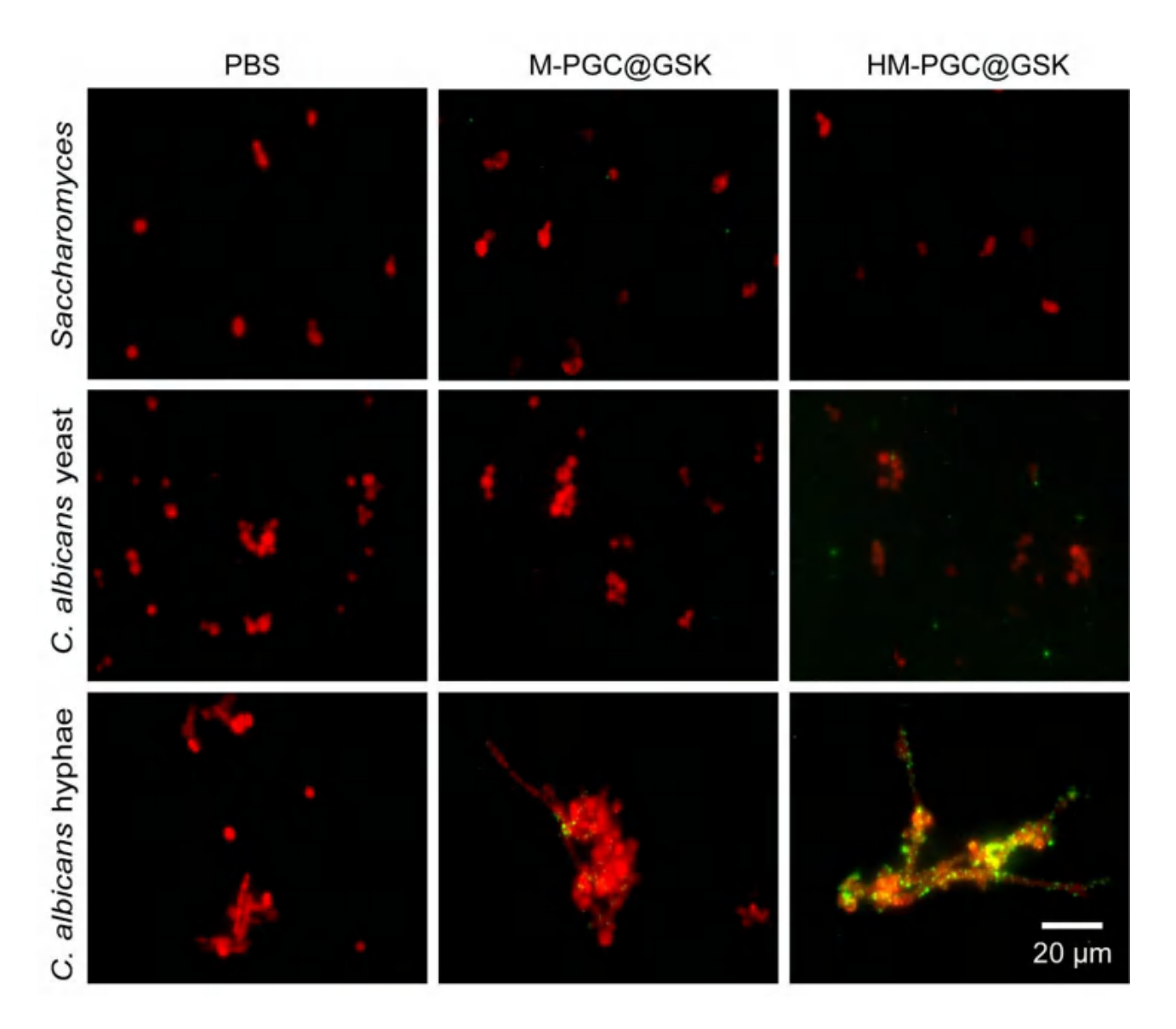


Figure S21. Representative CLSM images of DIO-labeled M-PGC@GSK and HM-PGC@GSK after co-incubation with Cy5.5-labeled *Saccharomyces*, *C. albicans* yeast, and *C. albicans* hyphae, respectively.

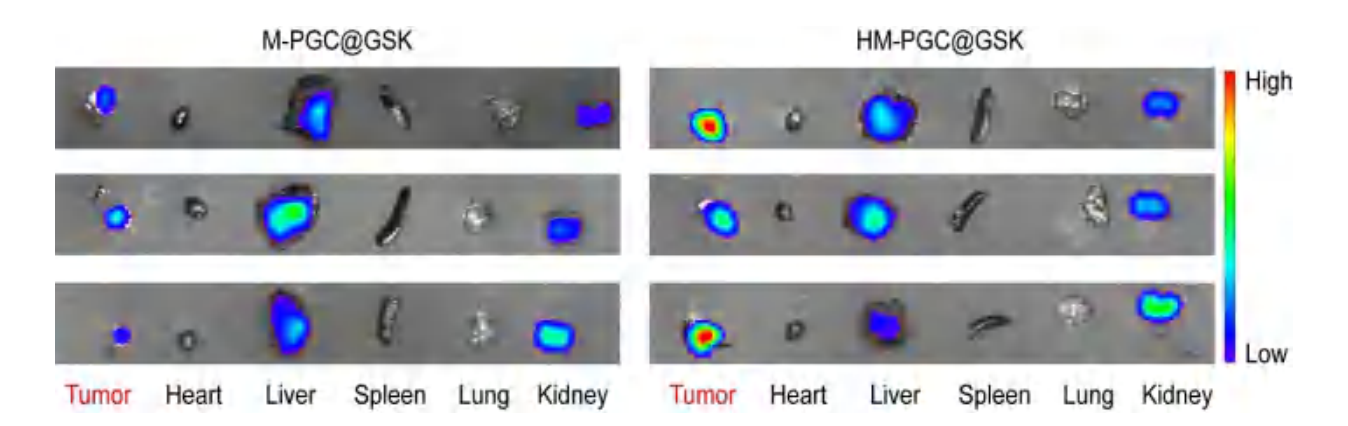


Figure S22. The fluorescence images of all samples in Figure 4n.

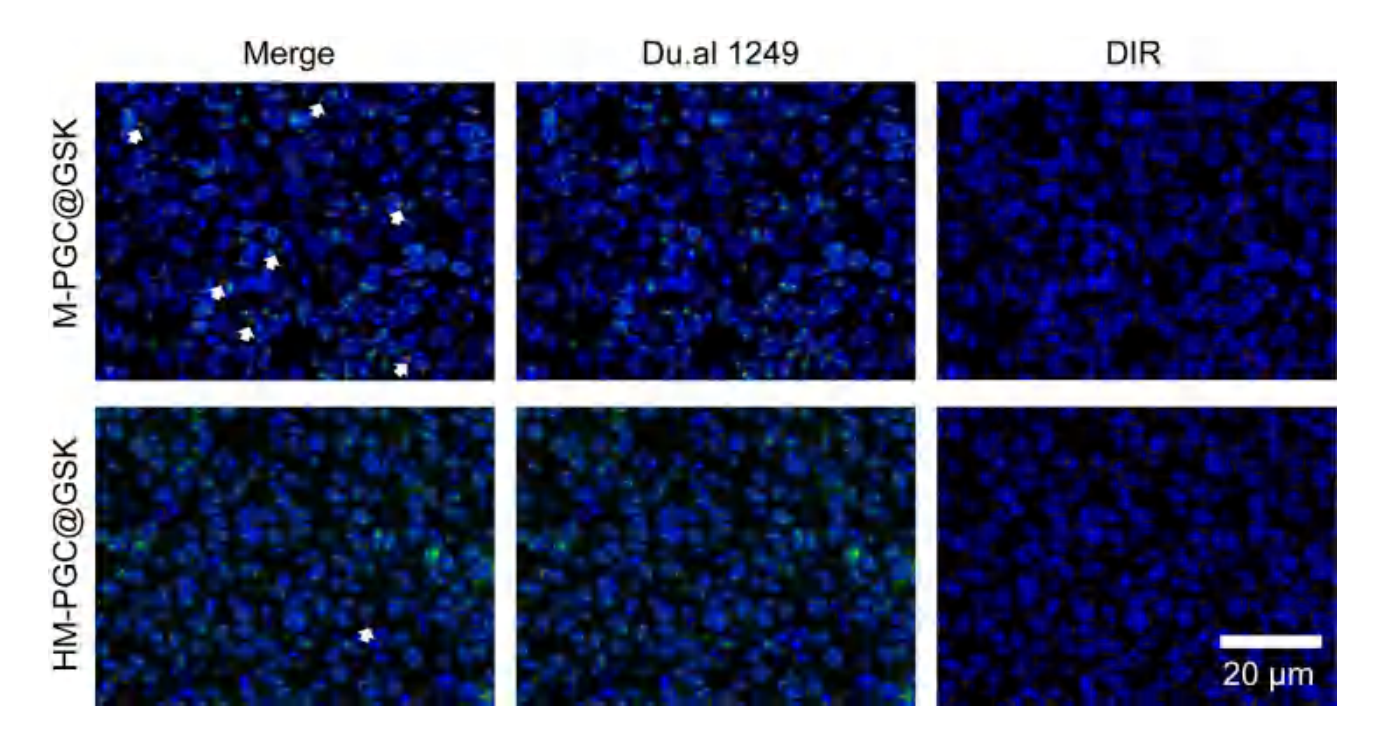


Figure S23. Representative CLSM of the co-localization of nanoparticles and *C. albicans* within the tumor of subcutaneous tumor-bearing mice at, 24 hours after intravenous injection of M-PGC@GSK or HM-PGC@GSK.

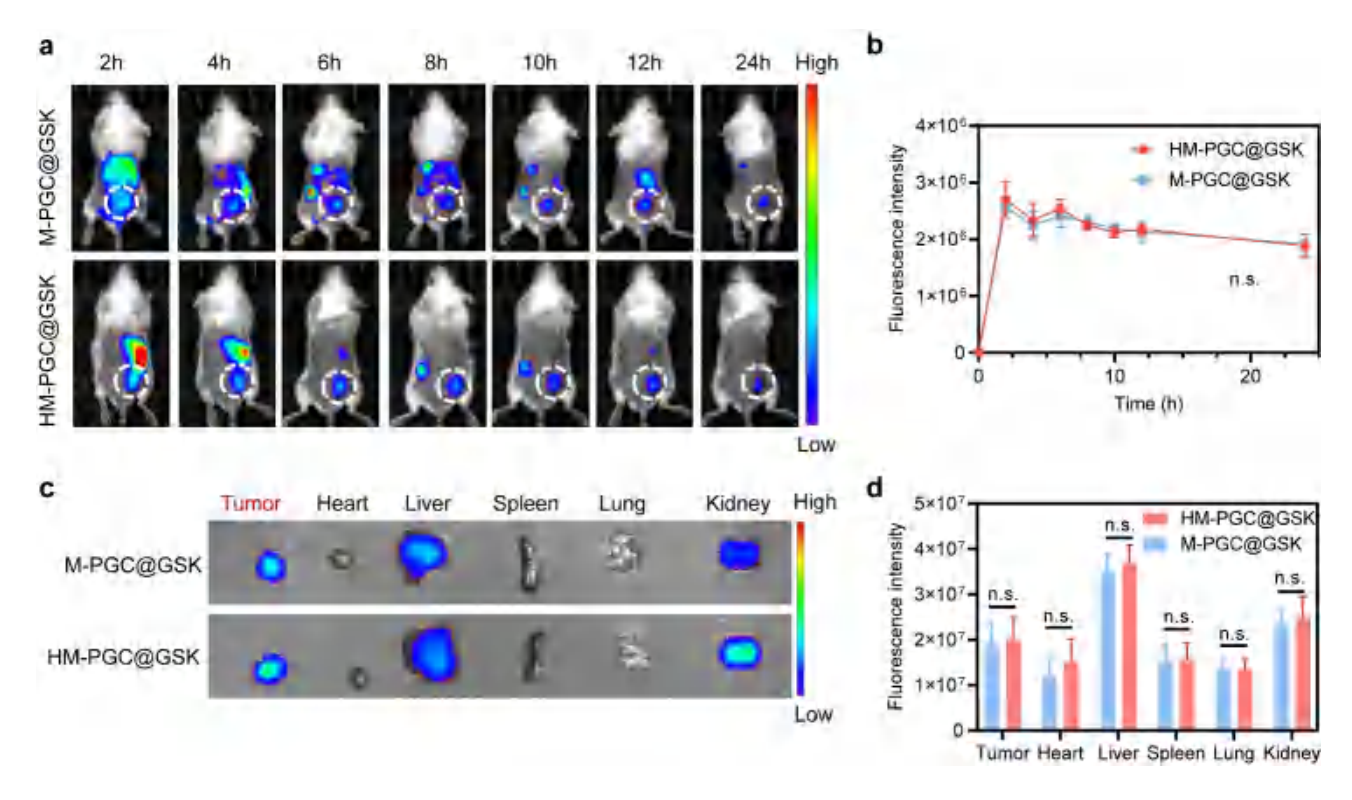


Figure S24. Targeting capacity of HM-PGC@GSK and M-PGC@GSK in tumor-bearing mice without *C. albicans* load. a, Representative IVIS images of BALB/c mice bearing subcutaneous CRC tumors without *C. albicans* treatment within 24 h after intravenous administration of DIR-labeled M-PGC@GSK or HM-PGC@GSK. b, Quantification of in situ tumor fluorescence over 24 h after intravenous administration of DIR-labeled M-PGC@GSK or HM-PGC@GSK in BALB/c mice bearing subcutaneous CRC tumors without *C. albicans* treatment. n = 3 independent samples. c, Representative IVIS images of tumors and various organs of BALB/c mice bearing subcutaneous CRC tumors without *C. albicans* treatment within 24 h after intravenous administration of DIR-labeled M-PGC@GSK or HM-PGC@GSK. d, Quantitative analysis of fluorescence intensity of tumors and various organs 24 hours after intravenous administration of DIR-labeled M-PGC@GSK or HM-PGC@GSK in subcutaneous CRC BALB/c mice without *C. albicans* treatment. n = 3 independent samples. Data are presented as mean ± s.d. Statistical significance was determined by unpaired two-tailed Student's t-test (b, d).

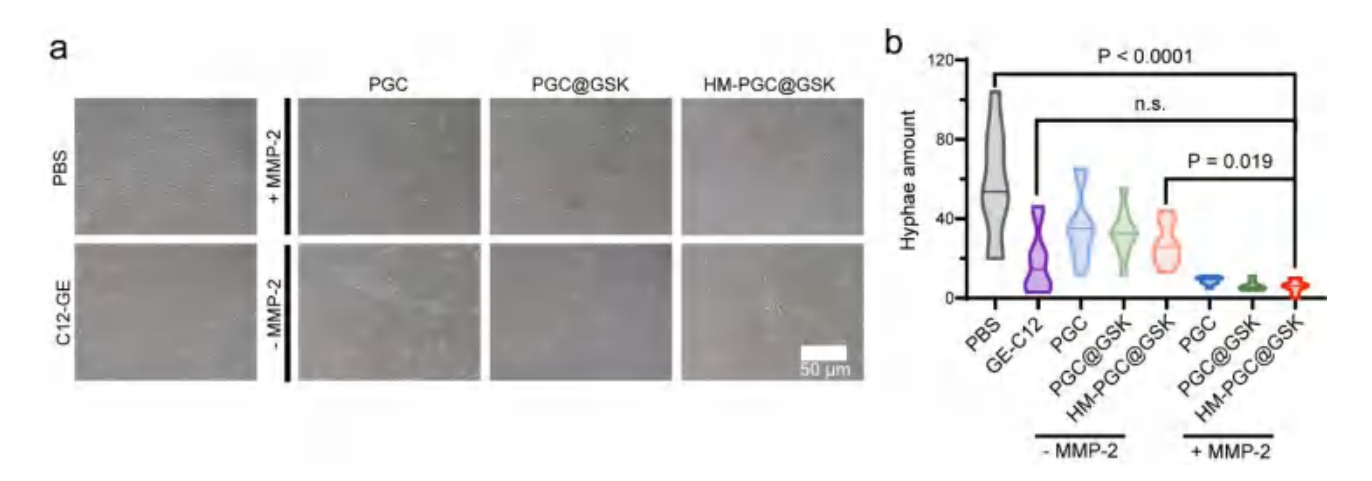


Figure S25. HM-PGC@GSK induces morphological transformation of C. albicans. a-b, Bright field images (a) and quantitative analysis (b) of C. albicans yeast form induced by PGC, PGC@GSK, and HM-PGC@GSK in the presence or absence of MMP-2 enzyme. Data are presented as mean \pm s.d. Statistical significance was determined by one-way ANOVA with Tukey's post hoc correction (b).

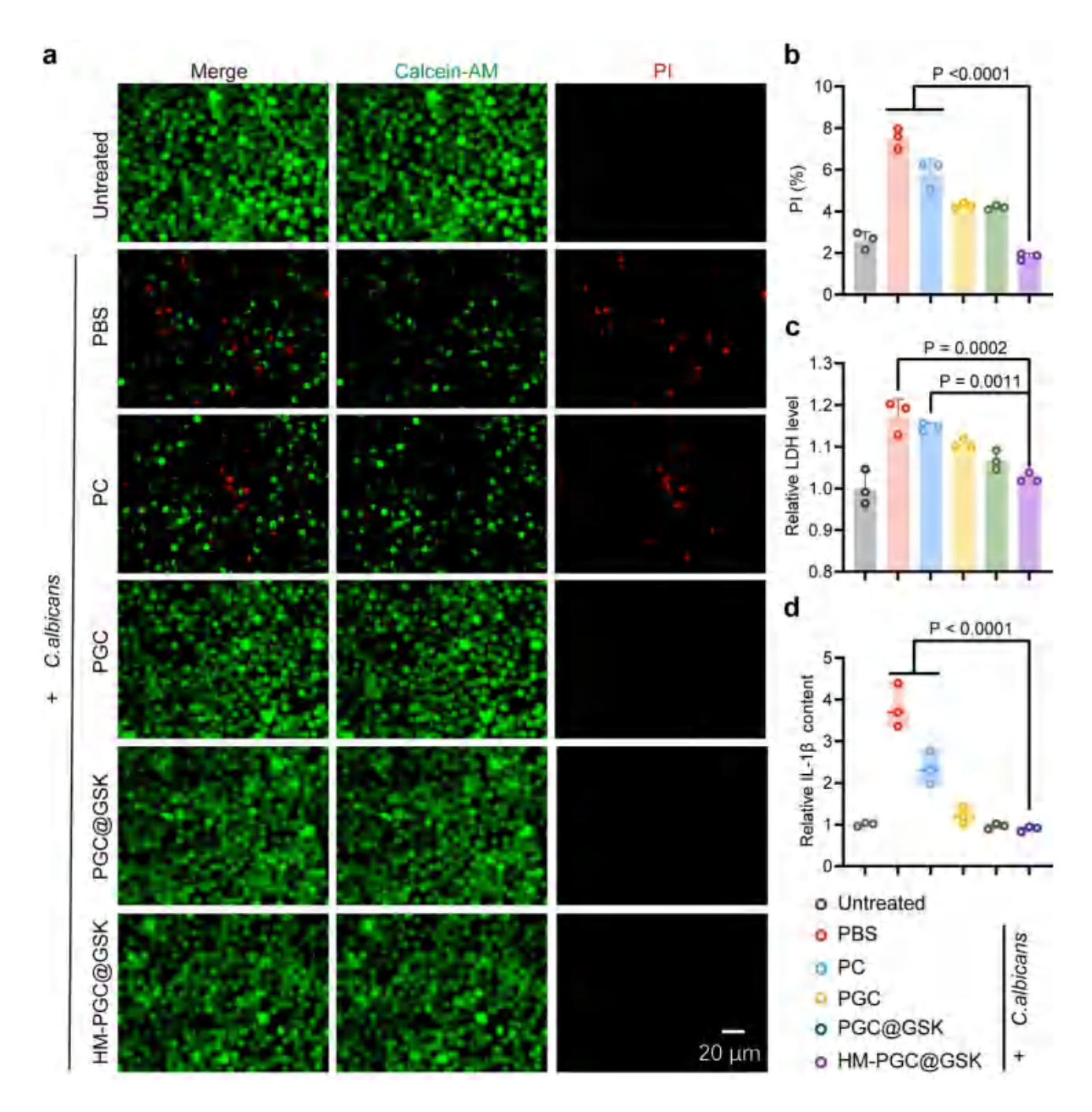


Figure S26. HM-PGC@GSK protects J774A.1 from pyroptosis. a, Representative CLSM images of Calcein/PI staining of J774A.1 cells following various treatments. b, Quantitative analysis of PI staining of J774A.1 cells following various treatments by FCM. n=3 independent samples. c, Quantitative analysis of LDH secretion by J774A.1 cells after different treatments. n=3 independent samples. d, Quantitative analysis of IL-1β secretion by J774A.1 cells after different treatments. n=3 independent samples. Data are presented as mean \pm s.d. Statistical significance was determined by one-way ANOVA with Tukey's post hoc correction (b, c, d).

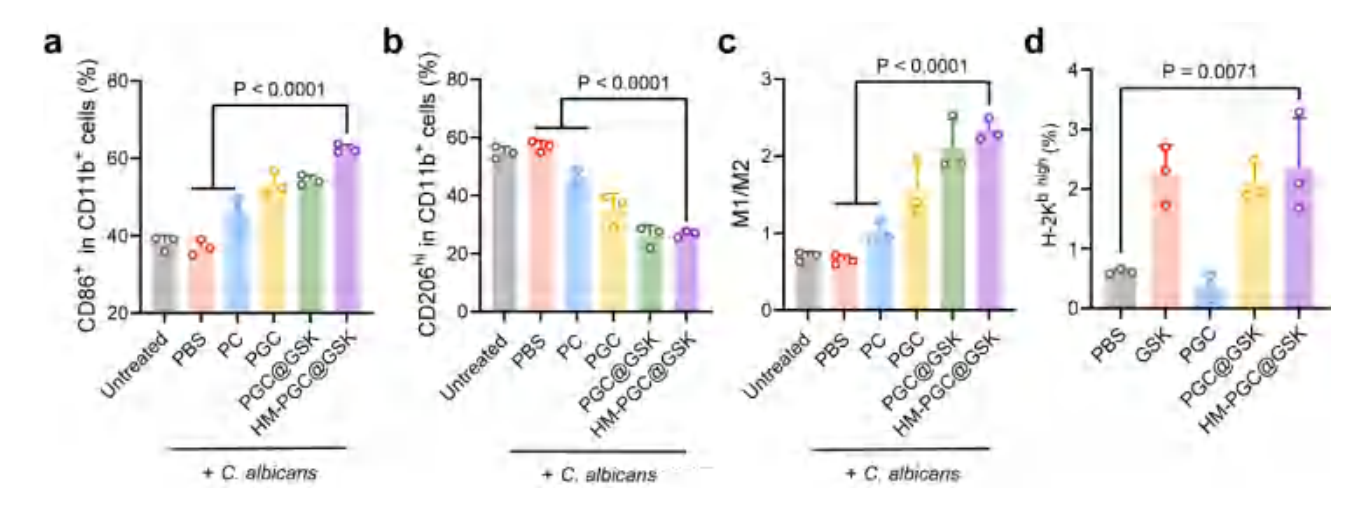


Figure S27. HM-PGC@GSK induces M1 polarization of BMDMs and a-c, Flow cytometry analysis of M1 macrophages (a), M2 macrophages (b) and M1/M2 ratio (c) in BMDM cells after different treatments. n = 3 independent samples. d, FCM quantitative analysis of H-2K^b expression on CT26 cells after different treatments. n = 3 independent samples. Data are presented as mean \pm s.d. Statistical significance was determined by one-way ANOVA with Tukey's post hoc correction.

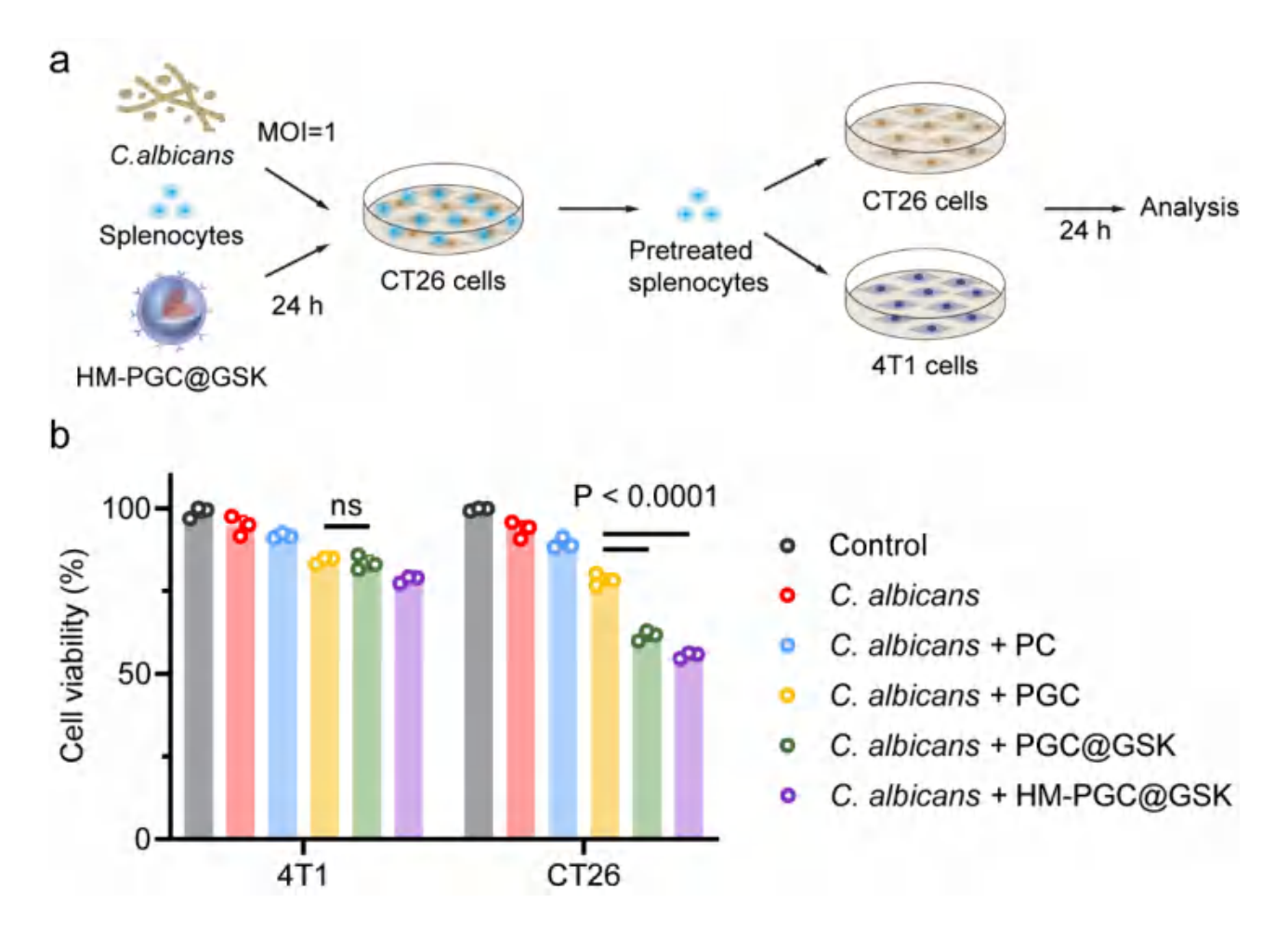


Figure S28. a, The Schematic diagram of splenocyte killing specificity detection. b, Cell viability of CT26 and 4T1 cells following co-culture with different pretreatments of splenocyte. n=3 independent samples. Data are presented as mean \pm s.d. Statistical significance was determined by one-way ANOVA with Tukey's post hoc correction.

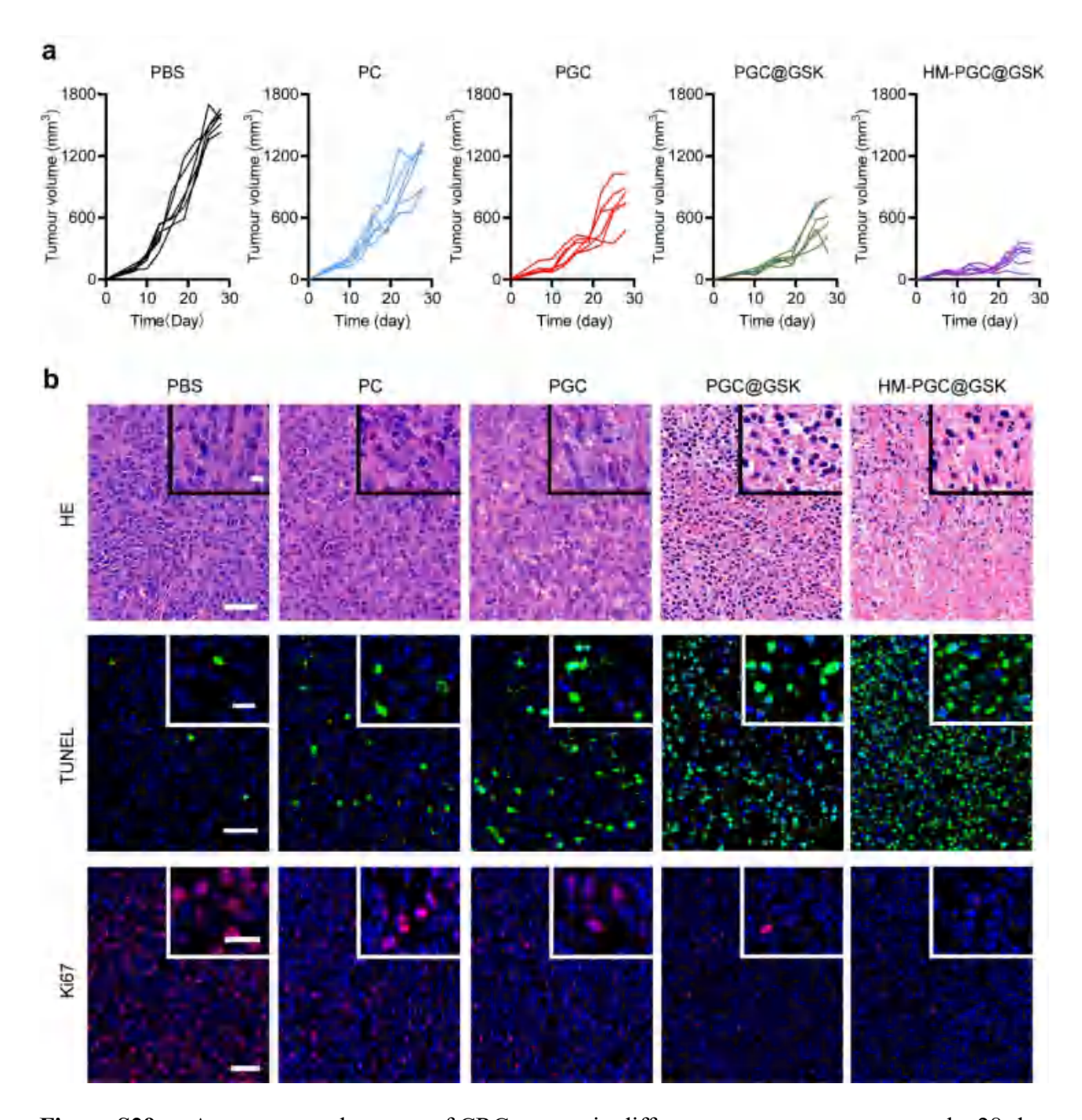


Figure S29. a, Average growth curves of CRC tumors in different treatment groups over the 28-day of the treatment period. n=6 independent mice. b, H&E staining, TUNEL staining, and Ki67 staining of tumor tissues from mice in different treatment groups. Scale bar, 50 μ m (inset, 20 μ m).

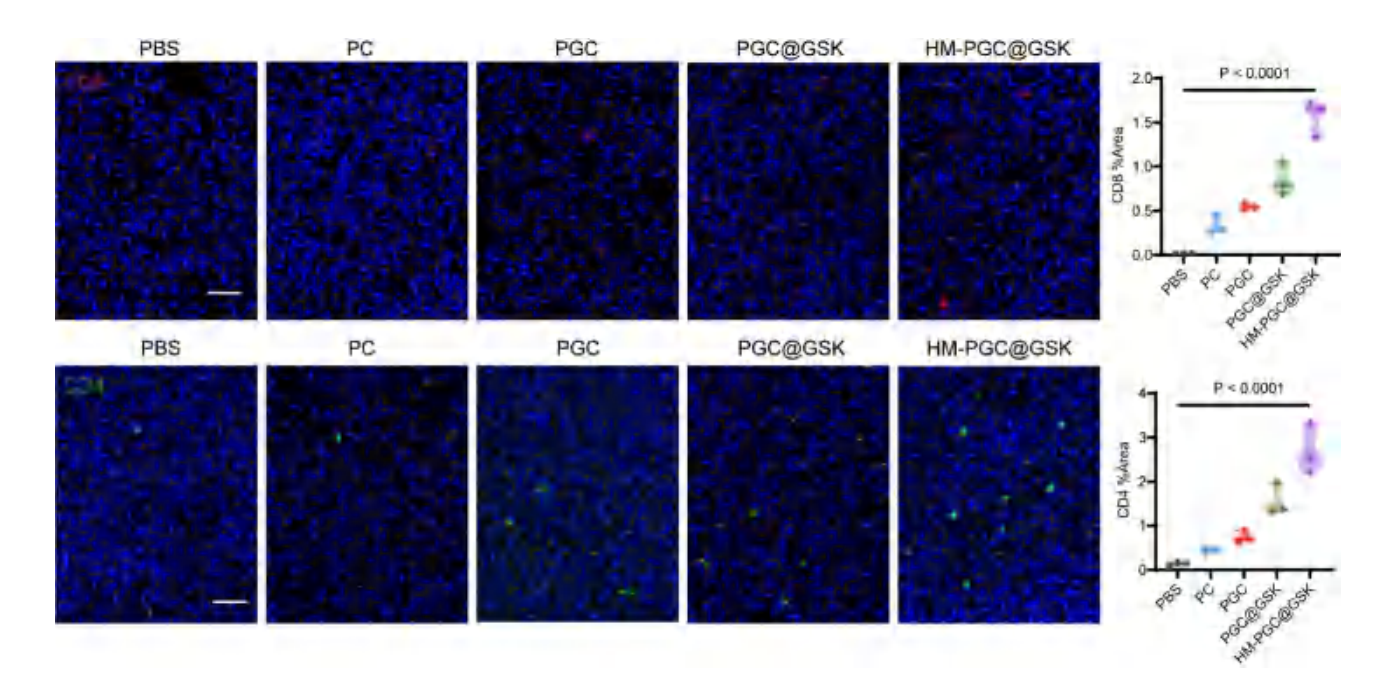


Figure S30. Representative immunofluorescence staining CLSM images and quantitative analysis of CD8⁺ and CD4⁺ of tumor tissues from mice in different treatment groups. Scale bar, 50 μ m. n = 3 independent samples. Data are presented as mean \pm s.d. Statistical significance was determined by one-way ANOVA with Tukey's post hoc correction.

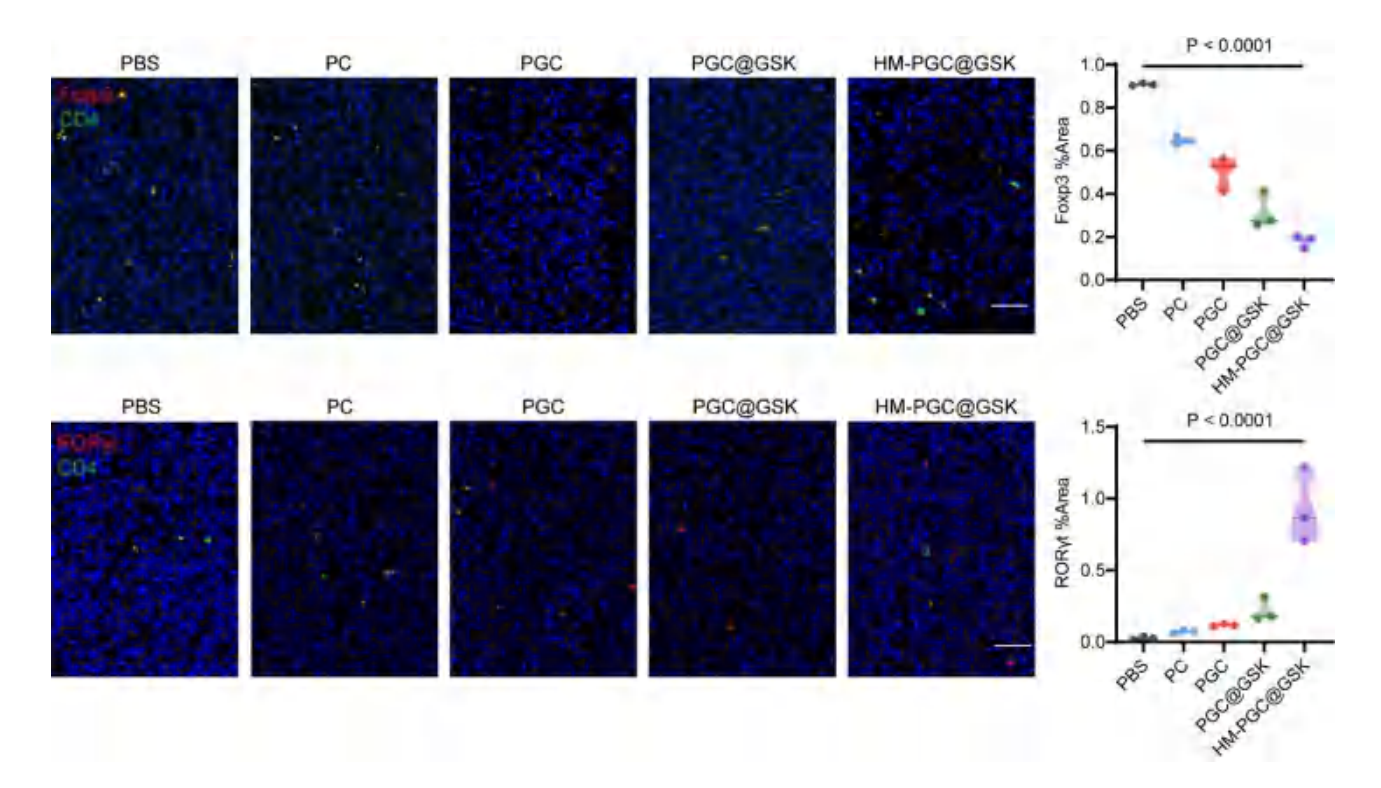


Figure S31. Representative immunofluorescence staining CLSM images and quantitative analysis of Treg (Foxp3⁺ CD4⁺) and Th17 (ROR γ t⁺ CD4⁺) of subcutaneous tumor tissues from mice in different treatment groups. Scale bar, 50 μ m. n = 3 independent samples. Data are presented as mean \pm s.d. Statistical significance was determined by one-way ANOVA with Tukey's post hoc correction.

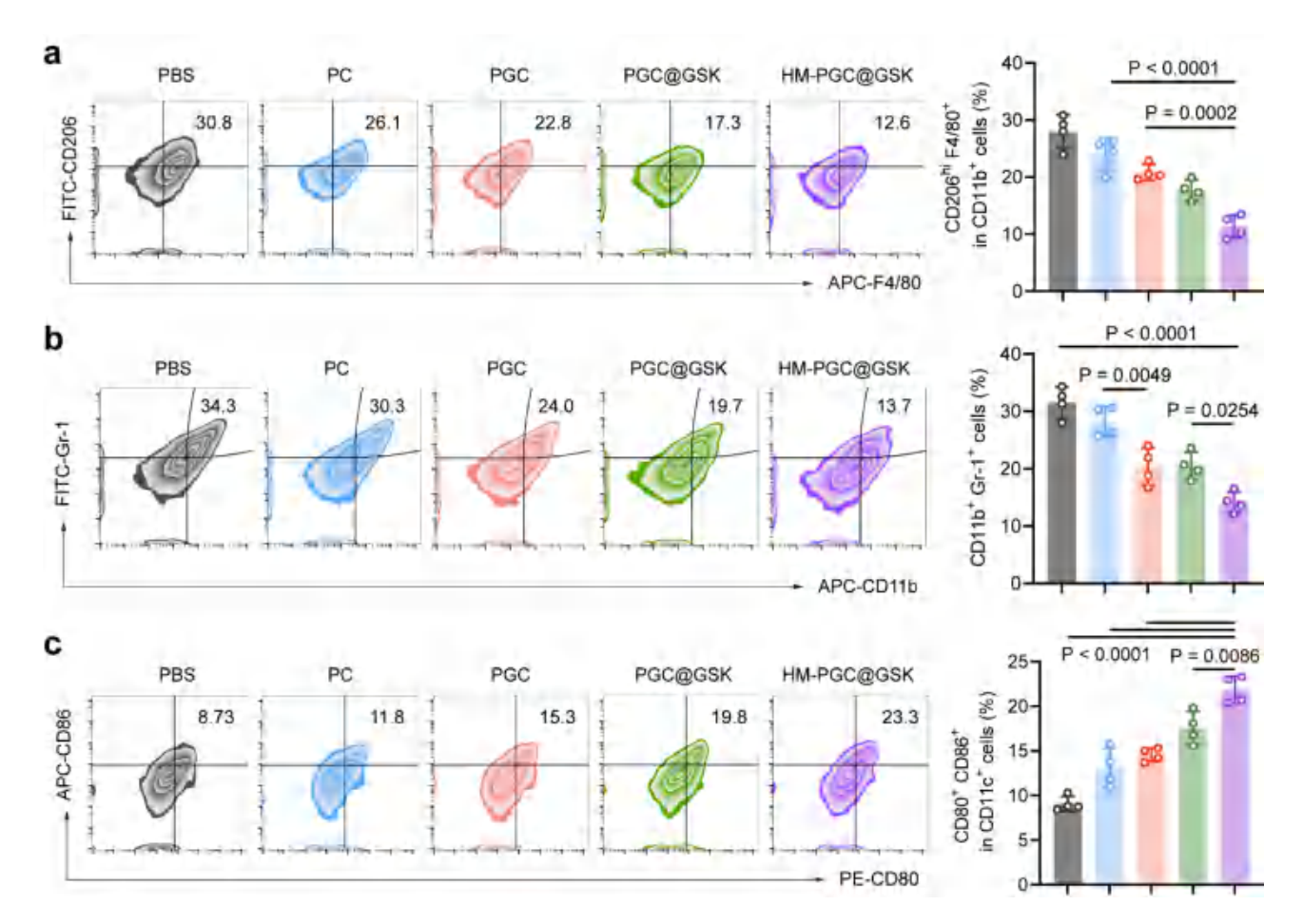


Figure S32. Representative FCM images and quantitative analysis of M2 macrophages (CD206⁺ in CD11b⁺ F4/80⁺ cells) (a), MDSCs (CD11b⁺ Gr-1⁺ cells) (b) and mature DCs (CD80⁺CD86⁺ in CD11c⁺) (c) in tumor tissues of mice bearing CT26 subcutaneous tumors in different treatment groups. n = 4 independent samples. Data are presented as mean \pm s.d. Statistical significance was determined by one-way ANOVA with Tukey's post hoc correction.

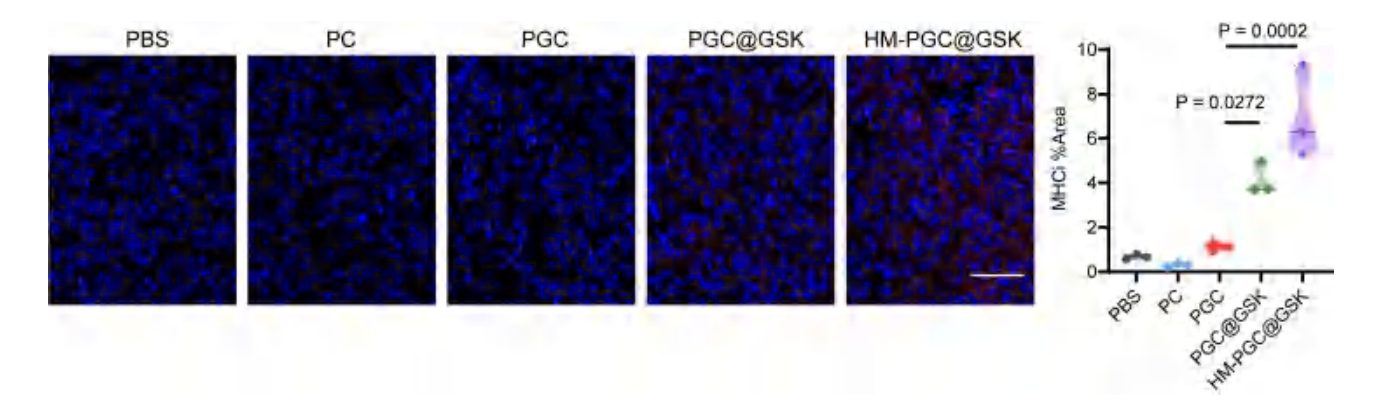


Figure S33. Representative immunofluorescence staining CLSM images and quantitative analysis of MHC I of tumor tissues from mice in different treatment groups. Scale bar, 50 μ m. n = 3 independent samples. Data are presented as mean \pm s.d. Statistical significance was determined by one-way ANOVA with Tukey's post hoc correction.

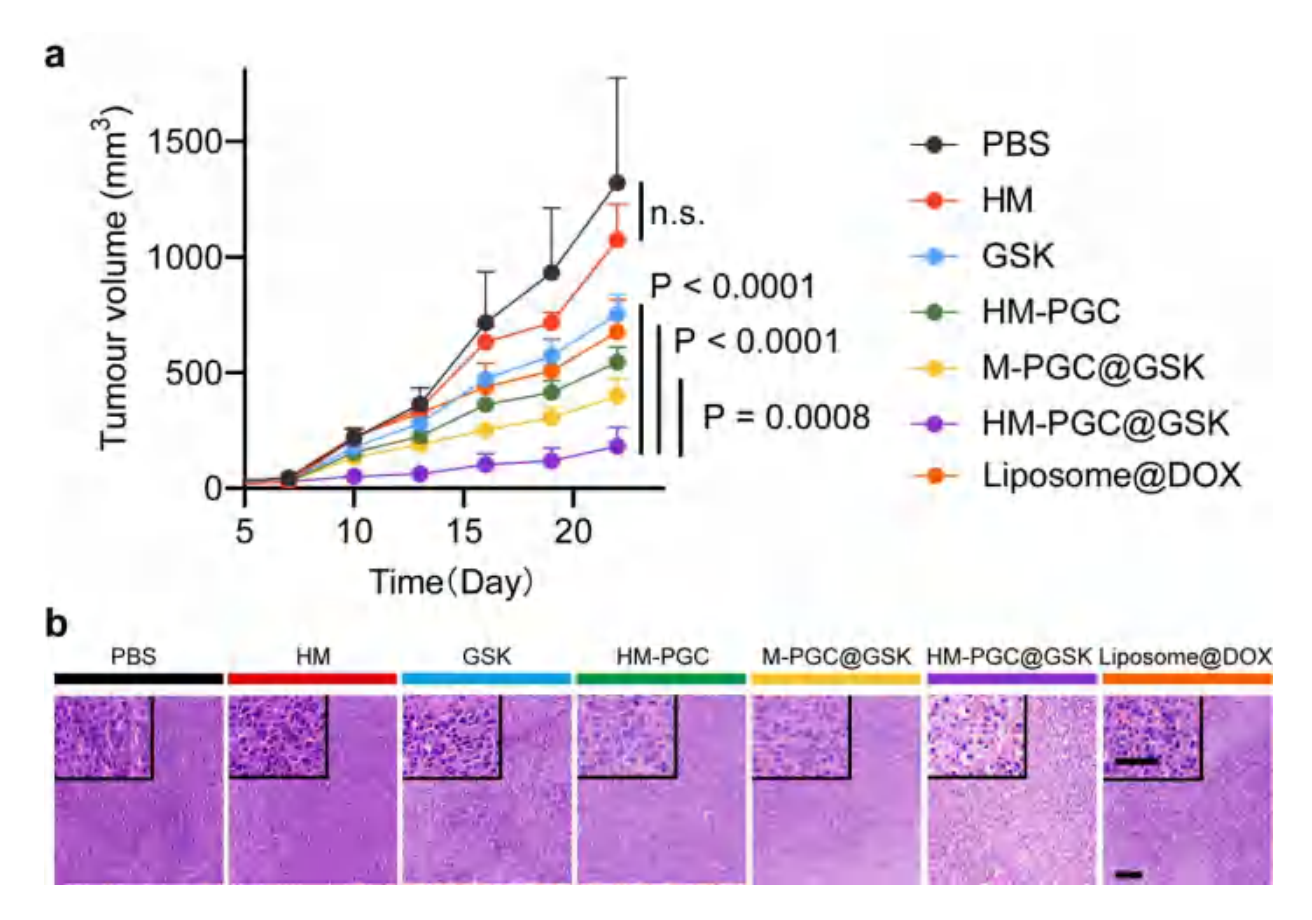


Figure S34. a, The tumor volume curves of CT26 subcutaneous tumor-bearing mice after receiving PBS, HM, GSK-3484862, HM-PGC, M-PGC@GSK, HM-PGC@GSK and liposome@DOX treatment. n = 6 independent mice. b, H&E staining of tumor tissues from mice in different treatment groups in Figure S33a. Scale bar, 100 μ m (inset, 50 μ m).

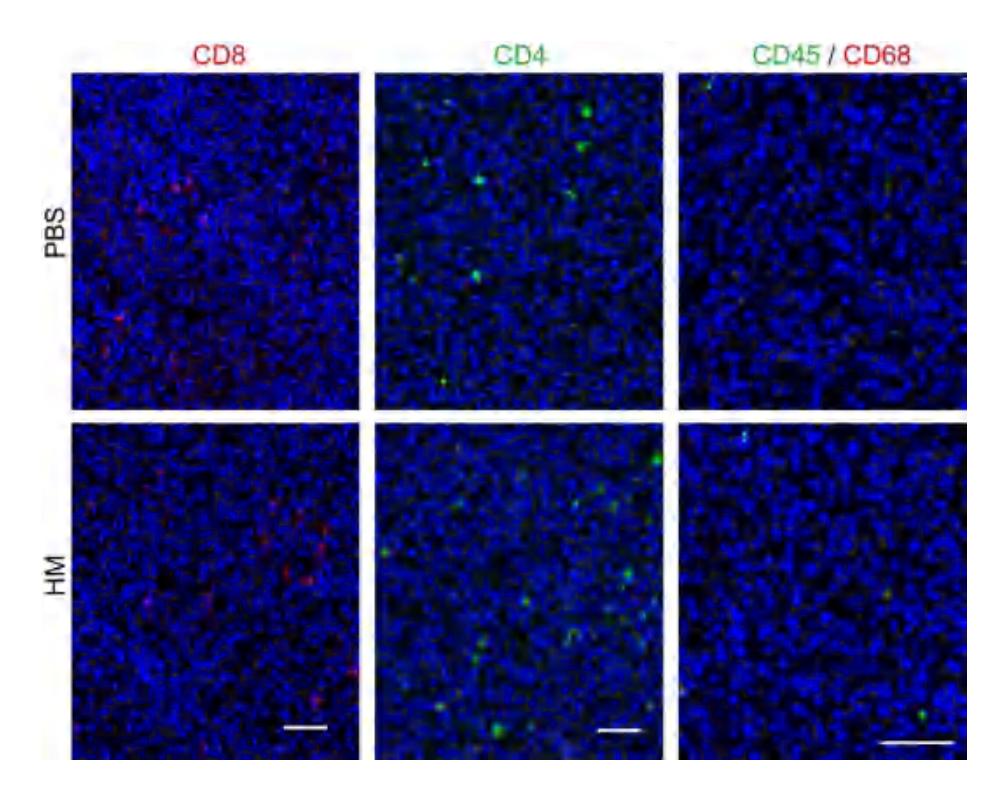


Figure S35. Representative immunofluorescence staining CLSM images of CD8, CD4 and CD45/CD68 of tumor tissues from mice treated with PBS and HM coating. Scale bar, $50 \mu m$.

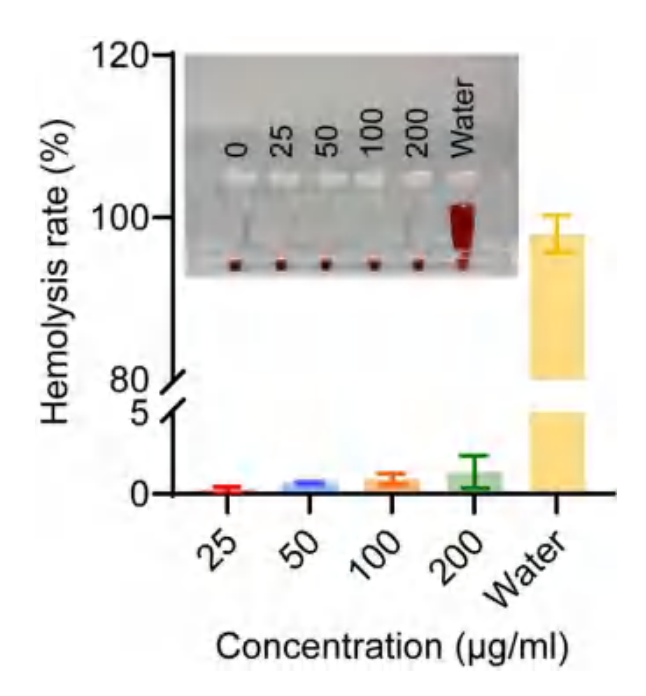


Figure S36. The hemolysis rates of mouse blood after co-incubation with HM-PGC@GSK in different concentrations. n = 4 independent sample.

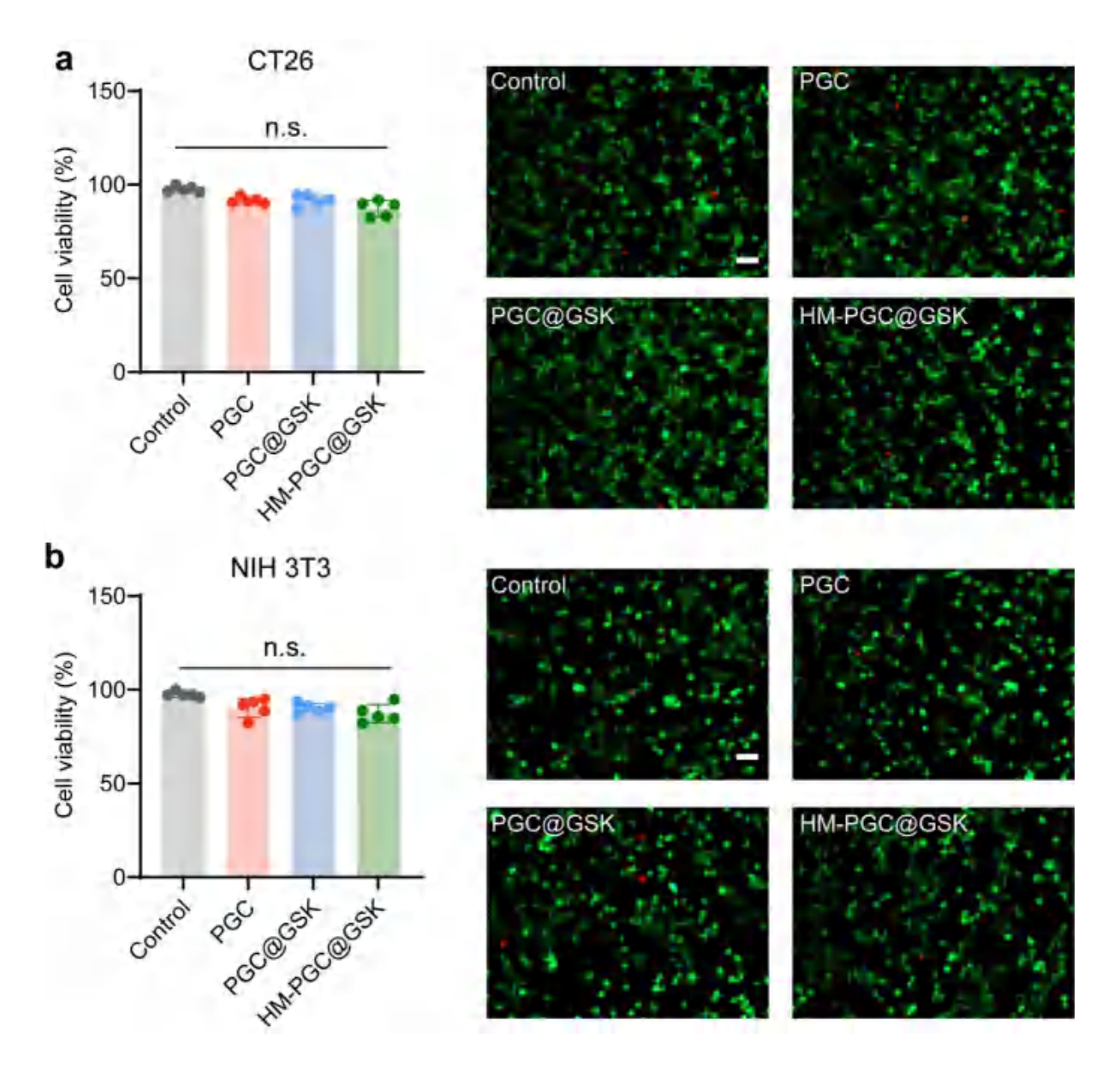


Figure S37. a-b, Cell viability and Live/dead staining of CT26 cells (a) and NIH 3T3 cells (b) after various treatments. n = 5 independent sample.

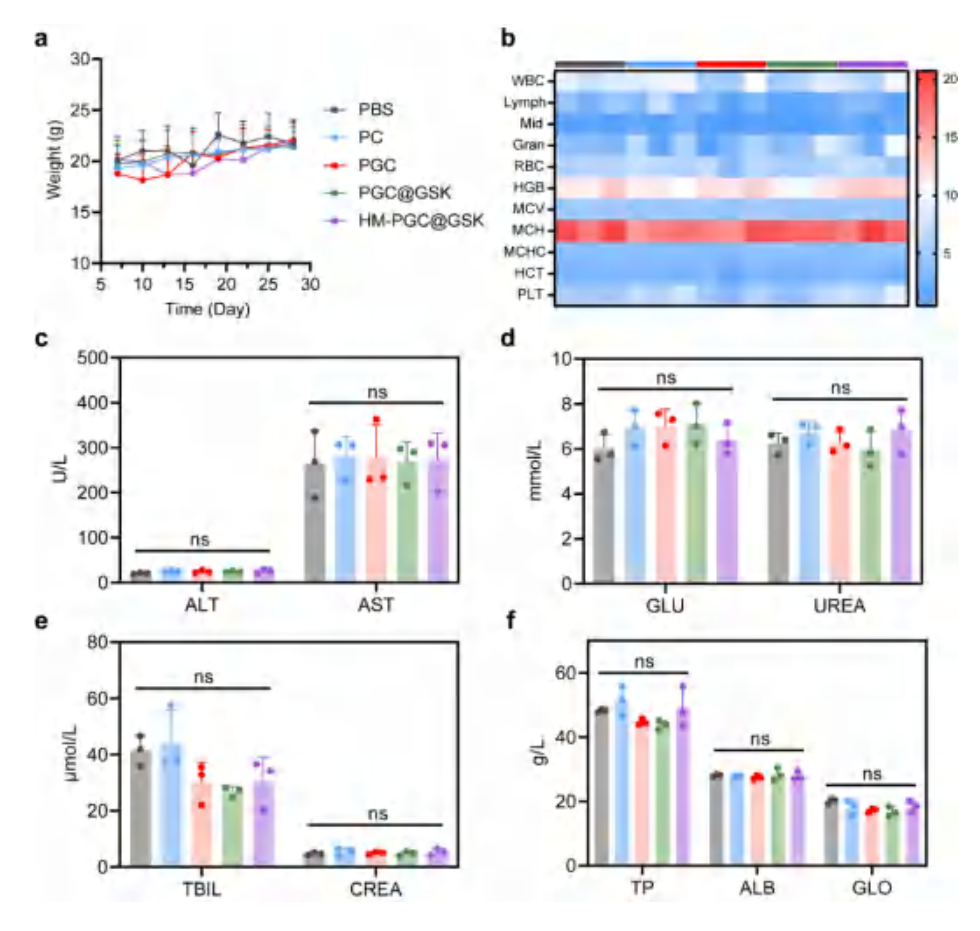


Figure S38. a, Average body weight of mice with subcutaneous CRC tumors across different treatment groups within 28 days of treatment. n = 6 independent samples. b, Heat map of the complete blood cell counts analysis of mice with subcutaneous CRC tumor after different treatment. n = 3 independent samples. Granulocyte (Gran, 10^9 cells L^{-1}), hematocrit (HCT, %), hemoglobin (HGB, g L^{-1}), lymphocyte (Lymph, 10^9 cells L^{-1}), mean corpuscular volume (MCV, fl), mean corpuscular hemoglobin (MCH, pg), mean corpuscular hemoglobin concentration (MCHC, g L^{-1}), intermediate cell (Mid, 10^9 cells L^{-1}), platelets (PLT, 10^9 cells L^{-1}), red blood cells (RBC, 10^{12} cells L^{-1}), and white blood cells (WBC, 10^9 cells L^{-1}). c-f, Analysis of complete blood biochemical indices in mice with subcutaneous CRC tumor after different treatment. Liver function-related alanine transaminase (ALT), aspartate transaminase (AST) (c), kidney function-related urea (UREA), glucose (GLU), creatinine (CREA) and bilirubin (TBIL) (d, e), as well as total protein (TP), albumin (ALB) and globulin (GLO) (f). n = 3 independent samples. Data are presented as mean \pm s.d. Statistical significance was determined by one-way ANOVA with Tukey's post hoc correction (c, d, e, f).

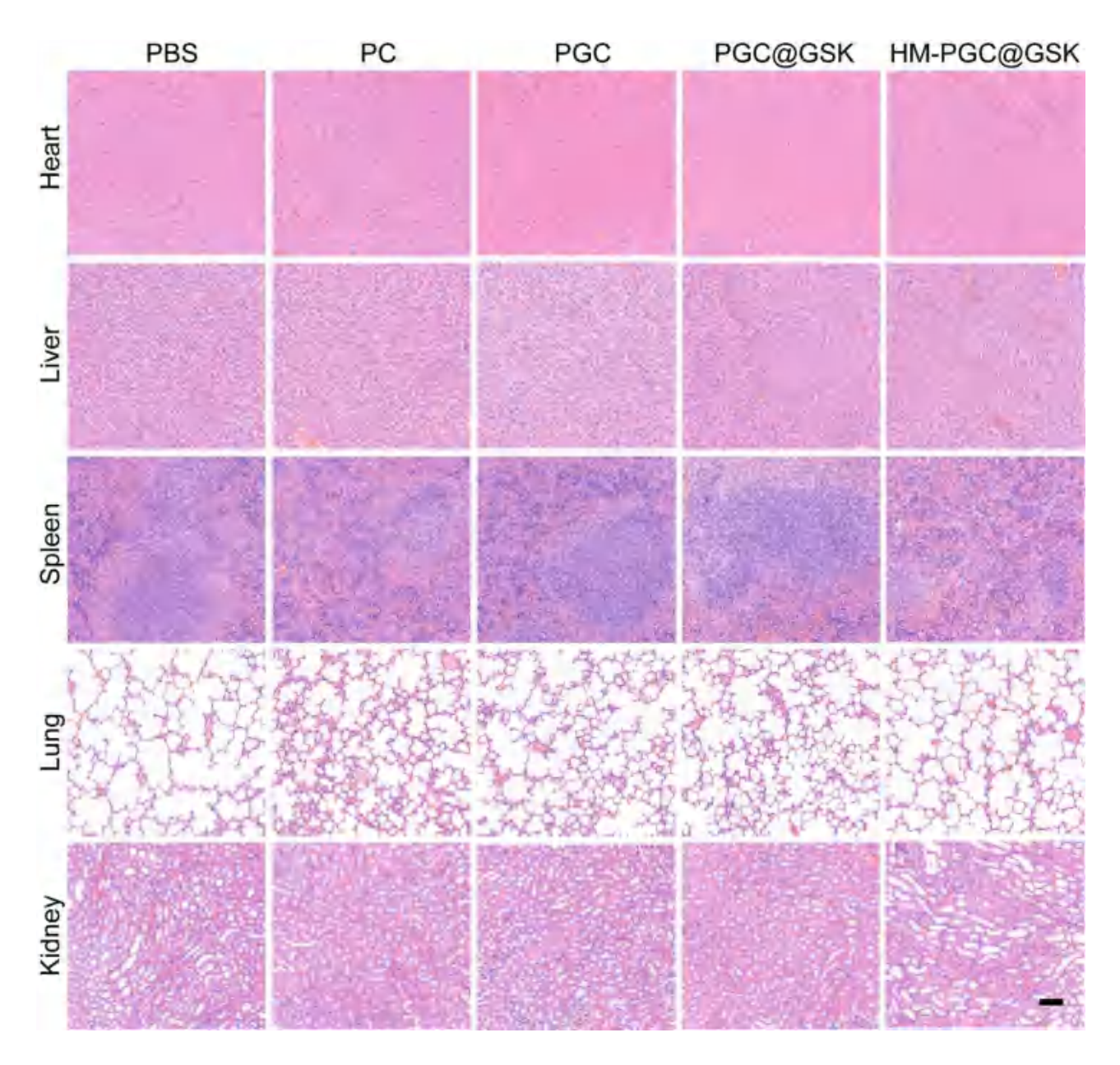


Figure S39. Representative images of H&E staining of major organs from mice with subcutaneous CRC tumor after different treatment. Scale bar, $100~\mu m$.

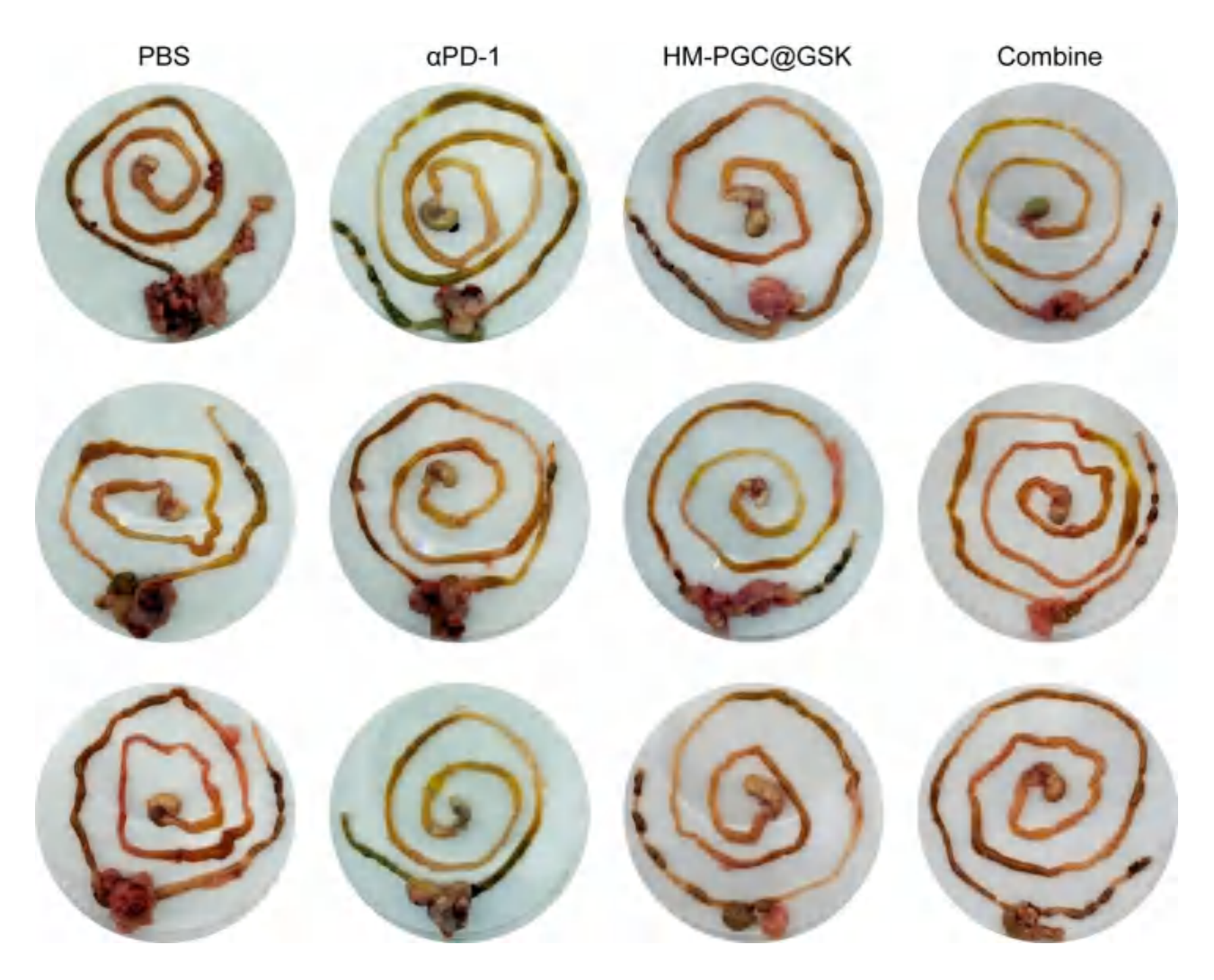


Figure S40. Representative bright-field images of the intestinal sections from mice with orthotopic CRC following different treatment. n = 3 independent samples.

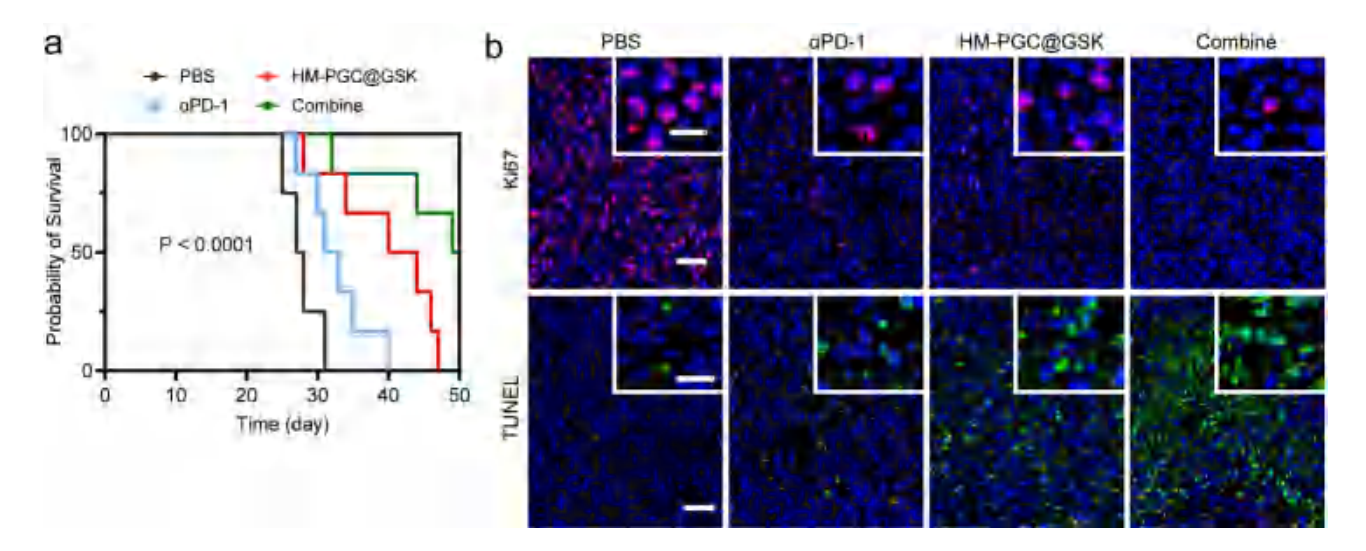


Figure S41. a, Survival curves of mice with orthotopic CRC in different treatment groups. n=6 independent samples. b, Representative Ki67 and TUNEL staining images of tumor sites in mice with orthotopic CRC following different treatment. Scale bar, 50 μ m. Data are presented as mean \pm s.d. Statistical significance was determined by log-rank (Mantel-Cox) test (a).

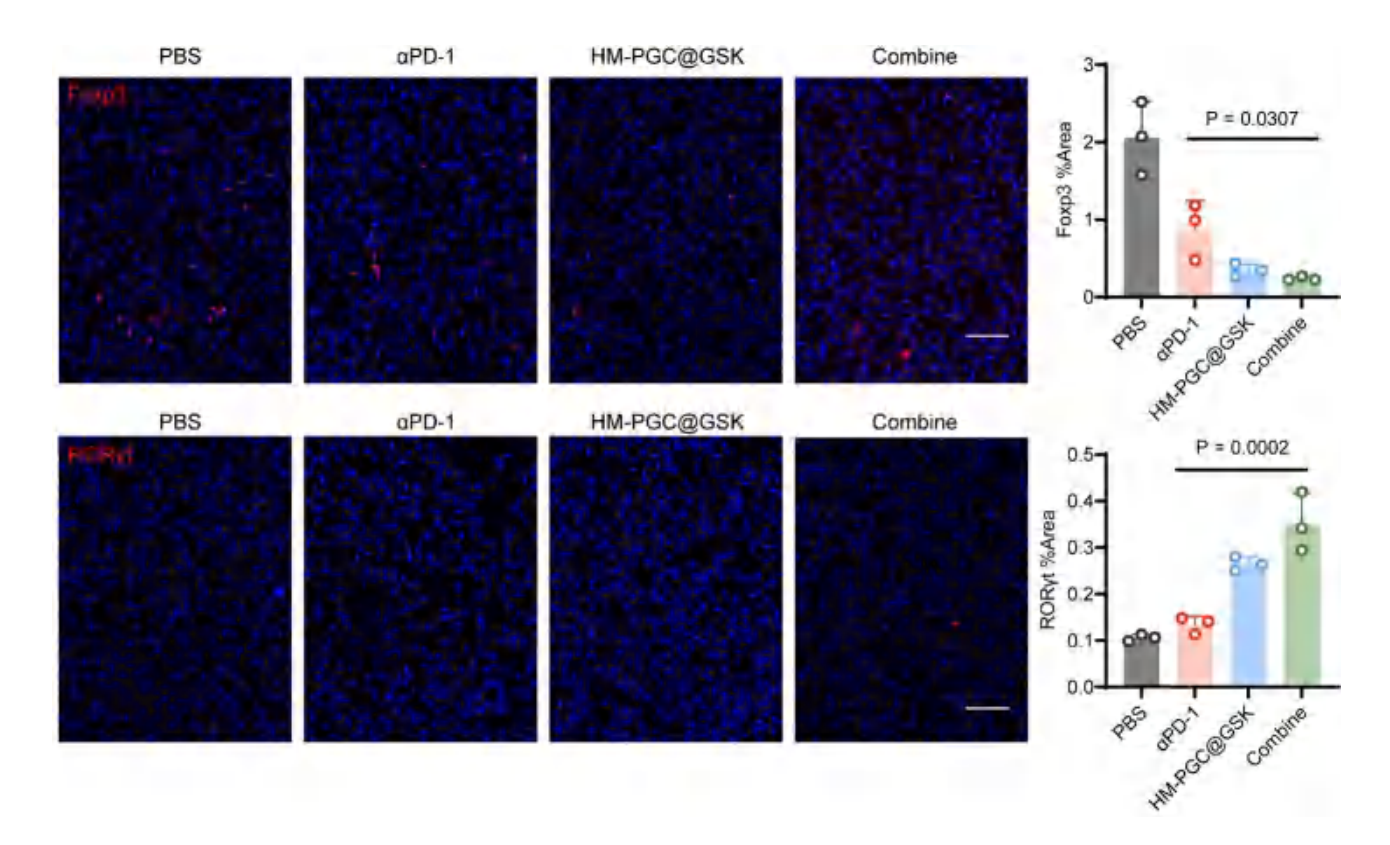


Figure S42. Representative immunofluorescence staining CLSM images and quantitative analysis of Treg (Foxp3⁺) and Th17 (ROR γ t⁺) of orthotopic tumor tissues from mice in different treatment groups. Scale bar, 50 μ m. n = 3 independent samples. Data are presented as mean \pm s.d. Statistical significance was determined by one-way ANOVA with Tukey's post hoc correction.

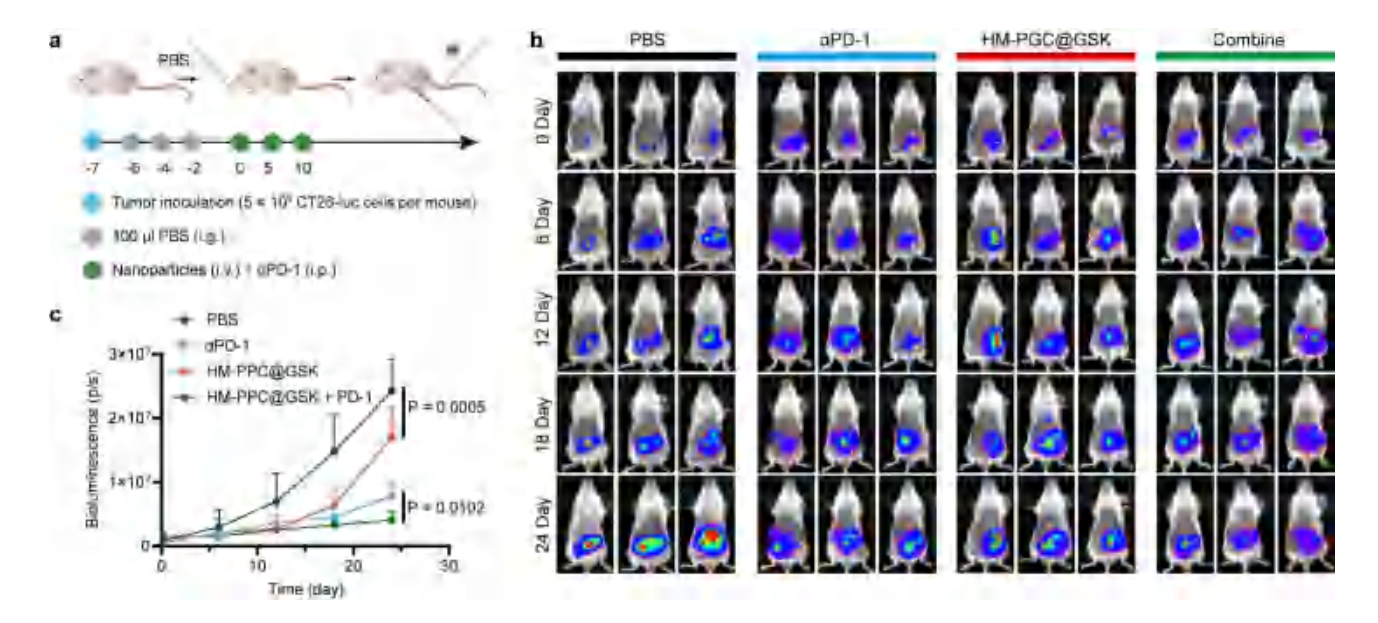


Figure S43. a, Schematic diagram of the orthotopic CRC model without *C. albicans* burden construction and the HM-PGC@GSK combined with ICB treatment scheme. b-c, In vivo bioluminescence imaging and quantitative analysis of orthotopic CRC mice after receiving PBS, αPD-1, HM-PGC@GSK and combine treatment.

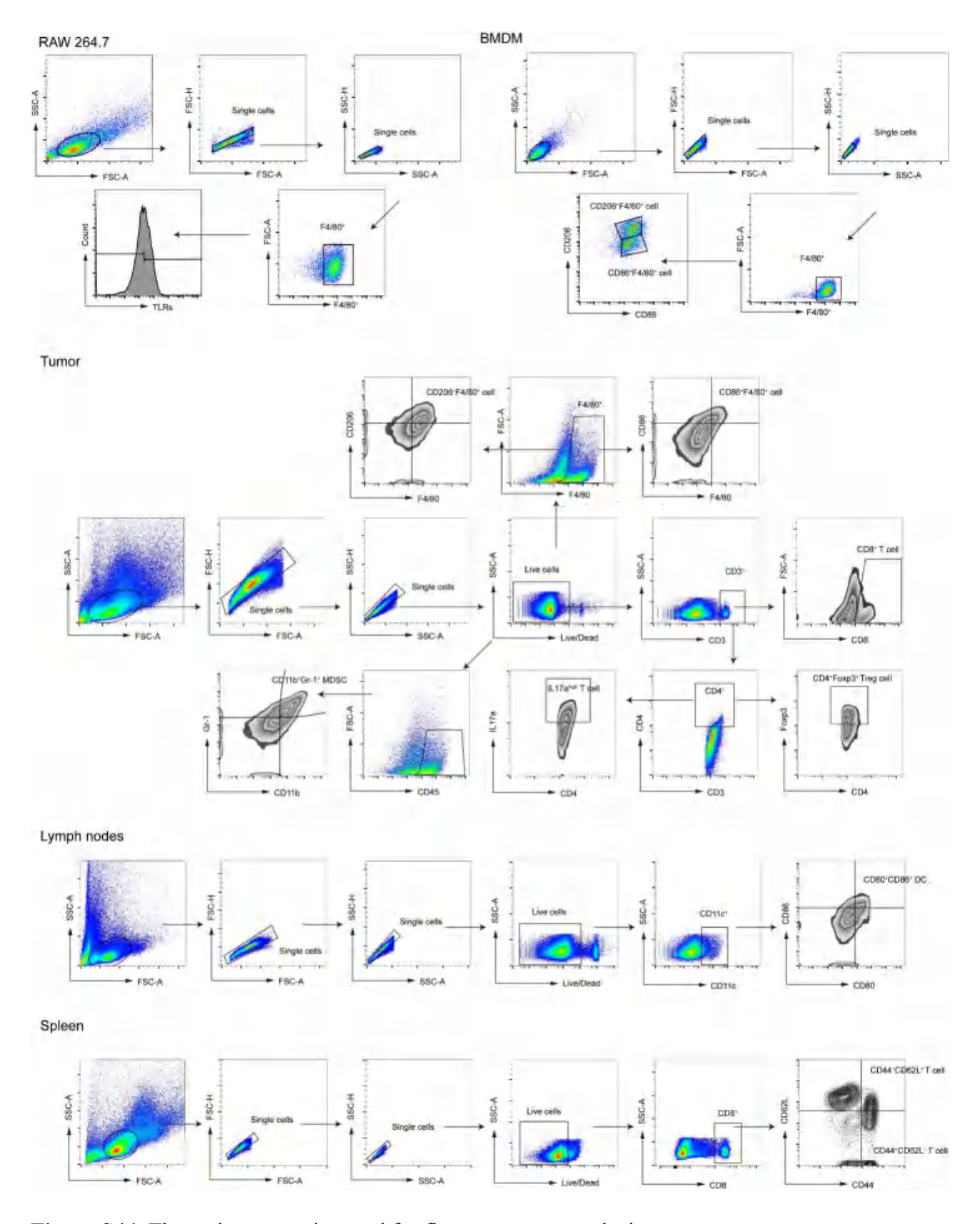


Figure S44. The gating strategies used for flow cytometry analysis.

Table S1. Probe sequences for FISH experiments

Probe name	Probe sequence (5'-3')
Du.al 1249	GCCAAGGCTTATACTCGCT

Table S2. Primer sequences for qRT-PCR analysis

Gene name	Forward primer (5'-3')	Reverse primer (5'-3')
Mouse-Dectin-1	ATAGAGAATCTGGATGAAGATGGAT	CTACTACCACAAAGCACAGGATTC
Mouse-TLR2	ACGTTTGCTATGATGCCTTTGT	AGACACAGCTTAAAGGGCGG
Mouse-TLR4	ACACTTTATTCAGAGCCGTTGGT	CAGGTCCAAGTTGCCGTTTC
Mouse-MR	CGTTTCGGTGGACTGTGGA	GTTGTGGGCTCTGGTGGG
Mouse-GSDMD	CGTGGCAGGAGCAGAGTTCT	ATAGAGCGCACTTGTGGGGA
Mouse-HWP1	CAGAATCATCATCTGCTCCAGC	AGCAGTAGAAACTGGAGTAGTTTCA